

***IN VIVO* DETECTION OF GADOLINIUM BY PGNA**

***IN VIVO* DETECTION OF GADOLINIUM BY PROMPT GAMMA NEUTRON
ACTIVATION ANALYSIS: AN INVESTIGATION OF THE POTENTIAL
TOXICITY OF GADOLINIUM-BASED CONTRAST AGENTS USED IN MRI**

By

JAMES L. GRÄFE, B.Sc.

A Thesis

Submitted to the School of Graduate Studies

in Partial Fulfilment of the Requirements

for the Degree

Doctor of Philosophy

McMaster University

© Copyright by James L. Gräfe, August, 2012

DOCTOR OF PHILOSOPHY (2012)
(Medical Physics)

McMaster University
Hamilton, Ontario

**TITLE: *IN VIVO* DETECTION OF GADOLINIUM BY PROMPT GAMMA
NEUTRON ACTIVATION ANALYSIS: AN INVESTIGATION OF THE
POTENTIAL TOXICITY OF GADOLINIUM-BASED CONTRAST AGENTS
USED IN MRI**

AUTHOR: James L. Gräfe, B.Sc. (University of Guelph)

SUPERVISOR: Dr. Fiona E. McNeill

NUMBER OF PAGES: xv, 155

ABSTRACT

This thesis describes the development of a method to measure *in vivo* gadolinium (Gd) content by prompt gamma neutron activation analysis (PGNAA). PGNAA is a quantitative measurement technique that is completely non-invasive. Gadolinium has the highest thermal neutron capture cross section of all the stable elements. Gadolinium-based contrast agents are widely used in magnetic resonance imaging (MRI). The primary intention of this work is to quantify *in vivo* Gd retention to investigate the potential toxicity of these agents. This study involves the optimization of the McMaster University $^{238}\text{Pu}/\text{Be}$ PGNAA facility for Gd measurements. Monte Carlo simulations were performed in parallel with the experimental work using MCNP version 5. Excellent agreement has been demonstrated between the Monte Carlo model of the system and the experimental measurements (both sensitivity and dosimetry). The initial study on the sensitivity of Gd demonstrated the feasibility of the measurement system. The Monte Carlo dosimetry simulations and experimental survey measurements demonstrated consistently that the radiation exposures for a single measurement were quite low, with an effective dose rate of 1.1 $\mu\text{Sv/hr}$ for a leg muscle measurement, 74 $\mu\text{Sv/hr}$ for a kidney measurement, and 48 $\mu\text{Sv/hr}$ for a liver measurement. The initial studies confirmed the Gd measurement feasibility which ultimately led to an *in vivo* pilot study on 10 healthy volunteers. The pilot study was successful with 9 out of 10 volunteers having measureable Gd in muscle above the *in vivo* detection limit of 0.58 ppm within 1 hour of administration, and the remaining participant had detectable Gd 196 minutes post administration. The concentrations measured ranged from 6.9 to 56 uncertainties different from zero. The system has been validated in humans and can now be used in future studies of short or long-term retention of Gd after contrast administration in at risk populations, such as those with reduced kidney function, patients with multiple exposures over the treatment period, and patients who are prescribed higher dosages. In addition, experiments and simulations were extended to another high neutron absorbing element, samarium (Sm).

Acknowledgements

I am very grateful to my supervisor Dr. Fiona McNeill for her guidance and support during these past few years. After every talk with Fiona I left with the answers to all my problems. Fiona is an accomplished and experienced researcher, and working with her has been an honour. Her natural calmness and depth of knowledge provided for the perfect working environment.

I also must acknowledge my incredible supervisory committee for their encouragement and outstanding expertise. Dr. Soo Hyun Byun, an expert in radiation metrology, was always available to help with detector related issues as well as discuss the theoretical aspects of my project. Dr. David Chettle provided invaluable advice on statistics and data analysis, and always thoroughly evaluated my work. I appreciate your continuous effort and contagious enthusiasm in all that was involved in my project and in science in general. Finally, thanks to Dr. Michael Noseworthy who first proposed this research project and was our connection to the field of MRI.

There are also many colleagues who have helped me along the way: Chantal Green, Witold Matysiak, Jovica Atanackovic, Gloria Orchard, Lesley Egden, Eric Da Silva, Elstan Desouza and Victor Kreft. In particular, I am very grateful to the late Mike Chamberlain who was a mentor to me in the early stages of my research; from the very beginning he made me feel welcome in the lab and was always willing to give me advice, he was the most selfless person I have ever met, and always made himself free to talk about anything.

I've made some great friends, and I am very thankful to Kristina, Caitlin, Bill, Ryan, Kyle, and Eric, who have shared some great times with me over the past few years here in Hamilton. I thank Susan Durst for her constant encouragement, love and support. My faithful canine companion Bear was there by my side throughout the final stages of my thesis, and played a big part in helping me achieve a balance between work and outdoor adventures.

The Medical Physics & Applied Radiation Sciences department has many wonderful staff, and I appreciate all the administrative help from Wendy Malarek, Fiona

Ahlang, Vera Larossi, Linda Ellis, and Nancy Brand. I must also acknowledge the technical help and advice I received from Jason Falladown and Scott McMaster while working in the Tandem Accelerator Building. Jason and Scott are two of the most practical and ingenious people I have ever met. I am also thankful to Alice Pidruczny for all her technical help, and for allowing me to use her lab for phantom preparation. Dr. Bill Prestwich provided me with some very valuable experimental and theoretical advice. Thanks also to Dave Tucker, Steve Staniek, and Chris Malcolmson of Health Physics for all their assistance and advice on radiation safety.

I thank my family who have always loved and supported me throughout my life.

Contents

Acknowledgements	iv
1 Introduction.....	1
1.1 Gadolinium	2
1.2 Gadolinium-based contrast agent toxicity.....	2
1.3 Neutron activation analysis.....	3
1.4 Prompt gamma neutron activation analysis of gadolinium.....	5
1.5 $^{238}\text{Pu}/\text{Be}$ source based system	9
1.6 Gadolinium detection: choice of detector	12
1.7 Phantom preparation	14
1.8 Thesis preface	16
2 The feasibility of <i>in vivo</i> detection of gadolinium by prompt gamma neutron activation analysis following gadolinium-based contrast-enhanced MRI (Article I)	17
2.1 Introduction to Article I	17
2.2 Contents of Article I.....	17
3 A benchmarked MCNP model of the <i>in vivo</i> detection of gadolinium by prompt gamma neutron activation analysis (Article II)	25
3.1 Introduction to Article II.....	25

3.2 Contents of Article II	26
3.3 Additional Material	34
4 Characteristic X ray emission in gadolinium following neutron capture as an improved method of <i>in vivo</i> measurement: a comparison between feasibility experiment and Monte Carlo simulation (Article III)	36
4.1 Introduction to Article III.....	36
4.2 Contents of Article III	37
4.3 Additional Material	43
5 Radiation dosimetry for the measurement of gadolinium by PGNAA using the ²³⁸Pu/Be source-based system	49
5.1 Simulated phantom dosimetry	49
5.1.1 Lower leg muscle irradiation	50
5.1.2 Kidney irradiation	54
5.1.3 Liver irradiation	58
5.2 Benchmark measurements: comparison of experimental and simulated dose rates	62
5.3 Gadolinium dose enhancement	63
5.3.1 Macroscopic Gd dose enhancement: a comparison of ENDF data.....	66
5.3.2 Heating numbers: kerma approximation.....	73
5.3.3 Kerma coefficients based on kinematics.....	74

5.3.4 Hydrogen benchmark calculation	78
5.4 Gadolinium dose enhancement: phantom dosimetry	80
5.4.1 Dose enhancement: leg irradiation.....	83
5.4.2 Dose enhancement: kidney irradiation.....	84
5.4.3 Dose enhancement: liver irradiation	85
5.5 Concluding remarks on dosimetry for the measurement of Gd using the $^{238}\text{Pu}/\text{Be}$ source-based system.....	87
6 Gadolinium detection via <i>in vivo</i> prompt gamma neutron activation analysis following gadolinium-based contrast agent injection: a pilot study in 10 human participants (Article IV)	89
6.1 Introduction to Article IV	89
6.2 Contents of Article IV	90
6.3 Additional material	109
6.3.1 Comment on the participant MR image data	109
6.3.2 Phantom calibration lines.....	109
6.3.3 Spectra from the secondary detector.....	111
7 <i>In vivo</i> detection of samarium in the kidney by PGNAA	115
7 Introduction.....	115
7.1 Materials and methods	115

7.2 Results and discussion	117
7.2.1 Experimental sensitivity and detection limits	117
7.2.2 Monte-Carlo simulation of samarium sensitivity	119
7.2.3 Detection efficiency loss	122
7.2.4 Comment of the loss of efficiency in the Gd photon emission energy region	128
7.2.5 Predicted detection limits for various body types	129
7.2.6 Sm K X rays	132
7.3 Conclusions	133
8 Conclusions	135
8.1 Discussion and thesis conclusions	135
8.2 Future work	139
8.2.1 Accelerator-based neutron source	139
8.2.2 Indirect measurement of Gd	141
8.2.3 Kidney impaired population	143
8.2.4 Gadolinium in bone	143
References	147

List of Figures

Figure 1.1. Log-log plot of the neutron capture cross sections for $^{155,157}\text{Gd}$ (Chadwick et al. 2006). The $1/\nu$ function is shown for comparison.....	5
Figure 1.2. Spectra from 2 L Gd phantoms showing the 199.2 keV prompt gamma ray from neutron capture of ^{155}Gd and the interfering background peak at 197.91 keV.	8
Figure 1.3. Spectra from 2 L Gd phantoms showing the 88.97 and 79.5 keV prompt gamma rays from neutron capture of ^{155}Gd and ^{157}Gd , respectively, and the characteristic Pb K X rays produced in the shielding components.	9
Figure 1.4. Neutron spectrum of the $^{238}\text{Pu}/\text{Be}$ source from Block et al. (1967).	11
Figure 1.5. Decay curve of the combined activity from the ^{238}Pu sources.	12
Figure 1.6. Spectra from 0 and 151 ppm 2 L Gd phantoms measured using a NaI(Tl) detector.....	14
Figure 3.1. Simulated neutron beam profile 5 cm away from the shielding and collimating apparatus.	34
Figure 3.2. Neutron fluence rate profile as a function of depth in water for the $^{238}\text{Pu}/\text{Be}$ system.	35
Figure 4.1. Geometry for the kidney phantom placed in 7 cm axial and lateral depths in the torso phantom. The detector is placed behind 2.5 cm of Pb photon shielding. (Monte-Carlo model of the geometrical set-up.)	44
Figure 4.2. Gadolinium kidney detection limits for various overlying tissue thicknesses.	46
Figure 4.3. Gadolinium liver detection limits for various overlying tissue thicknesses.	47

Figure 5.1. The top (a) and side view (b) of the irradiation geometry for the lower leg muscle. Image output from MCNP Visual Editor.....	51
Figure 5.2. Kidney irradiation geometry showing the (1) left kidney aligned with the collimated neutron beam from the irradiation facility. Also visible in this plane are the (2) right kidney, (3) liver, (4) gall bladder, (5) pancreas, (6) stomach, (7) spleen, and (8) spinal cord. Image adapted from MCNP Visual Editor.	55
Figure 5.3. Liver irradiation geometry showing the (3) liver aligned with the collimated neutron beam from the irradiation facility. Also visible in this plane are the (1) left kidney, (2) right kidney, (4) gall bladder, (5) pancreas, (6) stomach, (7) spleen, and (8) spinal cord. Image adapted from MCNP Visual Editor.	59
Figure 5.4. Comparison of the absorbed dose rate to an ICRU sphere from two kerma data-sets as a function of neutron energy from the $^{238}\text{Pu}/\text{Be}$ source. Also shown is the neutron fluence rate spectrum.	68
Figure 5.5. The equivalent dose rate to an ICRU sphere as function on neutron energy, calculated based on the ICRP60 & 103 recommendations. Also shown are the ICRP60 & 103 radiation weighting factors.	69
Figure 5.6. Neutron dose enhancement as a function of Gd concentration in an ICRU sphere for three different data libraries.	70
Figure 5.7. Comparison of the average heating numbers for ^{157}Gd from (a) ENDF-B-V.0 and (b) ENDF-B-VII.0. Images adapted from ‘Cross Section Plotting’ feature of MCNP Visual Editor.	71

Figure 5.8. Photon dose enhancement as a function of Gd concentration in an ICRU sphere for three different data libraries.	72
Figure 5.9. ^{157}Gd kerma components determined from available libraries in MCNP and derived based on kinematics. See text below for the kerma coefficients from equations 1-3.....	74
Figure 5.10. The kerma calculated from the local deposition of the full Q -value from the $^{157}\text{Gd}(n,\gamma)$ reaction and compared with the ENDF-B-V.0 data.....	78
Figure 5.11. Comparison of the kinematic neutron kerma coefficients in ^1H and those available in two MCNP data libraries.	79
Figure 5.12. Comparison of the neutron kerma in soft tissue with the IC/Auger electron and low energy X ray kerma from 550 pm Gd. The neutron soft tissue kerma is from Chadwick et al (1999). Also shown is the “equivalent dose” coefficient which is the neutron soft tissue kerma weighted with the ICRP103 neutron radiation weighting factors.	82
Figure 6.1. Phantom calibration lines from the LO-AX detector for 4 photon emission lines: (a) 181.9 keV, (b) 79.5 keV, (c) Gd K_{α} , (d) Gd K_{β}	110
Figure 6.2. Phantom calibration lines from the GMX detector for 2 photon emission lines: (a) 181.9 keV, (b) Gd K_{α}	111
Figure 6.3. Comparison of the fitted spectra obtained for all three measurements from one of the participants. The spectra show four photon emissions from neutron capture of ^{155}Gd and ^{157}Gd measured by the GMX detector. In measurement B, 17.3 ± 0.3 ppm of Gd was detected in the muscle.	112

Figure 6.4. Comparison of the spectra from the LO-AX and GMX detectors for a zero concentration phantom.....	113
Figure 7.1. Representative spectrum from a 150 ppm Sm phantom showing the 334 and 440 keV prompt gamma ray emissions.....	117
Figure 7.2. Representative spectra for the fitted 334 and 440 keV prompt gamma rays from Sm.	118
Figure 7.3. 440 and 334 keV experimental calibration lines for the kidney at 4 cm lateral and axial depths.....	119
Figure 7.4. Comparison plot of the measured and simulated 334 and 440 keV peak areas. The simulated values are determined based on the gamma emission probabilities from two different sources.....	121
Figure 7.5. Relationship between loss in efficiency and photon mean free path.....	125
Figure 7.6. Samarium kidney detection limits for various overlying tissue thicknesses.	129
Figure 7.7. Comparison of the neutron capture cross-sections of ^{157}Gd and ^{149}Sm from ENDF/B-VII.0. The neutron fluence rate spectrum in the kidney phantom is also shown on the secondary y-axis.....	131
Figure 7.8. Spectrum of the fitted Sm K Xrays from a 150 ppm Sm kidney phantom for a 20 000 second acquisition.	133
Figure 8.1. Simulated reduction in the number of 2.223 MeV hydrogen neutron captures as a function of Gd concentration in the 2 L phantoms.	142

List of Tables

Table 1.1 Isotopic thermal neutron cross section data, and relative probability for neutron capture in each naturally occurring isotope of gadolinium ($Z = 64$).	6
Table 1.2. Properties of the standards used to prepare the Gd phantoms.	15
Table 4.1. Individual kidney detection limits for the shallowest and greatest depths considered (the positions represent lateral and axial depths respectively).	46
Table 4.2. Individual liver detection limits for the shallowest and greatest depths considered (the positions represent lateral and axial depths respectively).	47
Table 5.1. MCNP calculated dose rates to the leg tissues of the ORNL adult male phantom.....	53
Table 5.2. MCNP calculated equivalent dose rates to the organs at risk for the kidney irradiation geometry.	56
Table 5.3. MCNP calculated effective dose components for the kidney irradiation.	57
Table 5.4. MCNP calculated equivalent dose rates to the organs at risk for the liver irradiation geometry.	60
Table 5.5. MCNP calculated effective dose components for the liver irradiation.	61
Table 5.6. Comparison of simulated and measured survey dose rate measurements.	63
Table 5.7. Photon production data from two libraries available in MCNP5.	77
Table 5.8. Summary of the neutron heating data from the available cross-section libraries for ^1H in MCNP.	80

Table 5.9. The photon equivalent dose-enhancement from 550 ppm Gd in the leg soft tissue. The table shows the ratio of the dose with 550 ppm in the leg soft tissue to the dose with zero Gd in the leg soft tissue.....	84
Table 5.10. The photon equivalent dose-enhancement from 550 ppm Gd in the kidneys. The table shows the ratio of the dose with 550 ppm in the kidneys to the dose with zero Gd in the kidneys.	85
Table 5.11. The photon equivalent dose-enhancement from 550 ppm Gd in the liver. The table shows the ratio of the dose with 550 ppm in the liver to the dose with zero Gd in the liver.	86
Table 6.1. Average reduced- χ^2 from the peak area fits.	111
Table 6.2. Comparison of peak resolution and detection limits for the Gd photon emission lines from both detectors.....	113
Table 7.1. Comparison of the available data sources for the gamma emission probabilities for neutron capture in ^{149}Sm , and ^{157}Gd	121
Table 7.2. Ratio of the most current-to-initial full-energy peak efficiency measurement. The n-type Ge detector efficiency has decreased as a function of energy due to neutron damage.	123
Table 7.3. Comparison of the proportion of neutron captures per neutron energy bin for ^{149}Sm and ^{157}Gd . Also shown is the ratio of the number of captures in ^{157}Gd to ^{149}Sm per energy bin.....	132

Chapter 1

1 Introduction

Body and tissue composition studies by non-invasive methods combine the expertise of researchers from many different disciplines, such as: archaeology, physics, biology, and chemistry. Many analytical radiation-based methods have been developed and include techniques such as X ray fluorescence (XRF) and neutron activation analysis (NAA) (Chettle 2006). In all of radiation-based techniques, the main premise is the same; to probe the tissue non-invasively with a radiation source to excite the element or isotope of interest, and to measure the resultant induced radiation signal using a radiation detector. In the case of *in vivo* exposures these goals must be achieved while keeping the radiation dose to reasonably low levels. It is usually considered acceptable if radiation exposures for these techniques are comparable to diagnostic clinical exposures. For *ex vivo* samples, this is less of a limitation as these methods are only destructive when enormous radiation doses of the MGy level are applied. For most practical applications, the techniques are considered completely non-destructive. The main focus of this thesis is on the development of the technique of *in vivo* NAA for the measurement of gadolinium. This had not been performed prior to this work. The irradiation system used in this study was initially developed for measurements of the body burden from the toxic element cadmium (Fedorowicz et al. 1993). The system was then subsequently improved by McNeill and Chettle (1998), and most recently by Grinyer (2008). The work in this thesis therefore builds upon previous experimental and theoretical work that was performed by the researchers mentioned above and upon the referenced articles cited within those works.

1.1 Gadolinium

Gadolinium (Gd) is a silvery white metal with atomic number (Z) 64, and atomic weight 157.25. The density of Gd is 7.901 g/cm^3 . Gadolinium is part of the lanthanide group in the periodic table and is frequently called a rare-earth metal, although it is found as high as 6 parts per million (ppm; $\mu\text{g/g}$) in the earth's crust (Haynes 2012). Gadolinium has a melting and boiling point of 1313 and 3273 °C, respectively (Haynes 2012). Gadolinium is named after the Finnish chemist Johan Gadolin who played a role in its discovery (Wastie, Latief 2004). Gadolinium is used in industry in magnets, and glass additives (Hirano, Suzuki 1996); also phosphors for color TV tubes can be made from Gd compounds (Haynes 2012). Gadolinium is also used as a neutron detector for neutron radiography (Spowart 1972). The most popular use of Gd is as a contrast agent in MRI. Gd was proposed as a contrast material because of its paramagnetic properties due to the 7 unpaired 4f electrons of the Gd^{3+} ion. It has now gained widespread use due to the demonstrated clinical efficacy for improved diagnosis and is routinely used where contrast is required to visualize lesions in the Central Nervous System (CNS), and to evaluate heart (Swaminathan et al. 2008) or liver disease, blood brain barrier disruptions, identify cancerous tumours, plus many other applications.

1.2 Gadolinium-based contrast agent toxicity

Gd is toxic in its free form and therefore is chelated to form a stable metabolically inert complex. There is concern for the safety of Gd-based agents in patients with renal disease. The first publication to demonstrate a link between Gd contrast agent administration and the disease nephrogenic systemic fibrosis (NSF) is that of Grobner (Grobner 2006). NSF is a painful and debilitating disease that causes fibroses of the skin and systemic tissues (Thakral, Alhariri & Abraham 2007). Following this initial paper, numerous reports of NSF (and the link to Gd compounds) have been published, and as a result of this paper, much research was conducted, including the work in this thesis.

Grobner's paper was the most referenced paper in the journal *Nephrology Dialysis Transplantation* between 2005 and 2009 with 258 citations by the end of 2009 (Lameire, Floege & Wheeler 2010), highlighting the significance of this issue within the clinical community. The issue has been noted by policy makers. The U.S. Food and Drug Administration (FDA) released a Public Health Advisory on June 8 2006, describing a possible link between NSF and gadolinium-based contrast agents (GBCA) in patients with kidney failure (FDA 2006). Subsequently another alert has been released (May 23, 2007, updated June 8, 2009) requesting that manufacturers add boxed warnings about the risk for the development of NSF (FDA 2009).

There have been no reports of NSF in patients with healthy renal function. These agents are used routinely with an estimated 10 million MRI scans being performed per year with Gd-enhancement in the U.S. (Colletti 2008). The main reports of adverse events as a result of Gd-based drugs in people with healthy renal function are allergic reactions. Although most of the adverse events reported are mild, varying from headache to injection site pain, there is still a concern about how much Gd is retained after injection. It is, at this point in time, unknown if there are people currently experiencing sub-clinical or chronic low level symptoms from Gd retention, or if there will be late effects that arise in the future. This thesis work was therefore undertaken to develop a non-invasive monitoring system for the study of Gd retention as an aid to understanding the potential toxicity of MRI contrast enhancing drugs.

1.3 Neutron activation analysis

Neutron activation analysis (NAA) is a well developed technique used to characterize the elemental composition of matter. The applications of NAA encompass many fields, such as geology, archaeology, security, and medical physics. For medical applications analyzing the living human, the technique is labelled *in vivo* neutron activation analysis (IVNAA). IVNAA has proven to be a sophisticated non-invasive method for determining concentrations or absolute amounts of essential elements in the body, such as nitrogen &

calcium, as well as the body burden of toxic trace elements present from occupational and environmental exposures (Chettle, Fremlin 1984).

When measuring gamma ray emissions in NAA the reactions of interest are neutron absorption and neutron inelastic scattering. Neutron inelastic scattering is a threshold reaction that occurs only if the neutron energy is above the energy of the nuclear first excited state of the scattering isotope. For neutron absorption (also termed “radiative neutron capture”), the underlying principle is quite simple; a neutron source irradiates a sample, and absorption of neutrons occurs within the target nuclei. The excited compound nucleus will initially de-excite to its ground-state by emission of ‘prompt’ gamma rays within nano-seconds to pico-seconds of capture. The nuclear ground-state may be stable or will be subject to further radioactive decay mechanisms (such as, for example, isomeric transitions or β^- decay). If the nuclear ground-state is stable after the initial prompt gamma ray emission, detection and irradiation must take place simultaneously in order to measure the prompt gamma rays. If the ground state is unstable, ‘delayed’ gamma ray emission can occur and irradiation can be followed by detection due to the extended time period that the sample may remain radioactive. The resultant characteristic γ -rays are measured using scintillation or semiconductor detectors. Ideally, the γ -rays are not only characteristic of, but specific to a single reaction, and thus the presence of the initial element can be uniquely identified. Comparison of the signal from the sample with the signal from appropriate calibration standards can mean that the element is not only identified, but the level of the element quantified.

The probability of a given elemental nucleus to absorb a neutron is characterized by its neutron capture cross section. The reaction cross section is an effective area of interaction, measured in units of cm^2 or barns ($b = 1 \times 10^{-24} \text{ cm}^2$). For many isotopes, the neutron capture cross section follows the “ $1/v$ law”, in which the cross section increases with decreasing neutron speed. However, the isotopes of gadolinium along with isotopes of cadmium, europium, and samarium are among a group of so called “non- $1/v$ isotopes” (Sun, Byun & Choi 2003). The neutron capture cross sections for ^{155}Gd and ^{157}Gd are shown in Figure 1.1 (Chadwick et al. 2006). There is a pronounced edge in the cross

sections at energies of the order of a 100^{th} of an eV and there are many resonances between approximately 1 eV and 400 eV. Also for comparison the $1/v$ function is shown in Figure 1.1.

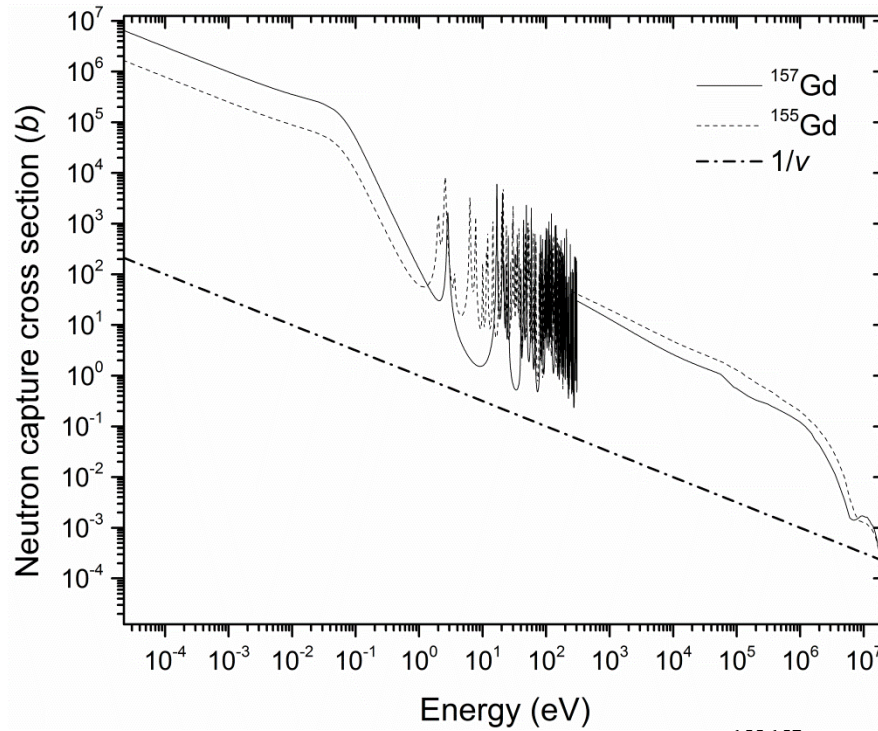
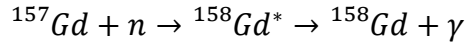
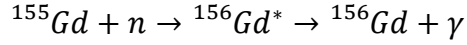


Figure 1.1. Log-log plot of the neutron capture cross sections for $^{155,157}\text{Gd}$ (Chadwick et al. 2006). The $1/v$ function is shown for comparison.

1.4 Prompt gamma neutron activation analysis of gadolinium

Gadolinium has seven naturally occurring isotopes. The extremely large capture cross section for two of these isotopes, ^{155}Gd and ^{157}Gd , enables naturally occurring gadolinium to be a unique and likely candidate for IVNAA. Gadolinium has the largest thermal neutron capture cross section of all the stable elements. Neutron irradiation of natural gadolinium results predominantly in the production of excited $^{156}\text{Gd}^*$ and $^{158}\text{Gd}^*$, which decay by prompt gamma emission to the stable ground-states of ^{156}Gd and ^{158}Gd ,

respectively. Gd is measured therefore by prompt gamma neutron activation analysis (PGNAA). The neutron capture reactions are:



The isotopic natural abundances, thermal neutron capture cross sections, and emission probabilities for the most dominant γ -rays for the different isotopes of gadolinium are shown in Table 1.1. Also given in Table 1.1 is the relative percentage of neutron captures (per source neutron) for each naturally occurring Gd isotope. It can be seen that ^{155}Gd and ^{157}Gd account for more than 99.9% of neutron captures in natural Gd. The cross section dependence on energy is shown in Figure 1.1.

Table 1.1 Isotopic thermal neutron cross section data, and relative probability for neutron capture in each naturally occurring isotope of gadolinium ($Z = 64$).

Isotope	Abundance (%)	σ_γ (barns)	Relative neutron captures (%)	Most probable γ -ray emission energy in keV (% ^b)
152	0.20	735	0.003	
154	2.18	85	0.004	
155	14.80	60900	18.48	199.2 (22.4), 88.97 (15.3)
156	20.47	1.8	0.0008	
157	15.65	254000	81.51	181.9 (18.1), 79.51 (10.1), 944.2 (7.8)
158	24.84	2.2	0.001	
160	21.86	1.4	0.0006	

Data taken from (IAEA 2007)

^b Percent per neutron capture

The difficulty involved in the measurement of Gd in living human beings is that the γ -rays associated with the reaction are low energy prompt γ -rays that are observed in the acquired spectrum, sitting upon a Compton continuum that arises from the higher energy activation products. These are produced a) in the neutron shielding materials that are necessary to contain and collimate the source and b) from the person. Hydrogen, used in our case, as shielding in the form of high density polyethylene, as well as its dominant

presence in the human body provides a large contribution to this Compton background, with emission of a 2.223 MeV gamma ray following neutron capture. In addition, the 478 keV gamma ray from activated borated resin (encasing the collimator arrangement), is another large background contributor.

The main prompt gamma rays used for the measurement technique described in this thesis are the 79.5 and 181.9 keV transitions from neutron capture of ^{157}Gd . In following chapters, it shall be seen that they provide reasonably good detection sensitivity. The spectra and detection limits obtained from these transitions are described in Chapter 2. The 199.2 keV from neutron capture of ^{155}Gd is not used because there is a significant background gamma ray at 197.91 keV from the $^{71\text{m}}\text{Ge}$ isomer produced by the $^{70}\text{Ge}(n, \gamma)$ reaction in the germanium detector. In Figure 1.2 representative spectra in this energy region from high concentration 2 L Gd phantoms are shown. The 197.91 keV peak is a significant component in the prompt gamma ray background and the 199.2 keV peak only becomes noticeable at very high concentrations of Gd. Similarly, the 88.97 keV peak from neutron capture of ^{155}Gd is in close proximity to the lead (Pb) X rays produced from the background photon continuum and so this was not used to measure gadolinium. This spectral region is shown in Figure 1.3. Pb is an important part of the system as gamma ray shielding. Extracting the Gd information from this Pb signal would be complex, and lead to large uncertainties in the estimate. This region would need to be fitted with three Gaussians incorporating the Pb K_{β} X rays and the 88.97 keV peak. In addition, there is a small background peak that would need to be subtracted. In this thesis the 88.97 keV was not incorporated into the spectral analysis as it was thus not expected to improve the sensitivity of the system. This is further demonstrated by the fact that the relative emission probability per neutron capture of the 79.5 keV gamma ray compared to the 88.97 keV gamma ray is approximately 2.9, and the background levels are approximately the same for these two peaks. If the detection limit is proportional to the error in the background divided by the slope (or intensity) then the detection limit for the 88.97 keV peak would be expected to be almost 3 times higher (worse) than that of the 79.5 keV peak. Since the detection limit for the 181.9 keV prompt gamma is significantly better

than the 79.5 keV, if we were to combine the detection limits using the inverse variance weighting method, then the 88.97 keV peak would have a minimal effect on improving the detection limit (ie. it would only improve the detection limit by about 2%). As is also shown in Figure 1.3, the 79.5 keV is surrounded by the Pb K X rays, but as long as the detector resolution is optimized this does not interfere in the analysis of this peak.

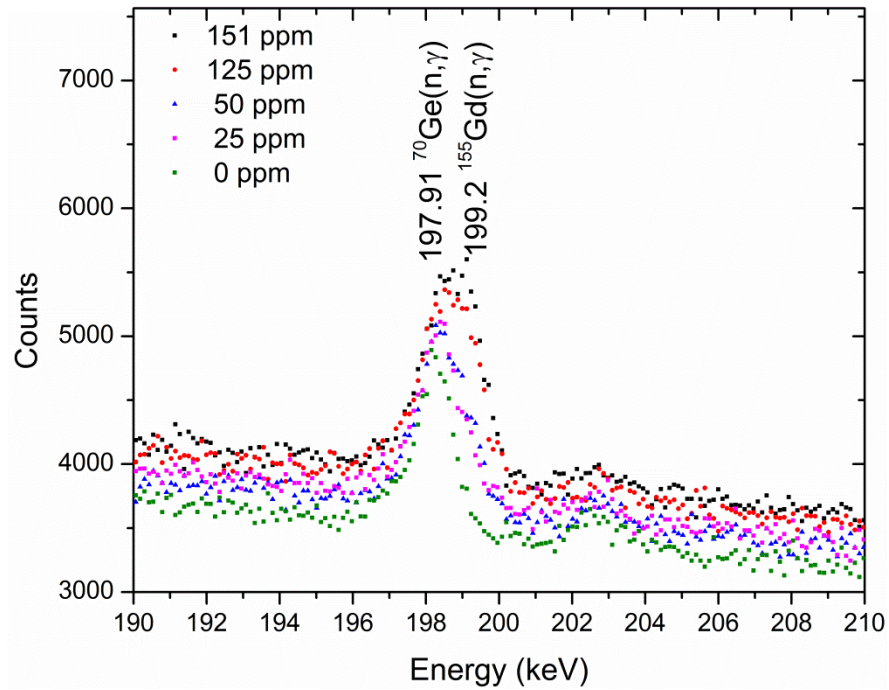


Figure 1.2. Spectra from 2 L Gd phantoms showing the 199.2 keV prompt gamma ray from neutron capture of ^{155}Gd and the interfering background peak at 197.91 keV.

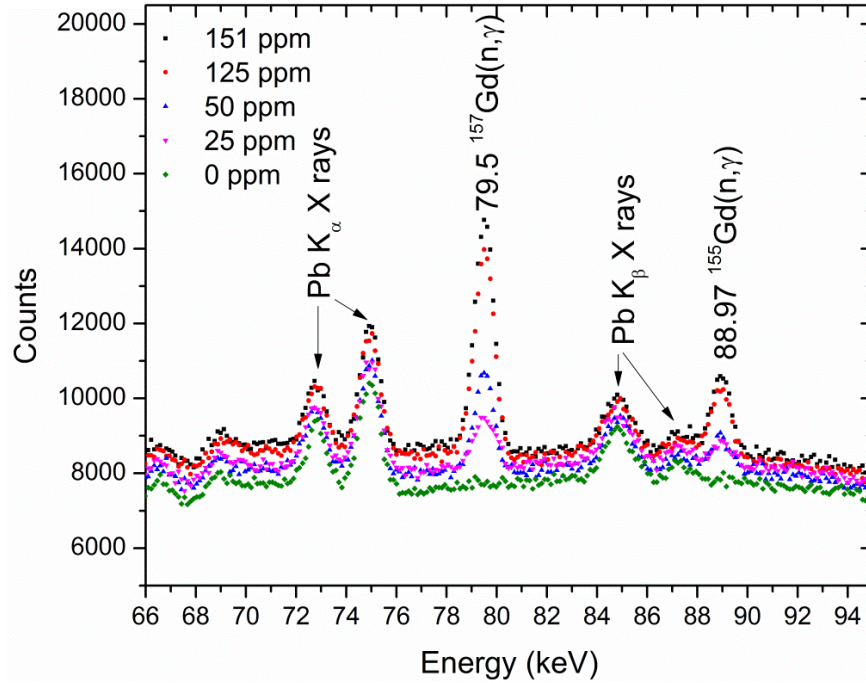
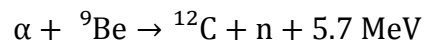


Figure 1.3. Spectra from 2 L Gd phantoms showing the 88.97 and 79.5 keV prompt gamma rays from neutron capture of ^{155}Gd and ^{157}Gd , respectively, and the characteristic Pb K X rays produced in the shielding components.

1.5 $^{238}\text{Pu}/\text{Be}$ source based system

Compared to an accelerator which is subject to operating costs, down-time due to routine maintenance as well as unpredictable operating disruptions that arise because it is a complex piece of machinery that needs active technical support, a $^{238}\text{Pu}/\text{Be}$ neutron source provides a relatively simple and flexible alternative to an accelerator-based neutron source. The source used in this instance is composed of the ^{238}Pu alpha emitter mixed in with a beryllium powder. The (α, n) reaction is described by the following formula:



The $^{238}\text{Pu}/\text{Be}$ neutron source is low maintenance, there is relatively no cost for operation, and the source is always “On” (decaying with half-life of 87.4 years). Although this latter point requires a storage area that is heavily shielded, and a lock-up system for source security, this requirement is achieved with moderate effort. The $^{238}\text{Pu}/\text{Be}$ neutron source has a low gamma ray yield compared to other available isotopic sources, such as $^{241}\text{Am}/\text{Be}$ and ^{252}Cf . One disadvantage for IVNAA is that the $^{238}\text{Pu}/\text{Be}$ neutron source has a broad and relatively high energy spectrum up to 11 MeV with an average neutron energy of ~ 4 MeV (Block et al. 1967). The spectrum from Block et al. (1967) is shown in Figure 1.4. In order for this source to be useful for *in vivo* measurements the neutron beam must be pre-moderated. The term pre-moderated is used here because the neutron beam must first be softened before it enters the target tissue to reduce tissue dose, and subsequently the beam is efficiently moderated by hydrogen *in vivo* to the thermal region with increased probability for thermal neutron absorption in the target tissue or organ. Beryllium (Be) discs encased in aluminum are used in our system as the pre-moderator because of the elastic scattering capability of fast neutrons, and Be also acts as a neutron multiplier via the $^9\text{Be}(n,2n)^8\text{Be}$ reaction (Franklin et al. 1990). In this system, there are two cylindrical neutron sources. The neutron sources are placed in a neutron shielding and collimating apparatus, described in detail in Chapters 2 and 3. The main materials that are used in this apparatus are alternating sheets of steel (iron (Fe)) and polyethylene, a central steel tube collimator encased in graphite, high-Z gamma-ray shielding materials such as tungsten, bismuth and lead, and the whole system is encased in borated resin. Iron (Fe) is a major component in the collimating and shielding apparatus design. The choice of Fe is due to the large cross section for inelastic scatter of fast neutrons by ^{56}Fe , which has a first excited state of 847 keV leading to a neutron energy loss of 1 MeV or more per collision (Franklin et al. 1990). Graphite encases the steel tube to reflect and collimate the neutrons along the central axis of the shielding apparatus. Polyethylene is chosen due to its hydrogen content and the fact that it is easy to shape and contain. Hydrogen is a well known neutron moderating element. Hydrogen’s effectiveness at moderating neutrons is due to its single proton nucleus with approximately the same mass as a neutron. Based on

reaction kinematics for elastic scattering, the energy transfer is proportional to the product of the colliding masses and inversely proportional to the square of the sum of the colliding masses, and as a result, hydrogen (proton) is the most efficient nucleus for energy transfer in a neutron elastic scattering event. Lastly, the borated resin is used due to the relatively large thermal neutron absorption cross section of ^{10}B ($\sim 3800\text{ b}$) to prevent neutron leakage at the system edges.

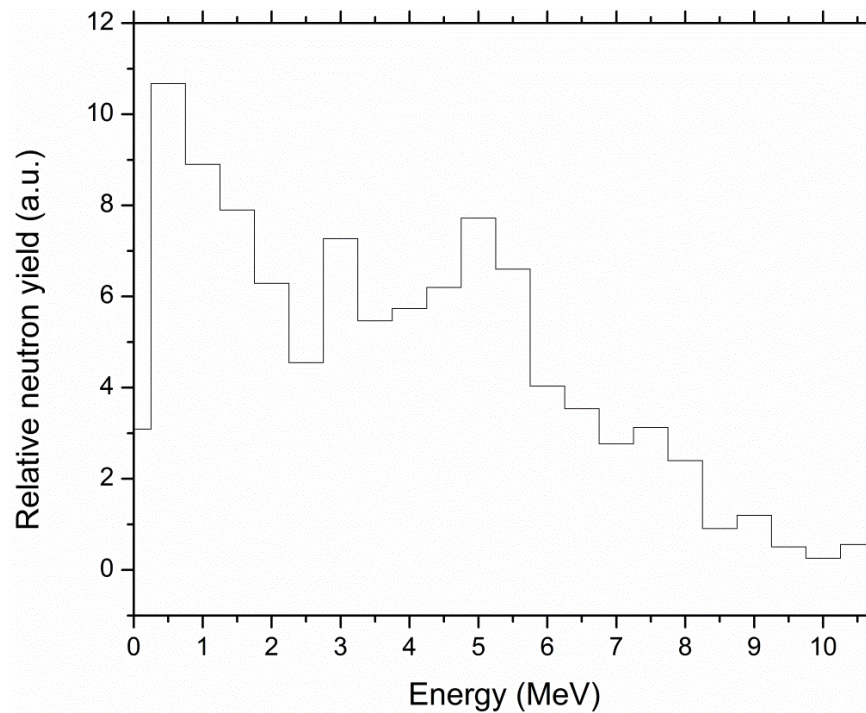


Figure 1.4. Neutron spectrum of the $^{238}\text{Pu}/\text{Be}$ source from Block et al. (1967).

A point that must be considered is the decay of the ^{238}Pu , which will directly affect the neutron yield from the source. A plot of the activity of the ^{238}Pu source used in this thesis is shown in Figure 1.5. The initial combined (both cylindrical sources) source activity was 17.4 Ci in May of 1992, which corresponds to a neutron emission rate of about 4.18×10^7 n/s. At the beginning of this thesis work, in 2007, the source activity had already decayed to 15.4 Ci, with a neutron emission rate of approximately 3.71×10^7 n/s. The long 87.4 yr half-life means that only minor adjustments are required from year to year, but over the course of a few years, adjustments to the neutron emission should be

made. Over the course of this thesis work, the neutron emission rate decreased by a modest factor 1.04. This was taken into account in all simulation work performed using this source.

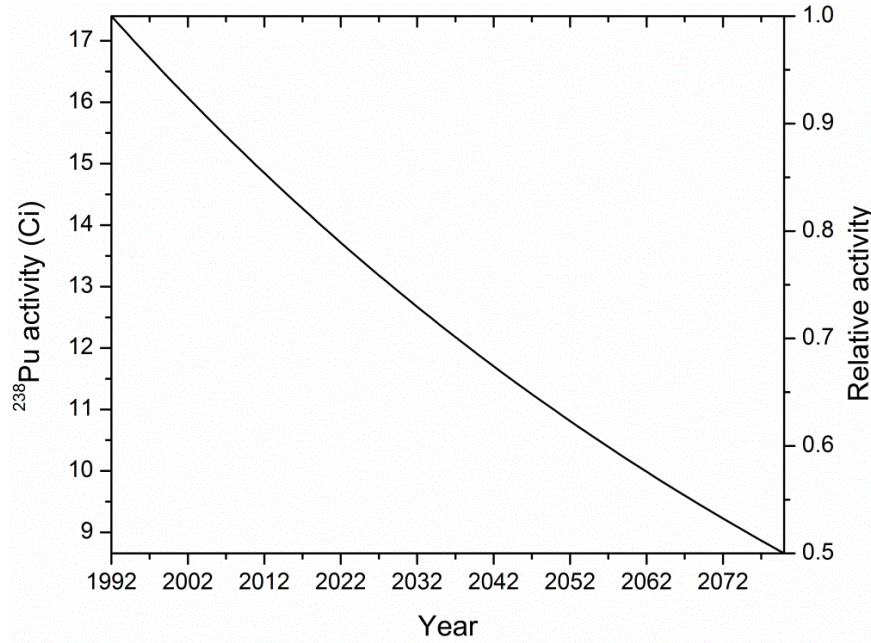


Figure 1.5. Decay curve of the combined activity from the ^{238}Pu sources.

1.6 Gadolinium detection: choice of detector

The ideal detector choice for Gd detection is a detector with good energy resolution at the low energy end of gamma-ray detection, while being of sufficient thickness to detect efficiently the primarily low energy gamma rays following Gd neutron capture, and also being able to withstand repeated neutron exposure. The bulk of the measurements in this thesis were performed using a small volume low energy (LO-AX) n-type Hyperpure Germanium (HPGe) detector (10% relative efficiency, 51700/20-S, ORTEC®). A small n-type detector was chosen because it is less susceptible to neutron damage due to both its small size and reverse electrode configuration (Gilmore 2008).

The n-type detector also has lower photon attenuation because the thick ~ 1 mm Li diffused electrode is located on the inner surface, while the thin ~ 0.3 μm B ion-implanted electrode is the outer entrance contact. The mean free paths in germanium for the Gd photon energies of interest, 40-200 keV, range from 0.03 to 1.1 cm. This detector with a thickness of 2 cm is therefore of sufficient thickness to detect effectively these energies. Further improvements in detection sensitivity would not improve significantly by using a thicker detector but a detector with a larger diameter (ie. greater surface area) could improve the absolute detection efficiency through an increased solid angle.

A thallium activated sodium-iodide NaI(Tl) is not a suitable detector to measure the low energy prompt gamma ray emissions of Gd because it has very poor low-energy resolution ($\sim 10\%$), and in a prompt gamma ray experiment there are many closely spaced low energy photon lines that the NaI detector is unable to resolve. A NaI(Tl) detector for PGNA is better suited to measure very high energy gamma rays, such as in the measurement of total body nitrogen using the 10.8 MeV gamma ray from the $^{14}\text{N}(n, \gamma)$ reaction (Stamatelatos et al. 1992). Neutron capture of ^{157}Gd does produce a high energy gamma ray at 6.750 MeV with an emission probability of approximately 2.4% (IAEA 2007). The spectra obtained with a 5 inch \times 5 inch NaI(Tl) detector (shielded by 2.8 cm of Pb) for 0 and 151 ppm 2 L Gd phantoms are shown in Figure 1.6. In this energy region the 6.750 MeV peak is not of a significant size, even at the high concentration of 151 ppm. It can also be seen that the 2.223 MeV peak counts from the $^1\text{H}(n, \gamma)$ reaction are actually lower by a factor of ~ 1.3 when 151 ppm Gd is present, compared to the zero Gd concentration phantom. This phenomenon is due to the fact that Gd has an enormous neutron absorption cross section compared to the 0.33 b cross section of ^1H , and therefore even with 151 ppm of Gd present, a noticeable reduction in the number of neutron captures on hydrogen is observed. The slightly higher background in the 2.223 MeV region for the 151 ppm Gd spectrum compared to the 0 ppm Gd spectrum is due to Compton continuum from the many high energy prompt gamma rays from Gd.

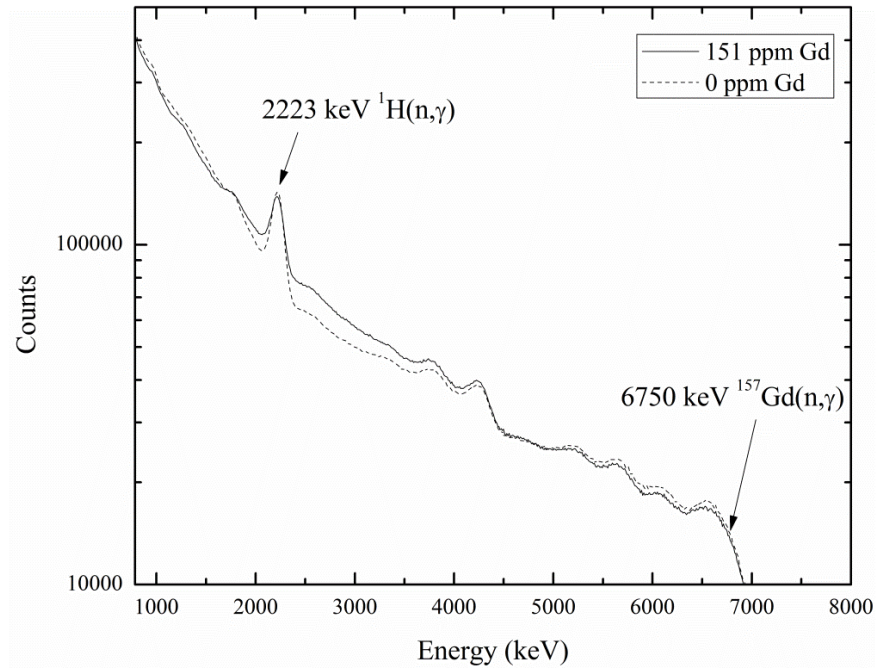


Figure 1.6. Spectra from 0 and 151 ppm 2 L Gd phantoms measured using a NaI(Tl) detector.

1.7 Phantom preparation

The target organs of interest for Gd retention, and for which measurement systems were developed in this thesis, are the kidney, liver, and muscle. The justification and literature review for choosing these target organs are presented in the Introduction section of Article I in Chapter 2. The kidney, liver, and lower leg muscle phantoms were prepared using polyethylene Nalgene® bottles. The kidney phantoms are represented by 125 mL bottles with Gd added by mass, using standard addition methods, from a standard atomic absorption (AA) solution (Sigma-Aldrich, Prod. No. 207136). The 2 L liver and leg muscle phantoms were prepared from the Gd-based contrast agent Omniscan™ (GE Healthcare, gadodiamide). They were also prepared using standard addition methods. Table 1.2 lists the properties of these solutions. It was convenient to prepare these larger phantoms using the GBCA because of the high Gd concentration of Omniscan™ (see

Table 1.2). Fresh Omniscan was also available at no cost as each patient study requires the opening of a new bottle of solution. Significant quantities of material can be left over from individual scans. These were collected from refrigerated storage and used in this study, rather than disposing of the material.

Table 1.2. Properties of the standards used to prepare the Gd phantoms.

Gd standard	ρ (g/cm ³)	Gd concentration (µg/g: ppm)
Atomic absorption	1.01	1005
Omniscan TM	1.15	68410

Since the density of the AA solution and the contrast agent are different from water, the mass of Gd, in g, added to the phantoms is calculated from the following equation:

$$m_{Gd} = \frac{C_p \rho_w \rho_s V_{tot}}{C_s \rho_s - C_p (\rho_s - \rho_w)}$$

where C_p is the desired phantom concentration in µg/g (ppm), ρ_w is the density of water (1 g/cm³), V_{tot} is the total phantom volume, C_s is the standard concentration in ppm, and ρ_s is the density of the standard solution. One drop of HCl was added during preparation of the kidney phantoms. This is standard practice in our laboratory to prevent the element from potentially depositing on the walls of the polyethylene container, which would produce a non-uniform distribution in the phantom. This has been observed with other phantom materials (such as lead and iron solutions in polythene) and has been found to be preventable by acidifying solutions. HCl was not added to the OmniscanTM phantoms as the Gd in these phantoms is chelated and therefore the majority of the Gd solution will be bound with minimal chance for non-uniform deposition or binding to the walls of the polyethylene bottles.

1.8 Thesis preface

Chapter 1 gives an introduction to Gadolinium, the motivation for this thesis, the technique of PGNAA, and describes the phantom preparation. Chapter 2 presents Article I, which describes the feasibility of the detection of gadolinium in the kidney, liver, and lower leg muscle. The introduction section of Article I describes in detail the project motivation and the choice of phantoms for the target tissues of Gd retention. Also given in Article I is a literature review of the concentrations of Gd measured in *ex vivo* tissue samples of humans and animals exposed to a Gd-based MRI contrast agent. Chapter 3 presents Article II which describes a benchmarked Monte Carlo model of our $^{238}\text{Pu}/\text{Be}$ source-based system including the irradiation facility, phantoms, and HPGe detector. Chapter 4 presents Article III which is a continuation of our Monte Carlo work to incorporate the Gd characteristic K X rays that are emitted due to internal conversion electron emission after neutron capture. Additionally, the optimized system detection limits are calculated for varying overlying tissue thicknesses for the kidney and liver using the Monte Carlo model of the Gd prompt gamma rays and K X rays. In Chapter 5 the radiation dosimetry for our system is calculated using the Monte Carlo code MCNP5. The three target organ irradiation geometries are considered in detail. In addition, the kerma from Gd neutron capture is calculated based on kinematics and compared with the available nuclear data. Chapter 6 presents Article IV which describes the results of the first ever *in vivo* pilot study measuring Gd by PGNAA. Chapter 7 describes the application of this system developed for gadolinium to another high neutron absorbing element, samarium. Lastly, the future work and conclusions are discussed in Chapter 8.

Chapter 2

The feasibility of *in vivo* detection of gadolinium by prompt gamma neutron activation analysis following gadolinium-based contrast-enhanced MRI (Article I)

2.1 Introduction to Article I

Article I describes a feasibility study on gadolinium detection in water phantoms representing the kidney, liver, and lower leg muscle. This is the first study published in the scientific literature that looks at the feasibility of the *in vivo* detection of gadolinium by NAA. The introduction contains a literature review of gadolinium retention and toxicity and demonstrates both the project motivation and the motivation behind the choice of the investigated target organs. This paper outlines the detection system, and demonstrates the improvements gained by using the slope of gadolinium signal versus concentration at lower concentrations only, to avoid significant self-shielding and fluence depression. The article also describes a shielded geometry, and a detector which was repaired of neutron damage by thermal annealing.

The experimental work presented in Article I was performed by the author of this thesis under the supervision of Dr. Fiona McNeill, and with the additional guidance of Dr. David Chettle, Dr. Soo Hyun Byun, and Dr. Michael Noseworthy. The manuscript was prepared by the author of this thesis and edited by Drs. Fiona McNeill, Soo Hyun Byun, David Chettle, and Michael Noseworthy.

2.2 Contents of Article I

The following article is reproduced with permission. Copyright © 2011, Elsevier.



The feasibility of *in vivo* detection of gadolinium by prompt gamma neutron activation analysis following gadolinium-based contrast-enhanced MRI

J.L. Gräfe*, F.E. McNeill, S.H. Byun, D.R. Chettle, M.D. Noseworthy

Department of Medical Physics and Applied Radiation Sciences, McMaster University, Hamilton, Ontario, Canada L8S-4K1

ARTICLE INFO

Article history:

Received 8 November 2009

Received in revised form

28 July 2010

Accepted 29 July 2010

Keywords:

In vivo neutron activation analysis

Gadolinium

Toxicity

Detection limit

ABSTRACT

The feasibility of using the McMaster University *in vivo* prompt gamma neutron activation analysis system for the detection of gadolinium has been investigated. Phantoms have been developed for the kidney, liver, and the leg muscle. The initial detection limits are determined to be 7.2 ± 0.3 ppm for the kidney, 3.0 ± 0.1 ppm for the liver, and 2.33 ± 0.08 ppm for the lower leg muscle. A few system optimizations have been tested and show significant detection limit reduction from these initial values. The technique is promising and shows feasibility for *in vivo* studies of gadolinium retention.

© 2010 Elsevier Ltd. All rights reserved.

1. Introduction

Gadolinium (Gd) is a rare earth element of the lanthanide group with atomic number 64. The Gd^{3+} ion shows strong paramagnetic properties, and shortens primarily the T1 relaxation times in the tissues in which it localizes, thus increasing the signal intensity in MRI (Gries, 2002). Free Gd^{3+} is toxic; much of the available toxicity information is based on animal studies of the 'rare earths' or lanthanides as a group with similar toxicological behavior. The lanthanides appear to interact largely with Ca^{2+} due to similar radial sizes (Hirano and Suzuki, 1996), and have been shown to promote calcifying activity in normal animals (Gabbiani et al., 1966). The lanthanides are known to form insoluble hydroxides, phosphates, or carbonates in blood and tissues (Wedeking and Tweedle, 1988; Luckey and Venugopal, 1977). These complexes are deposited in liver, bone, and muscle tissues (Vorobiov et al., 2003). In both rats and mice $GdCl_3$ has been demonstrated to cause necrosis in the liver and spleen, and mineral deposition in these organs as well as in the kidney (Spencer et al., 1997, 1998). The toxicity reviews on lanthanide salts summarize that they are quickly distributed to the kidney, liver, reticuloendothelial system, and slowly transported and retained in bone (Luckey and Venugopal, 1977; Hirano and Suzuki, 1996). The International Commission on Radiological Protection (ICRP) assumes (based on animal retention and toxicity data) a biological half-life of Gd in the

kidneys of 10 days, and 3500 days in the liver and mineral bone (ICRP P30, 1981).

To formulate a clinically safe extravascular MRI contrast agent, Gd is chelated with a suitable ligand, making a complex that has no apparent *in vivo* dissociation (Weinmann et al., 1984). However it is believed that the toxicity of gadolinium-based contrast agents (GBCAs) stems from the amount of free Gd that dissociates from its chelate, and tissue sample studies from patients with severe renal impairment affected by a disease known as nephrogenic systemic fibrosis (Grobner, 2006) have shown high concentrations of Gd (High et al., 2007; Swaminathan et al., 2008). Nephrogenic systemic fibrosis (NSF) is a severe and debilitating disease that affects the skin and systemic organs. The discovery of the disease parallels with the use of GBCAs (Grobner and Prischl, 2007) in the renally impaired. The long-term toxic effects of Gd contrast agents in healthy individuals with no renal impairment are as yet unknown. The long-term retention of Gd in bone has provoked researchers to postulate long-term toxicity of Gd mobilized from bone stores analogous to lead (Pb) regardless of the patient's renal function at the time of administration (Abraham et al., 2008; Thakral et al., 2007). With the possibility of repeated administration in pediatric patients as well as multiple sclerosis patients (who may in some circumstances receive a triple dose; Filippi et al., 1998), and the not uncommon double or triple dose used in magnetic resonance angiography (Swaminathan et al., 2008), it is important to know the residual burden that Gd may impose (Shellock and Kanal, 1999). The objective of this research is to develop a non-invasive method to determine the concentration of Gd deposited in patients with healthy renal function receiving intravenous GBCAs, and to verify all claims for the *in vivo* stability of these agents.

* Corresponding author. Tel.: +1 905 525 9140; fax: +1 905 522 5982.
E-mail address: grafejl@mcmaster.ca (J.L. Gräfe).

The recent literature represents measurements of Gd tissue retention in *ex vivo* samples of humans and animals exposed to GBCAs. The retention values for a few studies are listed in Table 1. The available data are limited to humans diagnosed with NSF and animal studies except for one study by White et al. (2006), who quantified bone retention in samples from healthy patients undergoing hip replacement surgery (see Table 1). To our knowledge there are no published works of *in vivo* measurements on humans. Chelation of Gd alters the pharmacokinetic profile (Aime and Caravan, 2009), and therefore may alter the sites of Gd deposition. On intravenous injection, GBCAs are rapidly distributed to the extracellular spaces and are primarily eliminated by glomerular filtration in the kidneys (Gries, 2002). Depending on the chelating agent there may also be some targeted hepatobiliary excretion for liver imaging (Aime and Caravan, 2009). Initial organs and tissues of interest are the kidney, liver, and muscle. The primary elimination of these contrast agents by glomerular filtration indicates that the kidney may be a suitable target for the *in vivo* quantification of gadolinium. As stated above the liver and bone are sites for long-term storage of free Gd^{3+} . In this paper the liver is investigated as a potential site for residual Gd, although the amount of hepatobiliary excretion of chelated Gd depends on the complex (Aime and Caravan, 2009). Bone was not investigated in this study because accelerator-based techniques may prove to be the best method for quantification in this site (Aslam et al., 2008). A model of the lower leg muscles was chosen for *in vivo* study, not only because of their relatively large muscular size, but also because this is a location far away from any critical organs with reduced radiation exposure risk. In addition, as stated above the lanthanides form complexes with endogenous anions, which can deposit in muscle. Furthermore, in a study of rabbit tissues 5 min post-injection of Gd-DTPA (diethylenetriamine pentaacetic acid), Gd was detected within endothelial cells lining blood vessels of muscle (Noseworthy et al., 2002). This result contradicts the claim for the extracellular nature of these agents. Investigation of the literature indicated, therefore, that the liver, kidney, and muscle could be the potential *in vivo* measurement sites for the assessment of gadolinium retention after exposure to a GBCA. This paper details the results of a preliminary study to determine if radionuclide-based neutron activation analysis could be feasible for *in vivo* measurement of gadolinium in liver, kidney, and lower leg muscle.

2. Methods

The measurement of Gd by neutron activation analysis is based on the 254.000 b thermal neutron capture cross section for the $^{157}Gd(n,\gamma)^{158}Gd$ neutron capture reaction. The stable ^{157}Gd

isotope has a natural abundance of 15.65%. The gamma-rays associated with the reaction are emitted promptly, so irradiation and counting must take place at the same time. The extremely high cross section of ^{157}Gd is counter-balanced by the fact that the reaction primarily emits low-energy gamma-rays that are attenuated within tissue. The simultaneous irradiation and counting set-up means these gamma-rays are located on a high Compton background (resulting from thermal neutron capture on hydrogen) within the experimental spectrum. The most dominant Gd prompt gamma-rays emitted following neutron capture have energies of 79.5 and 181.9 keV with emission probabilities per neutron capture of approximately 10% and 18%, respectively. In this paper, the kidney, liver, and leg muscle Gd concentrations were quantified based on the peak counts from the 79.5 and 181.9 keV gamma-ray emissions.

Simple cylindrical aqueous phantoms were used to simulate the human kidney, liver, and lower leg muscle. The kidney and liver phantoms were placed in a $31 \times 46 \times 46\text{ cm}^3$ polyethylene tank filled with de-ionized water to simulate the human torso. The kidney, liver, and torso phantoms were based on representations used previously for *in vivo* detection of cadmium (Grinyer et al., 2005). The kidney was represented by 0–150 ppm aqueous solutions of Gd in 125 mL polyethylene bottles, placed within the torso phantom. The liver was represented by 0–151 ppm solutions in 2 L polyethylene bottles placed in one position in the torso phantom in a simple geometry. The same 2 L phantoms used to represent the liver were also used on their own outside the water tank as an approximation of the lower leg. Fig. 1a illustrates the irradiation and counting configuration and shows the set-up for the torso and liver phantom. The configuration for a leg phantom is shown in Fig. 1b.

A small coaxial n-type HPGe low-energy photon detector (10% relative efficiency, model LOAX- 51700/20-S, ORTEC) was used to detect the characteristic gamma-rays from gadolinium. This detector is of sufficient size (52 mm diameter \times 20 mm length) to detect the low-energy gamma-rays efficiently at 79.5 and 181.9 keV. The signals from the HPGe detector were processed with a digital pulse processing system (DSA 2000, CANBERRA Industries, Inc.). In the results and discussion and system optimization sections the data will be referred to as acquired in the initial detector state and post-annealing. In the initial detector state there was considerable resolution degradation. This was due to the prolonged exposure of the detector to a fast neutron field. As a consequence, hole-trapping centers were produced within the germanium crystal's active volume (Kraner et al., 1968), therefore degrading the energy resolution due to insufficient charge collection. To repair this type of damage, the detector needs to be annealed (Raudorf et al.,

Table 1

Summary of Gd concentration in *ex vivo* tissue samples from a few studies on humans and animals exposed to a gadolinium-based contrast agent.

Subject(s)	Organ/tissue	Gd concentration (ppm)	Agent dose (mmol/kg)	Reference (year)
Canine	Kidney	2.05 ± 0.17	Gd-DTPA (0.2)	Bartolini et al. (2003)
	Liver	0.47 ± 0.11		
Rat	Kidney	1.37 ± 0.46	Gd-HP-DO3A (0.8)	
Human	Bone	1.77 ± 0.704	Gd-DTPA-BMA (0.1)	White et al. (2006)
	Bone	0.477 ± 0.271	Gd-HP-DO3A (0.1)	
Human ^a	Skin/soft tissue	5–106	N/A	High et al. (2007)
Human ^{a,d}	Skin	411^b , 255^c	Gd-DTPA-BMA (Angiographic dose ^b , multiple ^c)	Swaminathan et al. (2008)
	Kidney	190^b , 395^c		
	Liver	116^b , 108^c		

N/A, not available.

^a Patients diagnosed with nephrogenic systemic fibrosis (NSF).

^b Patient 1 (autopsy).

^c Patient 2 (autopsy).

^d Only a few selected organs are listed here, see reference for concentrations quantified in other organs.

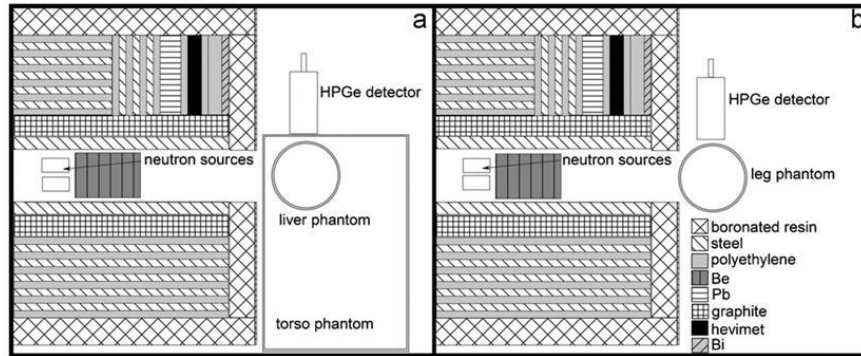


Fig. 1. Diagram of the experimental irradiation and detection geometry for (a) the liver configuration and (b) the leg muscle configuration (top view, not to scale).

1984). The detector was annealed during this feasibility study and improvements to the 79.5 and 181.9 keV peaks are discussed in Section 4.

The neutron source used in this study consisted of two cylindrical $^{238}\text{Pu}/\text{Be}$ sources. The sources are placed into a shielded collimator, described elsewhere (Grinyer et al., 2005; Fedorowicz et al., 1993), which provides a beam with a diameter of approximately 9 cm. The neutron sources were placed 6 cm (from their original position) closer to the collimator exit. This was determined by Grinyer et al. (2005) to be the optimal source position. The torso phantom, containing kidney or liver phantoms, was placed at the end of the collimator (see Fig. 1a.). The 2 L leg phantoms were placed in the direct neutron beam simulating dorsal irradiation of the leg muscle (see Fig. 1b.). The kidney phantoms were placed at 4 cm lateral and dorsal depths in the torso phantom. Torso phantom depth is the distance from the outside of the torso phantom to the midpoint of the organ phantom. In other words depth represents the distance between the skin surface and the midpoint of the organ. The liver phantoms were placed at 7 cm lateral and dorsal depths in the torso phantom. The leg phantoms are placed against the exit face of the collimator. The phantoms of varying Gd concentration are randomly activated. The detector was aligned axially with all phantoms, and spectra were acquired for a 2000 s live time as proposed for *in vivo* measurements. This time was chosen as it has been determined from other *in vivo* studies in our laboratory that this is a suitable *in vivo* measurement time. Subjects are willing to volunteer for a study of this duration, and can comfortably accommodate the measurement. Longer irradiation times lead, of course, to lower detection limits, but both subject participation rates and successful subject measurement rates decline if longer time periods are used.

Peak areas for the measurement were extracted using the data analysis and graphing software OriginPro 8 (OriginLab Corporation), which uses the Levenberg–Marquardt fitting algorithm (Press et al., 1992). An example of the typical spectra acquired in the initial detector state for the 79.5 and 181.9 keV peaks with resulting fits is shown in Fig. 2. The peak areas were fitted with a Gaussian function on a linear background, as shown in Eq. (1). The 79.5 keV peak areas were fitted with Eq. (1), but due to the poor resolution of the detector in the initial detector state the 181.9 keV existed in close proximity to the 186 keV prompt gamma peak from neutron capture of ^{65}Cu . The presence of the ^{65}Cu peak is most likely a result of the neutron activation of the copper cold finger of the HPGe detector. Therefore a double Gaussian function (Eq. (2)) was used to fit both the 181.9 and

186 keV peaks in this spectral region. The 79.5 keV peak exists in a complicated spectral region between unresolved peaks (see Fig. 2). The initial system state is not optimized to fit these peaks confidently; nevertheless the data analysis is included for completeness and comparison with the post-annealed detector results.

$$y = mx + B + \frac{A}{\sigma_1 \sqrt{2\pi}} \exp\left(-\frac{1}{2} \left(\frac{x - x_0}{\sigma_1}\right)^2\right) \quad (1)$$

$$y = mx + B + \frac{A}{\sigma_1 \sqrt{2\pi}} \exp\left(-\frac{1}{2} \left(\frac{x - x_0}{\sigma_1}\right)^2\right) + \frac{C}{\sigma_2 \sqrt{2\pi}} \exp\left(-\frac{1}{2} \left(\frac{x - x_c}{\sigma_2}\right)^2\right) \quad (2)$$

where m is the slope of linear background, B the intercept of linear background, A and C the peak areas, σ_1 and σ_2 the peak widths (standard deviation), x_0 and x_c the peak centroids.

As the number of counts in the peaks decreased, the peak width (σ_1) and the centroid position (x_0) were fixed to the values determined from fitting peaks with high number of counts (Grinyer et al., 2005). To maintain stability of all the fits for the spectra obtained from the pre-annealed detector, the peak widths and centroid positions were randomly constrained to fall within 0.5 standard deviations of the values determined from the highest concentration peaks. Calibration lines of peak area against concentration were created for both the 79.5 and 181.9 keV peaks. Each individual point on the experimental calibration line was an average of three or more data points. As is the convention in our laboratory, the detection limit (M_{DL}) is defined as twice the uncertainty in the zero-concentration phantom peak area, σ_0 , divided by the slope, S (counts/concentration), of the calibration line:

$$M_{DL} = \frac{2\sigma_0}{S} \quad (3)$$

3. Results and discussion

The 79.5 and 181.9 keV calibration lines for the kidney, liver, and leg muscle phantoms are shown in Fig. 3. The points with large relative errors are due to the mechanical difficulty in repositioning the kidney and liver phantoms within the torso phantom. This difficulty will be eliminated in the future with the design of a clamped positioning system. However, this demonstrates the degree of accuracy that will be required in future studies involving patient positioning.

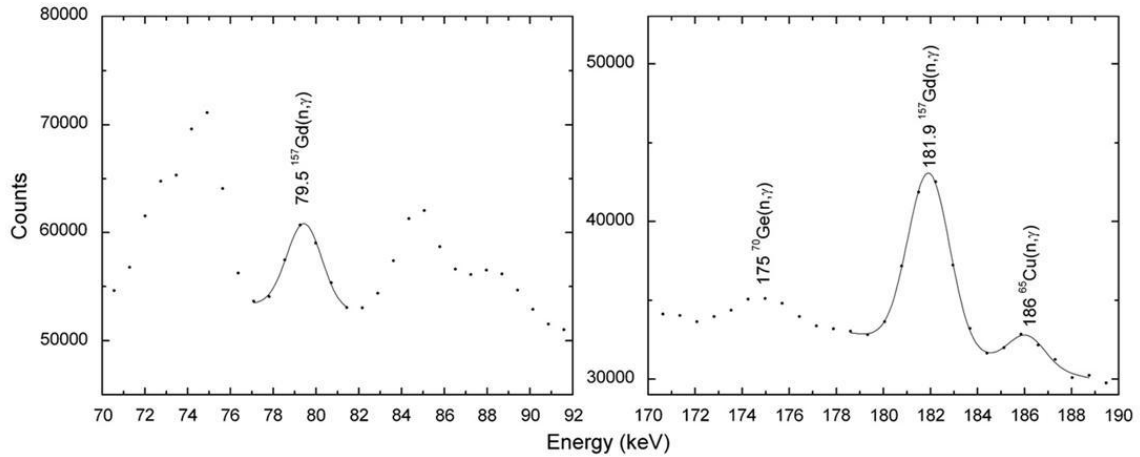


Fig. 2. An example of the spectra obtained in the initial detector state for the 79.5 and 181.9 keV peaks and resulting fits for a 75 ppm Gd 2 L leg phantom.

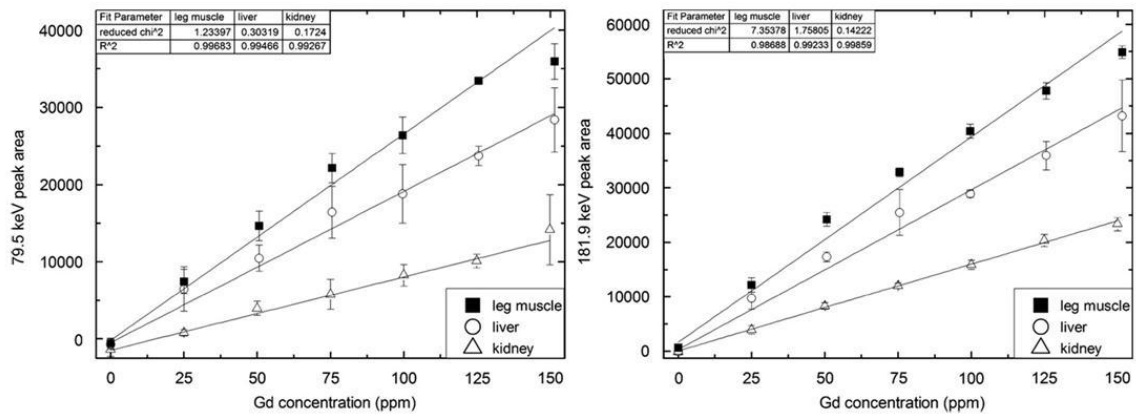


Fig. 3. 79.5 and 181.9 keV calibration lines for the kidney, liver, and leg muscle phantoms.

The data were fit by means of a weighted least-squares linear fit. The liver calibration lines show a highly linear relationship between peak area and Gd phantom concentration with acceptable R^2 and reduced χ^2 values. The calibration lines for the kidney again show a highly linear relationship, but the intercept for the 79.5 keV is offset at -1437 ± 449 counts. This is likely due to the difficulty in fitting this spectral region in the initial detector state. The 79.5 keV peak exists on a high Compton background closely between two peaks on either side that are both not well separated from other peaks (see Fig. 2), and therefore it is difficult to describe the background in this spectral region properly. These surrounding peaks are probably the result of Pb K X rays fluoresced within the Pb shielding that is present in the shielded neutron collimator assembly. This difficulty in background fitting has now been overcome due to improved resolution and separation of the full-energy peaks after the detector annealing (see Fig. 6). The 79.5 keV calibration line for the leg muscle phantom again shows acceptable fit parameters, but the linear fit to the 181.9 keV data shows a rather large reduced χ^2 of 7.4, and shows signs of non-linearity at the higher concentrations. This non-linearity could possibly be due to the extremely large thermal neutron absorption cross section of Gd that could lead to

self-shielding and flux depression phenomena. These phenomena have been seen previously by MCNP simulation in cadmium kidney phantoms (Atanackovic et al., 2007). The non-linearity appears to be more significant at concentrations higher than what is expected for *in vivo* measurement. Therefore in order to describe the sensitivity at levels expected for *in vivo* measurements accurately, lower concentration phantoms need to be made to describe the response in this region. As this is a feasibility study our initial concentrations extending from 0 to 150 ppm are sufficient for the original intentions of this study.

In the initial detector state detection limits were determined for the kidney, liver, and leg muscle. The detection limits from the 79.5 and 181.9 keV signals are listed in Table 2. The combined detection limit in Table 2 was determined via the inverse weighting method. The detection limit for the kidney phantom can be expressed as either a concentration or an absolute mass since its size is smaller than the beam diameter (~ 9 cm), and thus can be fully encompassed in the neutron beam. In addition to expressing the detection limits as a concentration of gadolinium, the detection limits for all organ phantoms were also calculated in terms of the percent of injected dose of gadolinium that a 70 kg person would receive for an MR scan of the central nervous

Table 2

Phantom detection limits for the initial detector state. The M_{DL} is presented as a concentration (and mass in the case of the kidney) as well as the percent of the injected dose (% ID) for three GBCAs.

Location	79.5 keV M_{DL} (ppm)	181.9 keV M_{DL} (ppm)	Combined M_{DL} (ppm)	M_{DL} (% ID)
Kidney (125 mL) ^a	19 ± 2 (2.3 ± 0.2 mg)	7.8 ± 0.4 (0.97 ± 0.05 mg)	7.2 ± 0.3 (0.90 ± 0.04 mg)	0.081 ± 0.003
Liver (2 L) ^b	7.1 ± 0.4	3.3 ± 0.1	3.0 ± 0.1	0.54 ± 0.02
Leg (2 L muscle)	5.0 ± 0.1	2.6 ± 0.1	2.33 ± 0.08	0.42 ± 0.01

^a 4 cm lateral and dorsal depths.

^b 7 cm lateral and dorsal depths.

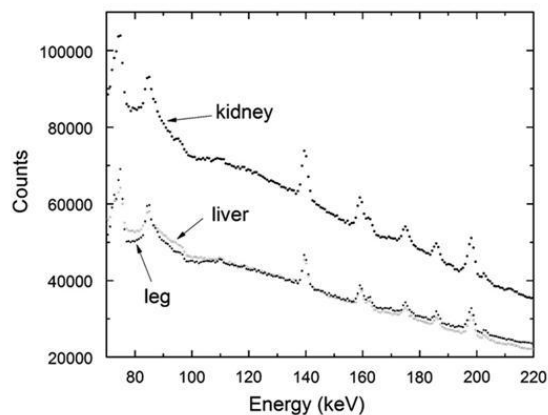


Fig. 4. Representative zero-concentration spectra for the kidney, liver, and leg muscle phantoms. The higher background in the kidney spectrum is due to the shallow kidney depth, which requires the detector to be placed in the closest position to the neutron shielding and collimating apparatus.

system for three GBCAs (OmniscanTM—gadodiamide, Magnevist[®]—gadopentetate dimeglumine, Gadovist[®]—gadobutrol). Although the confidence in the 79.5 keV peak fitting of the spectra acquired from the detector in the initial state is weak, using the 79.5 keV signal only reduces the combined detection limit by at most 12%.

The reason for the higher kidney detection limit as compared to the liver and leg muscle phantoms is twofold: (a) the smaller size (125 mL) of the kidney leads to a smaller absolute Gd content, which results in a lower sensitivity and (b) the background for the kidney detection configuration is the largest due to the shallow depth (within the torso phantom) kidney irradiation geometry, which requires the detector to be placed in the closest position to the collimator. The 0 ppm (background) spectra for the kidney, liver, and lower leg muscle phantoms are shown in Fig. 4.

The above detection limits can be obtained for a neutron skin dose of approximately 0.5 mSv (Grinyer et al., 2005). The detection limits of our system show that if a very small percentage of Gd is retained it will be detectable. Although the data are limited, these detection limits approach values for retention from the literature (see Table 1). The bone retention data of White et al. (2006) suggest that the amount retained for gadodiamide (Gd-DTPA-BMA) in bone is about 1–2% of the injected dose (Aime and Caravan, 2009). Although bone is not one of our initial target tissues in this study, these values give insight into the retention of Gd in healthy volunteers after Gd contrast agent administration. In the future complementary analysis of *in vivo* Gd bone content and organ systemic distribution with time may give more information on the redistribution and toxicity of free Gd in the body. Furthermore, High et al. (2007) and

Swaminathan et al. (2008) found significant Gd concentrations in patients with nephrogenic systemic fibrosis (see Table 1). Admittedly these concentrations are for a group of patients with severe renal impairment who have received GBCAs, which is not our target patient population. Nevertheless, this gives further insight into the order of magnitude possible for Gd retention in human tissues. Gd is a biologically non-essential element, and humans are exposed to Gd only through GBCAs. Unlike other studies of biologically non-essential *in vivo* aluminum burden (Davis et al., 2008) and biologically essential magnesium (Aslam et al., 2008; to name but two) there is no standard minimum value to which to set the goal of the detection limits for Gd. Therefore we can only infer from the available retention studies that the initial detection limits of this technique approach appropriate values and with a few optimizations could reach appropriate levels for clinical measurements.

4. System optimization

Although the initial system was not entirely optimized for Gd detection due to the degraded resolution of the detector and high Compton background, the initial system allowed for an estimation of the feasibility of *in vivo* detection of Gd. This section discusses a few simple system upgrades that significantly optimize the system and improve the feasibility of measurement. The system is optimized using the 2 L leg phantoms because of their ease of use, but the improvements can potentially be applied to all organs of interest. The turnover of the calibration lines was noticed most significantly in the leg phantoms. To investigate the improvement in sensitivity in the assumed linear region more 2 L Gd phantoms were prepared at 2, 5, and 10 ppm.

There is a large background of gamma-ray contribution to the Compton continuum in the low-energy Gd prompt gamma-ray peak regions produced from neutron interactions in the materials of the collimating and shielding apparatus. A 20 cm × 33 cm Pb shield with a thickness of 2.5 cm was introduced between the collimator and the HPGe detector. This Pb shield significantly reduced the background level as shown in Fig. 5. A major reduction was seen in the size of the Doppler broadened 478 keV prompt gamma-ray peak from neutron capture of ¹⁰B in the boronated resin encasing the collimating apparatus (see Fig. 1).

The above detection limits were achieved with a detector that needed annealing. The detector resolution has recently been improved by the annealing process. The resolution improvements to the 79.5 and 181.9 keV lines are shown in Table 3. The improvements in spectral resolution are shown in Fig. 6 for 5 and 25 ppm 2 L leg phantoms with the detector shielded by Pb. The improvements in resolution provide better separation of the full-energy peaks for improved fitting of the 79.5 keV peak, and the 181.9 keV peak is now well separated from the 186 keV ⁶⁵Cu peak

so that it can be fit with a single Gaussian function as described in Eq. (1).

The zero-concentration phantom peak area uncertainty (σ_0) in Eq. (3) is proportional to the square root of the background. The amount of background underlying a full-energy peak is proportional to the peak resolution and the background level. The respective average background levels for the 2 L leg muscle geometry have been reduced by a factor of ~ 1.32 , and 1.64 in the

79.5 and 181.9 keV peak regions, and the resolution improvements are given in Table 3. The expected reduction factors in the zero-concentration phantom peak area uncertainties are 1.62 ± 0.09 and 1.70 ± 0.06 , and the observed reductions from the fits were 1.80 ± 0.03 and 1.69 ± 0.06 for the 79.5 and 181.9 keV peak regions, respectively.

To avoid any neutron self-attenuation effects due to the enormous neutron capture cross section of Gd, the sensitivity for the leg phantoms was determined based on 0, 2, 5, 10, and 25 ppm phantoms (instead of 0–150 ppm above). The slope of the calibration line increased by a factor of approximately 1.75 for the 79.5 keV line, and by a factor of approximately 1.46 for the 181.9 keV line. Both lines show an increase in slope due to the reduced neutron self-attenuation at lower Gd concentrations. The larger increase for the 79.5 keV line is due to the improved fitting after the detector annealing. With the improved resolution, reduced background, and larger slope for the lower concentration phantoms the detection limits improve by a factor of 3.1 and 2.5 to 1.59 ± 0.03 and 1.07 ± 0.03 ppm for the 79.5 and 181.9 keV peaks, respectively. The combined improved detection limit for the leg muscle is 0.89 ± 0.02 ppm.

Similar improvements to the leg muscle detection limits are expected for the kidney and liver. Although the non-linearity (from Gd neutron self-attenuation) observed in the leg was not as evident in the initial calibration lines for the kidney and liver, the background reduction and improved resolution will greatly benefit the detection limit reduction by a factor of about 1.7. Future work will incorporate the determination of the detection limits as a function of organ depth (overlying tissue thickness) to determine the sensitivity of this measurement over a wide range of patient body types.

5. Conclusions

Detection limits for gadolinium concentration in three target organs in anthropomorphic phantoms have been determined. The results of this preliminary study show that the *in vivo* detection of gadolinium following contrast-enhanced MRI by prompt gamma neutron activation analysis is feasible, as detection limits approach concentrations previously assayed by biopsy measurements. These detection limits can be obtained for an acceptable neutron skin dose of about 0.5 mSv. Future work could

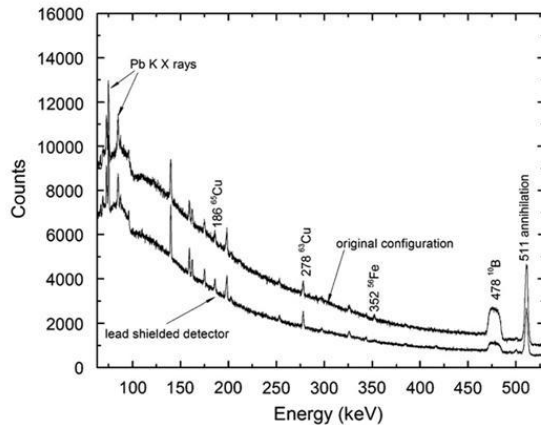


Fig. 5. Spectra of 0 ppm leg phantoms showing the background reduction from the Pb detector shield. Many of the low-energy peaks between ~ 140 and 200 keV are from the isomeric states of the Ge isotopes produced by neutron reactions in the detector (Bunting and Kraushaar, 1974). The spectra were obtained with the annealed detector. Note the total number of channels on the multichannel analyzer (MCA) has been changed from 4096 to 8192.

Table 3
Comparison of the HPGe detector resolution before and after annealing.

Energy (keV)	Full width at half maximum (FWHM) (keV)	
	Initial	Annealed detector
79.5	1.9 ± 0.2	0.96 ± 0.03
181.9	2.0 ± 0.1	1.14 ± 0.03

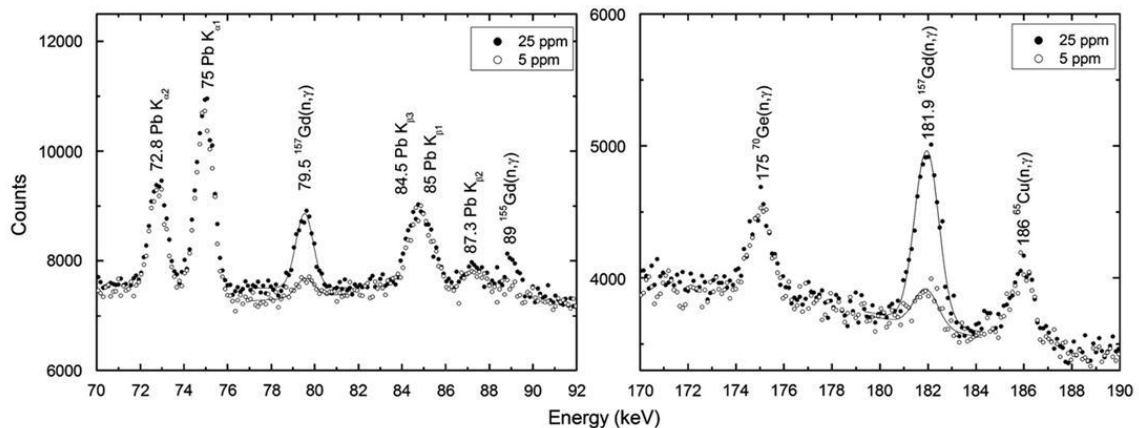


Fig. 6. An example of the spectra obtained after the detector annealing and with the detector shielded by 2.5 cm of Pb. The spectra show the 79.5 and 181.9 keV peaks with the resulting fits for 5 and 25 ppm Gd 2 L leg phantoms. Note the total number of channels on the multichannel analyzer (MCA) has been changed from 4096 to 8192.

considerably improve the technique. For example, the investigation of the detection limit improvements by modification of an MCNP model (Atanackovic et al., 2007) of the $^{238}\text{Pu}/\text{Be}$ system could aid in further developing the measurement.

Acknowledgements

The authors would like to thank Alice Pidruczny and John Avelar of the McMaster Nuclear Reactor for providing the detector annealing services. The Natural Sciences and Engineering Research Council of Canada funded this research.

References

- Abraham, J.L., Thakral, C., Skov, L., Rossen, K., Marckmann, P., 2008. Dermal inorganic gadolinium concentrations: evidence for in vivo transmetallation and long-term persistence in nephrogenic systemic fibrosis. *Br. J. Dermatol.* 158, 273–280.
- Aime, S., Caravan, P., 2009. Biodistribution of gadolinium-based contrast agents, including gadolinium deposition. *J. Magn. Reson. Imaging* 30, 1259–1267.
- Aslam, Pejović-Milić, A., McNeill, F.E., Byun, S.H., Prestwich, W.V., Chettle, D.R., 2008. In vivo assessment of magnesium status in human body using accelerator-based neutron activation measurement of hands: a pilot study. *Med. Phys.* 35, 608–616.
- Atanackovic, J., Grinyer, J., Chettle, D.R., Byun, S.H., 2007. The comparison of two MCNP models used for prompt gamma in vivo detection of cadmium and mercury. *Nucl. Instrum. Methods Phys. Res. B* 263, 169–174.
- Bartolini, M.E., Pekar, J., Chettle, D.R., McNeill, F., Scott, A., Sykes, J., Prato, F.S., Moran, G.R., 2003. An investigation of the toxicity of gadolinium based MRI contrast agents using neutron activation analysis. *Magn. Reson. Imaging* 21, 541–544.
- Bunting, R.L., Kraushaar, J.J., 1974. Short-lived radioactivity induced in Ge(Li) gamma-ray detectors by neutrons. *Nucl. Instrum. Methods* 118, 565–572.
- Davis, K., Aslam, Pejović-Milić, A., Chettle, D.R., 2008. In vivo measurement of bone aluminum in population living in southern Ontario, Canada. *Med. Phys.* 35, 5115–5123.
- Fedorowicz, R.P., Chettle, D.R., Kennett, T.J., Prestwich, W.V., Webber, C.E., 1993. A $^{238}\text{Pu}/\text{Be}$ facility for in vivo cadmium measurements. In: Ellis, K.J., Eastman, J.D. (Eds.), *Human Body Composition*. Plenum Press, New York.
- Filippi, M., Rovaris, M., Capra, R., Gasperini, C., Yousty, T.A., Sormani, M.P., et al., 1998. A multi-centre longitudinal study comparing the sensitivity of monthly MRI after standard and triple dose gadolinium–DTPA for monitoring disease activity in multiple sclerosis. Implications for phase II clinical trials. *Brain* 121, 2011–2020.
- Gabbiani, G., Jacqmin, M.L., Richard, R.M., 1966. Soft-tissue calcification induced by rare earth metals and its prevention by sodium pyrophosphate. *Br. J. Pharmacol. Chemother.* 27, 1–9.
- Gries, H., 2002. Extracellular MRI contrast agents based on gadolinium. *Top. Curr. Chem.* 221, 1–24.
- Grinyer, J., Byun, S.H., Chettle, D.R., 2005. In vivo prompt gamma neutron activation analysis of cadmium in the kidney and liver. *Appl. Radiat. Isot.* 63, 475–479.
- Grobner, T., 2006. Gadolinium—a specific trigger for the development of nephrogenic fibrosing dermopathy and nephrogenic systemic fibrosis? *Nephrol. Dial. Transplant.* 21 1104–1108.
- Grobner, T., Prischl, F.C., 2007. Gadolinium and nephrogenic systemic fibrosis. *Kidney Int.* 72, 260–264.
- High, W.A., Ayers, R.A., Cowper, S.E., 2007. Gadolinium is quantifiable within the tissue of patients with nephrogenic systemic fibrosis. *J. Am. Acad. Dermatol.* 56, 710–712.
- Hirano, S., Suzuki, K.T., 1996. Exposure, metabolism, and toxicity of rare earths and related compounds. *Environ. Health Perspect.* 104 (Suppl. 1), 85–95.
- ICRP P30, 1981. Limits for intakes of radionuclides by workers. *Ann. ICRP* 6, 67–69.
- Kraner, H.W., Chasman, C., Jones, K.W., 1968. Effects produced by fast neutron bombardment of Ge(Li) gamma ray detectors. *Nucl. Instrum. Methods* 62, 173–183.
- Luckey, T.D., Venugopal, B., 1977. *Metal Toxicity in Mammals I—Physiologic and Chemical Basis for Metal Toxicity*. Plenum Press, New York.
- Noseworthy, M.D., Ackerley, C., Qi, X., Wright, G.A., 2002. Correlating subcellular contrast agent location from dynamic contrast-enhanced magnetic resonance imaging (dMRI) and analytical electron microscopy. *Acad. Radiol.* 9 (Suppl. 2), S514–S518.
- Press, W.H., Teukolsky, S.A., Vetterling, W.T., Flannery, B.P., 1992. *Numerical Recipes in C* second ed. Cambridge University Press, Cambridge.
- Raudorf, T.W., Trammell, R.C., Wagner, S., 1984. Performance of reverse electrode HPGe coaxial detectors after light damage by fast neutrons. *IEEE Trans. Nucl. Sci.* NS 31, 253–257.
- Shellock, F.G., Kanal, E., 1999. Safety of magnetic resonance imaging contrast agents. *J. Magn. Reson. Imaging* 10, 477–484.
- Spencer, A.J., Wilson, S.A., Batchelor, J., Reid, A., Rees, J., Harpur, E., 1997. Gadolinium chloride toxicity in the rat. *Toxicol. Pathol.* 25, 245–255.
- Spencer, A., Wilson, S., Harpur, E., 1998. Gadolinium chloride toxicity in the mouse. *Hum. Exp. Toxicol.* 17, 633–637.
- Swaminathan, S., High, W.A., Ranville, J., Horn, T.D., Hiatt, K., Thomas, M., et al., 2008. Cardiac and vascular metal deposition with high mortality in nephrogenic systemic fibrosis. *Kidney Int.* 73, 1413–1418.
- Thakral, C., Alhariri, J., Abraham, J.L., 2007. Long-term retention of gadolinium in tissues from nephrogenic systemic fibrosis patient after multiple gadolinium-enhanced MRI scans: case report and implications. *Contrast Media Mol. Imaging* 2, 199–205.
- Vorobiov, M., Basok, A., Tovbin, D., Shnaider, A., Katchko, L., Rogachev, B., 2003. Iron-mobilizing properties of the gadolinium–DTPA complex: clinical and experimental observations. *Nephrol. Dial. Transplant.* 18, 884–887.
- Wedeking, P., Tweedle, M., 1988. Comparison of the biodistribution of ^{153}Gd -labeled $\text{Gd}(\text{DTPA})^{3-}$, $\text{Gd}(\text{DOTA})^{-}$, and $\text{Gd}(\text{acetate})_3$ in mice. *Nucl. Med. Biol.* 15, 395–402.
- Weinmann, H.J., Brasch, R.C., Press, W.R., Wesbey, G.E., 1984. Characteristics of gadolinium–DTPA complex: a potential NMR contrast agent. *Am. J. Roentgenol.* 142, 619–624.
- White, G.W., Gibby, W.A., Tweedle, M.F., 2006. Comparison of $\text{Gd}(\text{DTPA-BMA})$ (Omniscan) versus $\text{Gd}(\text{HP-DO3A})$ (ProHance) relative to gadolinium retention in human bone tissue by inductively coupled plasma mass spectroscopy. *Invest. Radiol.* 41, 272–278.

Chapter 3

A benchmarked MCNP model of the *in vivo* detection of gadolinium by prompt gamma neutron activation analysis (Article II)

3.1 Introduction to Article II

Article II describes the Monte Carlo simulations of our source-based Gd detection system using MCNP Version 5. This article describes a Monte Carlo model of the HPGe detector that was used experimentally. The model was developed from experimental data obtained using various gamma-ray point sources available in our laboratory. This detector model was then combined with a modified version of a model of the $^{238}\text{Pu}/\text{Be}$ source-based NAA system. The original geometry model of the source-based system was developed by Dr. Jovica Atanackovic, who kindly provided the code. Modifications were made by the author of this thesis. Excellent agreement was found between the measured and simulated Gd detection sensitivity on a per source neutron basis. In other words, no normalization of the Monte Carlo work to experiment was necessary. The creation of a benchmarked Monte Carlo model allows for the simulation of many more irradiation geometries, shielding and moderating materials and configurations than could be studied experimentally. A benchmarked and verified model also allows for more efficient work, because the amount of experimental work required to determine an ideal set-up is reduced. Once the ideal set-up is determined via simulation it can then be re-verified experimentally. A system design methodology that efficiently combines simulation and experiment reduces operator radiation exposures. It also reduces the neutron damage to the HPGe detector. Finally, a Monte Carlo model of the system can be used to determine the dosimetry for various irradiation conditions and geometries, and the dose rates to the organs at risk. A full understanding of the dosimetry of the system is difficult, if not

impossible, to obtain by experiment alone. For all of these reasons, a benchmarked Monte Carlo model was a significant contribution to the overall goals of this thesis.

The experimental and simulation work in Article II was performed by the author of this manuscript under the supervision of Dr. Fiona McNeill and under the additional guidance of Dr. Soo Hyun Byun and Dr. David Chettle. The initial idea to simulate the detection of Gd in two parts (neutron capture and subsequent gamma ray detection) was suggested by Dr. Soo Hyun Byun. The manuscript was prepared by the author of this thesis and edited by Drs. Fiona McNeill, Soo Hyun Byun, David Chettle, and Michael Noseworthy.

Article's I and II were submitted for publication at the same time. The review process was faster for Article II and therefore it was accepted for publication first. The articles are not presented in order of publication date in this thesis because it is better for the flow of the thesis to present the articles in the order of experimental design, then simulation of experimental design.

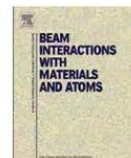
3.2 Contents of Article II

The following article is reproduced with permission. Copyright © 2010, Elsevier.



Contents lists available at ScienceDirect

Nuclear Instruments and Methods in Physics Research B

journal homepage: www.elsevier.com/locate/nimb

A benchmarked MCNP model of the *in vivo* detection of gadolinium by prompt gamma neutron activation analysis

J.L. Gräfe*, F.E. McNeill, S.H. Byun, D.R. Chettle, M.D. Noseworthy

Department of Medical Physics and Applied Radiation Sciences, McMaster University, Hamilton, Ontario, Canada L8S 4K1

ARTICLE INFO

Article history:

Received 30 November 2009

Received in revised form 1 March 2010

Available online 14 April 2010

Keywords:

In vivo neutron activation analysis

Gadolinium

Monte Carlo simulation

Ge detector

ABSTRACT

Gadolinium (Gd)-based contrast agents are a valuable diagnostic aid for magnetic resonance imaging (MRI). The amount of free Gd deposited in tissues following contrast enhanced MRI is of toxicological concern. The McMaster University *in vivo* prompt gamma neutron activation analysis facility has been adapted for the detection of Gd in the kidney, liver, and the leg muscle. A simple model of the HPGe detector used for detection of the prompt γ -rays following Gd neutron capture has been created using Monte Carlo simulation. A separate simulation describing the neutron collimation and shielding apparatus has been modified to determine the neutron capture rate in the Gd phantoms. The MCNP simulation results have been confirmed by experimental measurement. The deviations between MCNP and the experiment were between 1% and 18%, with an average deviation of $3.8 \pm 6.7\%$. The validated MCNP model is to be used to improve the Gd *in vivo* measurement sensitivity by determining the best neutron moderator/reflector arrangement.

© 2010 Elsevier B.V. All rights reserved.

1. Introduction

Gadolinium-based contrast agents (GBCA) provide a remarkable improvement in the overall efficacy of MR diagnoses. The continual and widespread use of these contrast agents motivates the need for short and long term toxicology studies. The free Gd^{3+} ion is toxic, and therefore must be chelated with an organic ligand to reduce the *in vivo* toxicity. The amount of dissociation of the Gd^{3+} ion from its chelate, presents a concern for the safety of GBCA [1]. At McMaster University, developmental work [2] is being carried out to determine the *in vivo* concentration of gadolinium by prompt gamma neutron activation analysis (PGNAA) following gadolinium contrast enhanced MRI. The experimental site, initially developed for the measurement of cadmium in the kidney and liver [3,4], has been adapted to detect gadolinium in the same tissues as well as in the lower leg muscle. The biological half-life of these agents is approximately 1–2 h [5]. The Gd chelates are excreted from the body in un-metabolized form via renal filtration at greater than 99%. The small remainder is eliminated from the body via hepatic biliary excretion [6]. The *in vivo* measurement will be performed after a suitable clearance period. Previous *ex vivo* tissue studies have found Gd retention of the order of parts per million (ppm) [7–9]. Our feasibility study [2] demonstrates that we can detect Gd *in vivo* by PGNAA at less than 1% (ppm level) of the injected dose (~ 1.1 g Gd for an average 70 kg person) for a

standard scan, in the kidney, liver and lower leg muscle, in our simple water-based human phantoms.

The naturally occurring Gd isotope with the largest cross section for thermal neutron capture is ^{157}Gd ($a = 15.65\%$, $\sigma_0 = 254\,000$ b) [10]. Taking into account the product of the isotopic abundance (a), neutron capture cross section (σ_0) and γ -ray emission probability, γ -rays of energy 79.5 and 181.9 keV from de-excitation of $^{158}\text{Gd}^*$ are the most prominent in the spectrum following neutron capture by Gd. PGNAA requires the simultaneous irradiation and detection of these γ -rays with the use of a HPGe detector.

The Monte Carlo N-particle (MCNP) code has proven to be an extremely useful tool in the field of radiation physics. The ultimate goal in this present work is twofold (a) to use MCNP Version 5 [11] to simulate the *in vivo* gadolinium measurement system and validate the code against experimental measurements, and (b) determine the effects on gadolinium measurement sensitivity of variations to experimental parameters.

2. Gadolinium measurement system

To model the experimental results, both the neutron capture of gadolinium and detection of the characteristic γ -rays must carefully be considered. MCNP is used in two separate files to model first the neutron transport and prompt γ -ray production in the Gd measurement system, and then secondly the detection of the ^{157}Gd prompt γ -rays with a HPGe detector.

The PGNAA system consists of four main components: neutron sources, a shielding and collimating apparatus, human organ

* Corresponding author. Tel.: +1 905 525 9140/26328; fax: +1 905 522 5982.
E-mail address: grafejl@mcmaster.ca (J.L. Gräfe).

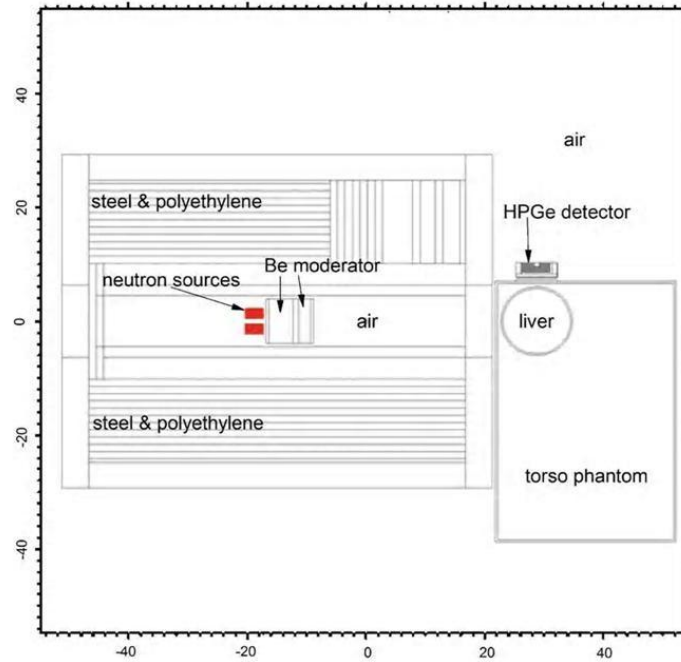


Fig. 1. MCNP geometry of the irradiation and detection system with the liver and torso irradiation geometry shown (dimensions in cm). The shaded region of the HPGe detector represents the active germanium volume.

phantoms, and a HPGe detector. The MCNP geometry of the system configuration is shown in Fig. 1. Two cylindrical ^{238}Pu /Be neutron sources with a total ^{238}Pu activity of 15.3 Ci are placed into the shielded collimator. The shielding and collimation apparatus is fully described elsewhere [3,4], suffice it to say the shielding comprises alternating layers of steel and polyethylene with a central steel tube collimator which in turn is surrounded by a graphite block. The $^9\text{Be}(\alpha, n)^{12}\text{C}$ reaction of the source produces neutrons with energies up to 11 MeV, with distribution such that the average neutron energy is about 4 MeV [12]. The neutron energy spectrum is pre-moderated/multiplied by placing two beryllium discs with a total thickness of 6 cm directly into the collimator.

A polyethylene torso phantom filled with de-ionized water is placed at the collimator exit, and aqueous 125 mL kidney or 2 L liver polyethylene phantoms doped with known concentrations of Gd are placed within it (see Fig. 1). The lower leg muscle irradiation is simulated by placing the 2 L phantoms representing the lower leg directly against the exit face of the collimator. The phantom measurements were made with a single small volume HPGe low energy photon detector (10% relative efficiency, model ORTEC LOAX 51700/20-S, see Table 2 for dimensions). The detector is an n-type Ge semiconductor crystal and is of a closed-ended coaxial geometry. The detector is placed at the exit of the collimator out of the main neutron beam and is aligned axially with all phantoms. The phantom measurements are performed for a fixed live time of 2000 s [2].

3. Detector efficiency

The first step in modeling the experimental results is to determine the detector full-energy peak efficiency (FEPE). Several sources were used to cover the energy region of 59.5–1005 keV,

and consisted of a ^{241}Am source, a ^{137}Cs source, and a mixed ^{152}Eu , ^{154}Eu , ^{155}Eu source. The energy lines, emission probabilities, and half-lives are shown in Table 1 [13]. The energy line at ~ 86.5 keV is the combination of the two emissions shown in the table. The uncertainty in the activity of the ^{137}Cs source is given as 3.7%, the europium source is 5%, and the ^{241}Am source error could not be located, so a 5% error was arbitrarily assumed for this source. These sources are aligned axially with the detector face and placed at a distance of 10 cm (using calipers) from the plastic protective detector window cap. All Gd phantom measurements are performed with the plastic cap present, for consistency the efficiency calculations are performed in the same manner.

In order to extract the full-energy peak areas the acquired spectra were fitted using a Gaussian curve, for the full-energy peak, on a linear background. However, due to the effects of γ -ray Compton scatter in the detector housing materials, and electrons escaping the detector active volume described in Ref. [14], there may exist a step in the background. Also because of long exposure of the germanium crystal to a fast neutron field, there were observed low en-

Table 1
Experimental sources used in the efficiency calibration covering 59.5–1004.7 keV.

Nuclide	Energy (keV)	Emission probability	Half-life (days)
^{241}Am	59.54	0.3578	$(1.5785 \pm 0.0023) \times 10^5$
^{137}Cs	661.66	0.8499	$(1.099 \pm 0.004) \times 10^4$
^{152}Eu	344.28	0.2658	4941 ± 7
	411.12	0.02237	
^{154}Eu	1004.73	0.1785	3138.1 ± 1.4
^{155}Eu	86.06	0.00154	1736 ± 6
	86.55	0.307	
	105.31	0.211	

Data from [13].

ergy tailing effects. These peaks were then fitted with a much more complicated function which included an exponential low energy tail and a smoothed step function [15]. The log–log plot of the measured efficiencies determined from the ratio of the measured peak counting rate to source photon emission rate versus energy is shown in Fig. 2.

3.1. Simple detector model

Monte Carlo simulations have been used by R.G. Helmer et al. to model a germanium detector's efficiency to an accuracy of about 0.2% from 50 to 1400 keV [14]. The degree of precision required for the model in this work is of the order 5%, since the calibration source activities and the gadolinium peak area variations are generally of this order. An accurate detector simulation relies heavily on the total active volume of the germanium crystal, and the position of the germanium crystal within the aluminum capsule. Many researchers have discovered significant discrepancies in the manufacturer specified parameters [16–18]. These parameters include dead-layer thicknesses, crystal volume, and the end-cap to crystal position [14,19]. It is also important to take into account the photon attenuation that can occur in the source housing materials [19]. This presently is only a concern for the ^{241}Am source which is contained in a 1.9 mm thick aluminum container. Therefore in the model it is assumed that this source is located in the middle of the container attenuated by 0.95 mm of aluminum.

For photon transport simulations, MCNP is run in p mode (photon transport), and the efficiencies are acquired from the F8 pulse height tally. The F8 tally for photons in MCNP records the number of pulses detected in user specified energy bins, which is analogous to a detector response function. The statistical uncertainties in the MCNP photon transport simulation were kept to less than 1%. Using the specifications for the detector given on the quality assurance (QA) data sheet (Table 2) the differences between the experimental and simulated efficiencies were found to range from 8% to 22%. The ratios are shown in the 'Manufacturer specified' column in Table 3. Given that all simulated efficiencies are greater than measured, it was thought that this may indicate that the active detector volume may actually be less than specified, and the crystal may be deeper with respect to the end-cap [14] than quoted. The quality assurance sheet states that the detector has a 0.5 mm Be window, but on close inspection this is not the case. The detec-

Table 2
Initial parameters from the detector QA data sheet used to model the HPGe detector in MCNP.

Parameter	Manufacturer specified
Crystal diameter	52 mm
Crystal length	20 mm
Internal dead-layer	0.9 mm ^a
External dead-layer	0.3 μm
End-cap to crystal	3 mm
Hole diameter	9 mm ^a
Hole depth	7.6 mm ^a
Window	0.5 mm (Be)

^a From private communication with ORTEC.

Table 3
Comparison of the experimental and simulated full-energy peak efficiencies (FEPE).

Energy (keV)	MCNP to experimental efficiency ratios	
	Manufacturer specified ^a	Adjusted parameters ^b
59.54	1.14	1.01
86.55	1.12	1.02
105.31	1.08	0.99
344.28	1.15	1.08
411.12	1.16	1.08
661.66	1.18	1.11
1004.73	1.24	1.17

^a Detector modeled using the geometric parameters listed in Table 2.

^b Detector modeled with the germanium crystal 2 mm deeper from a 1.3 mm Al window.

tor face is entirely aluminum, with a thickness of 1.3 mm. It was subsequently determined through communication with ORTEC that this was a special order detector. The presence of this aluminum window not only attenuates the low energy γ -rays, but it places all the sources a distance of 0.8 mm further than initially modeled.

To investigate the efficiency discrepancies further, multiple scans of the detector length and radius were performed [14,20]. The detector was placed on a linear adjustable stand allowing the detector to be moved in 1 mm increments. The detector was then scanned with a 1 mm diameter lead collimated 88 keV γ -ray beam from a ^{109}Cd source. The thickness of the lead in the collimator was 25 mm. The 88 keV peak counting rate was measured as a function of detector position. The front detector radius and normalized side scans are shown in Fig. 3. The front scan confirmed the radius to be ~ 52 mm. The side scans show a large drop of about 80% in the counting rate over the crystal length at a distance of about 9 mm from the detector face. This drop occurs for a distance of ~ 6 mm and then the counting rate appears to increase again. Initially it was thought that this may be the source of discrepancy between the results, and that perhaps this represented damaged areas of the crystal. However, upon the acquisition of a radiograph of the detector capsule, there appears to be some sort of clamping material holding the crystal in place. Therefore no firm conclusion can be made as to the active length of the crystal.

The scan results show the germanium crystal to be about 2 mm further back from the aluminum window than expected, and the X-ray images support this conclusion. Using these modifications and substituting the detector window with aluminum in the model the final ratios shown in the 'Adjusted parameters' column of Table 3 were obtained. The experimental and simulated efficiencies in Fig. 2 above, demonstrate that the detector response has been modeled sufficiently well over the energy region of 59.5 to ~ 200 keV. The discrepancies at the higher energies suggest that the active length may be shorter; as well the inner dead-layer thickness may be greater than the nominal value.

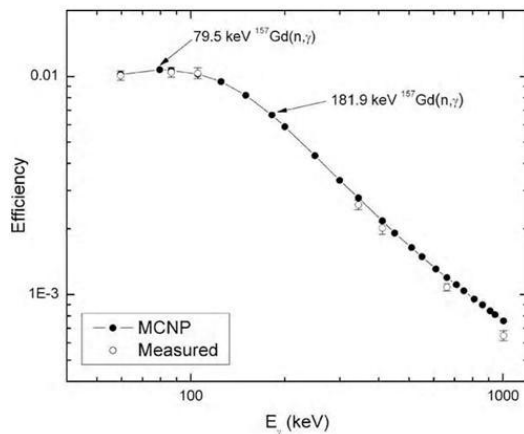


Fig. 2. Comparison of the measured and simulated absolute FEPEs against energy. The Monte Carlo data points correspond to the final adjusted parameters discussed below in the text.

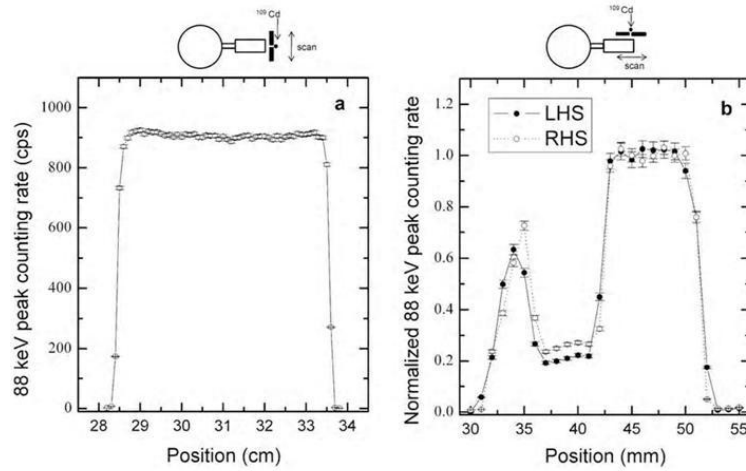


Fig. 3. Detector scans of (a) the 52 mm active diameter, and (b) along both sides of the 20 mm active length.

4. Neutron capture simulation

The next step in modeling of the experimental measurements is to simulate the neutron capture of gadolinium in our phantoms. The MCNP geometry input file of the $^{238}\text{Pu}/\text{Be}$ site which has been used to simulate the detection of cadmium and mercury [21] was kindly supplied by J. Atanackovic. The file is adapted to replicate the experimental geometries used in the gadolinium neutron capture [2]. This includes the detector model, leg phantoms, and the kidney and liver phantoms placed in the torso phantom. The initial objective was to transport neutrons and photons in the same simulation, and then to use the F8 pulse height tally to simulate the detector spectrum. This would include the gadolinium peaks as well as the background created from the activated shielding materials and the hydrogenous phantoms. This is hindered by the absence of neutron interaction data with germanium in MCNP5 [11], and the long computation time needed in n p mode (neutron and photon transport). To overcome these limitations, MCNP is run in n mode and p mode separately, and the results are combined to produce the simulated sensitivity (counts/ppm) of gadolinium. (It should be noted that germanium neutron data libraries are available in the updated revised release of evaluated data [22].)

To treat the slowing down (thermalization) of neutrons properly, MCNP provides thermal $S(\alpha, \beta)$ cross section libraries. Enger et al. [23] compared fluence measurements with MCNP simulations, and only found agreement when $S(\alpha, \beta)$ tables are used. Therefore the $S(\alpha, \beta)$ tables at a temperature of 294 K are used in the neutron transport simulations to describe the thermalization of neutrons accurately in beryllium, water, graphite, and polyethylene used in the experimental set-up.

To simulate the experiment with an acceptable amount of accuracy the neutron sources are modeled as uniform cylindrical volume sources with diameter of 2.06 cm and a length of 3.30 cm. The $^{238}\text{Pu}/\text{Be}$ source card is modeled after the spectrum described in Ref. [12]. The source activity is corrected for decay effects as well as for the source certification yield of $(2.4 \pm 3\%) \times 10^6$ n/s/Ci. The Be pre-moderator discs are housed in aluminum to protect from the toxic Be metal. This model includes the aluminum housing material of the Be pre-moderators. MCNP is run in n mode to transport neutrons to determine the number of (n, γ) reactions that occur in ^{157}Gd in the phantom cell volume (V). The FM4 tally multiplier card is used for this purpose and the resulting equation for the neutron capture by ^{157}Gd per neutron emitted from the source is:

$$P(n, \gamma) = C \int \int \varphi(\vec{r}, E) \sigma(E) dE dV \quad (1)$$

Eq. (1) includes the number density, C , of ^{157}Gd in the phantom cell volume, the neutron fluence spectrum, $\varphi(\vec{r}, E)$ and the energy dependant (n, γ) cross section for ^{157}Gd , $\sigma(E)$.

The second part of the model transports photons from the phantom through the surrounding media to the detector. A separate input file is created to transport photons in p mode to determine the efficiency of a uniform volume source of characteristic photons incident on the germanium detector. The F8 pulse height tally is used for this purpose, and the resultant equation for the gadolinium peak counts for a prompt γ -ray at energy E_γ , acquired by the detector is:

$$R(E_\gamma) = nP(n, \gamma) \Gamma(E_\gamma) \bar{\epsilon}(\vec{r}, E_\gamma) \quad (2)$$

Eq. (2) now includes the number of neutrons, n , emitted from the source for 2000 s, the γ -ray emission probability per neutron capture (derived from Ref. [24]), $\Gamma(E_\gamma)$, and the volume averaged peak efficiency, $\bar{\epsilon}(\vec{r}, E_\gamma)$, of the prompt γ -rays from the phantom volume source. The volume averaged peak efficiency is simulated in MCNP by sampling the source position from a uniform volume source of photons of energy, E_γ , and then tracking their energy deposition within the detector active volume. Since the F8 tally output is normalized by the number of photons emitted, the volume averaged peak efficiency is determined by summing the number of the full-energy detection events from the tally output.

The smaller 125 mL kidney phantoms are modeled as a single cylindrical volume, since they can be placed entirely in the collimated neutron beam. The liver and leg phantoms are much larger than the collimator and therefore it was decided that separating them into three volumes vertically would be sufficient to match with the experimental data. The center cylinder is modeled to the extent of the neutron beam diameter, and the top and bottom cylindrical sections are of equal volumes completing the 2 L phantoms. The relative errors in all FM4 tally outputs are less than 3.6%. The Monte Carlo calculations in this work are not normalized to the experiment and are based solely on an *ab initio* computation. In Fig. 4, a demonstration of the close agreement of the MCNP model with the experimental data is shown in the calibration line (182 keV peak area versus concentration) for a kidney phantom placed at 4 cm dorsal and lateral depths in the torso phantom.

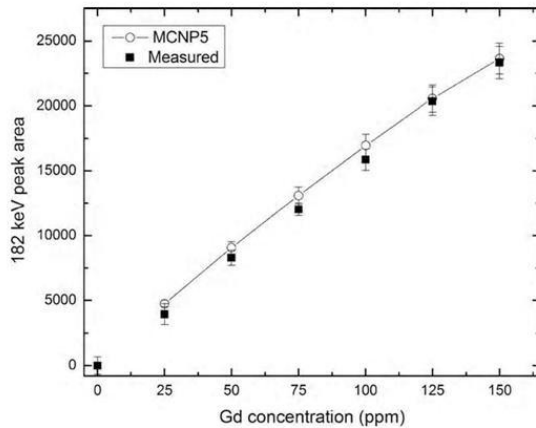


Fig. 4. Simulated and measured 182 keV calibration lines for the kidney at 4 cm lateral and dorsal depths. Dorsal and lateral depths represent the skin to organ distance.

The results show that even when neglecting the spatial distribution of the neutron capture (i.e., photon production) within the kidney phantoms for the photon transport model, the agreement is still sufficient to match with the measured 182 keV peak areas. The above result can be adapted for the other characteristic emissions, but in terms of making predictions and improvements, simulation of the dominant 182 keV line is sufficient for these purposes.

5. MCNP predictions

The appearance of fluence depression (FD) and self-shielding (SS) phenomena seen in cadmium kidney phantoms [21], motivates the investigation of the same phenomena in the gadolinium phantoms. As shown in Fig. 5, there is a large deviation from linearity of the ^{157}Gd neutron capture rate in the kidney phantoms as the concentration of gadolinium increases. This is reasonable considering the enormous thermal neutron capture cross section of

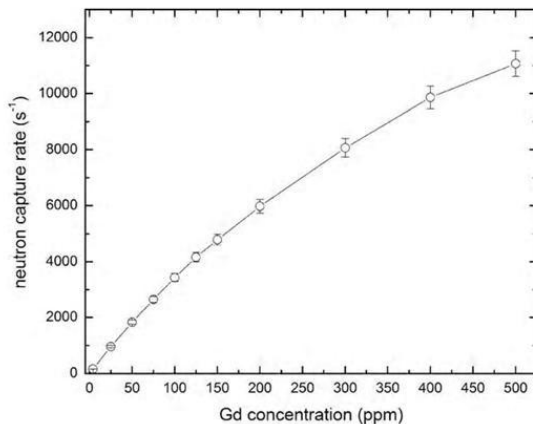


Fig. 5. Simulated ^{157}Gd neutron capture rate as a function of Gd concentration in the kidney phantoms. Note the non-linearity due to self-shielding and fluence depression.

^{157}Gd . Furthermore the large cross section of ^{155}Gd ($a = 14.8\%$, $\sigma_0 = 60\,900\text{ b}$) [10] is expected to suppress neutron capture at higher concentrations. The percentage difference between the extrapolation of a linear line between 0 and 4 ppm Gd concentrations, increases to above 6% around 50 ppm in the 125 mL kidney phantoms, and around 25 ppm in the 2 L liver and leg phantoms. This result is subtly shown for the concentrations presented in Fig. 4. These attenuation effects are more significant at concentrations higher than expected for *in vivo* measurements.

In order to soften the broad neutron energy spectrum (0–11 MeV [12]) of the $^{238}\text{Pu}/\text{Be}$ source and improve the feasibility of *in vivo* measurement (dose constraints; higher energy neutrons are more biologically damaging [25]), a neutron pre-moderator consisting of 2 cm and 4 cm beryllium discs is placed between the source and the subject [26]. An investigation into the effectiveness of these pre-moderators in terms of measurement sensitivity was modeled for the 25 ppm 2 L leg phantoms. As shown in Fig. 6, the ^{157}Gd γ -ray production rate increases with decreasing beryllium thickness. This result is consistent with the investigation by Franklin et al. [26], which demonstrated an increase in the thermal neutron fluence inside a water phantom with decreasing beryllium thickness. Also, if the leg phantoms are encased in a graphite reflector the improvement is quite significant. The graphite geometry is depicted in Fig. 7; graphite completely surrounds the leg phantoms except for a space large enough to place the HPGe detector.

To investigate the validity of the MCNP predictions further, the leg phantoms were irradiated with only 2 cm of the Be pre-moderator placed into the collimator. A comparison plot is shown in Fig. 8, which demonstrates both the measured and simulated calibration curves for the 2 and 6 cm pre-moderator configuration. The agreement here provides a further validation to the model. This also suggests that the model will be useful for the optimization of the moderation of the neutron energy spectrum of the $^{238}\text{Pu}/\text{Be}$ source. This is of importance for both sensitivity and dosimetric purposes. In fact, it was determined by Atanackovic et al. [21] that the higher energy neutrons ($>10\text{ keV}$) in the organs at risk from the $^{238}\text{Pu}/\text{Be}$ source were the largest contributor to the dose rates, despite the fact that they were the smallest component of the neutron fluence within these organs. Therefore MCNP can now be used to model different fast neutron moderating and filtering materials so as to reduce the fast neutron component of the neutron beam and optimize the lower energy component.

The range of percentage deviations between MCNP and the experiment, for the data presented in Figs. 4 and 8, was 1% and

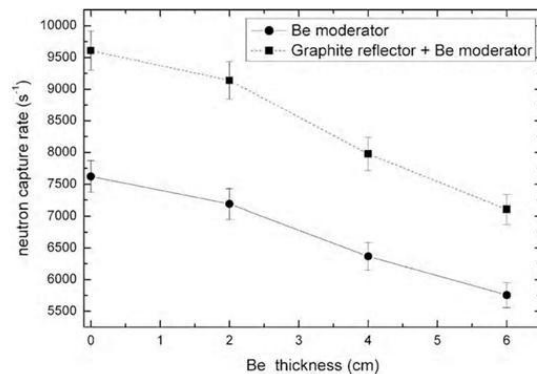


Fig. 6. Simulated ^{157}Gd neutron capture rate in the 25 ppm 2 L leg phantoms as a function of pre-moderator thickness. The improvements gained from encasing the phantoms in graphite are shown as well.

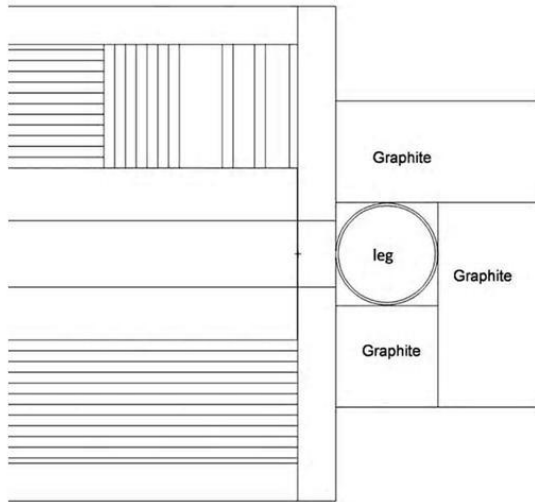


Fig. 7. MCNP geometry for the leg phantom encased in graphite to reflect the escaping neutrons back into the phantom.

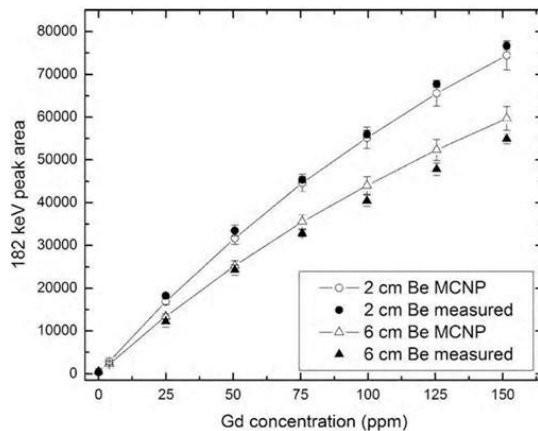


Fig. 8. Comparison plot of the measured and simulated 182 keV peak areas for the 2 and 6 cm Be pre-moderator configuration for the 2 L phantoms. Note the presence of self-shielding and fluence depression in both the measured and simulated peak areas.

18% (for the kidney at 25 ppm Gd, this was the only percentage deviation greater than 10%). The average deviation was $3.8 \pm 6.7\%$. These simulations show that for this irradiation/detection geometry, these phantom sizes and photon emission energies, that it is not necessary to consider the spatial distribution of the photon production (from neutron capture events) within the phantom cell volume for the photon transport model (a uniform volume distribution is sufficient). However, it is shown in Figs. 4, 5 and 8, that in the neutron capture simulation it is important to consider the self-attenuation effects due to the enormous cross sections of ^{155}Gd and ^{157}Gd . This model will be useful for future work by developing patient specific calibration lines depending on organ size and location within the body. Furthermore, Monte Carlo dosimetric studies will be performed to investigate the potential for any significant dose enhancement from ^{157}Gd due to the de-excitation of $^{158}\text{Gd}^*$ emitting prompt γ -rays, conversion electrons and Auger electrons [27], therefore examining the feasibility of this measurement procedure in its entirety.

tion of $^{158}\text{Gd}^*$ emitting prompt γ -rays, conversion electrons and Auger electrons [27], therefore examining the feasibility of this measurement procedure in its entirety.

6. Conclusions

The measured gadolinium sensitivities have been confirmed with the use of two MCNP models. The two models describe the production and the detection of the most dominant prompt γ -rays following gadolinium neutron capture in an *in vivo* measurement system. The neutron transport model can now be used to optimize the detection sensitivity per unit dose and improve the feasibility of *in vivo* measurement. The MCNP model will help to develop this method further for non-invasively determining the amount of Gd deposited in patients following Gd-based contrast enhanced MRI by prompt gamma neutron activation analysis.

References

- [1] F.G. Shellock, E. Kanal, Safety of magnetic resonance imaging contrast agents, *J. Magn. Reson. Imaging* 10 (1999) 477–484.
- [2] J.L. Gräfe, F.E. McNeill, S.H. Byun, D.R. Chettle, M.D. Noseworthy, The feasibility of *in vivo* detection of gadolinium by prompt gamma neutron activation analysis following gadolinium based contrast enhanced MRI, *Appl. Radiat. Isot.*, submitted for publication.
- [3] R.P. Fedorowicz, D.R. Chettle, T.J. Kennett, W.V. Prestwich, C.E. Webber, A $^{238}\text{Pu}/\text{Be}$ facility for *in vivo* cadmium measurements, in: K.J. Ellis, J.D. Eastman (Eds.), *Human Body Composition*, Plenum Press, New York, 1993.
- [4] J. Grinyer, S.H. Byun, D.R. Chettle, *In vivo* prompt gamma neutron activation analysis of cadmium in the kidney and liver, *Appl. Radiat. Isot.* 63 (2005) 475–479.
- [5] H. Gries, Extracellular MRI contrast agents based on gadolinium, *Top. Curr. Chem.* 221 (2002) 1–24.
- [6] H.J. Weinmann, M. Laniado, W. Mützel, Pharmacokinetics of GdDTPA/dimeglumine after intravenous injection into healthy volunteers, *Physiol. Chem. Phys. Med. NMR* 16 (1984) 167–172.
- [7] M.E. Bartolini, J. Pekar, D.R. Chettle, F. McNeill, A. Scott, J. Sykes, F.S. Prato, G.R. Moran, An investigation of the toxicity of gadolinium based MRI contrast agents using neutron activation analysis, *Magn. Reson. Imaging* 21 (2003) 541–544.
- [8] G.W. White, W.A. Gibby, M.F. Tweedle, Comparison of Gd(DTPA-BMA) (Omniscan) versus Gd(HP-DO3A) (Prohance) relative to gadolinium retention in human bone tissue by inductively coupled plasma mass spectroscopy, *Invest. Radiol.* 41 (2006) 272–278.
- [9] W.A. High, R.A. Ayers, S.E. Cowper, Gadolinium is quantifiable within the tissue of patients with nephrogenic systemic fibrosis, *J. Am. Acad. Dermatol.* 56 (2007) 710–712.
- [10] S.F. Mughabghab, *Neutron Cross Sections*, vol. 1, Part B, Z = 61–100, Academic Press, New York, 1984.
- [11] X-5 Monte Carlo Team, MCNP – A General Monte Carlo N-particle Transport Code Manual, Version 5, LA-UR-03-1987, Los Alamos National Laboratory, 2003.
- [12] S. Block, J. Bryan, C. Prevo, D. Montan, Laboratory sources enhanced in 0.5 eV to 200 keV neutrons for instrument evaluation, *Health Phys.* 13 (1967) 1025–1031.
- [13] International Atomic Energy Agency, X-ray and Gamma-ray Decay Data Standards for Detector Calibration and Other Applications; <http://www-nds.iaea.org/xgamma_standards/>.
- [14] R.G. Helmer, J.C. Hardy, V.E. Jacob, M. Sanchez-Vega, R.G. Neilson, J. Nelson, The use of Monte Carlo calculations in the determination of a Ge detector efficiency curve, *Nucl. Instrum. Methods A* 511 (2003) 360–381.
- [15] D.V. Booker, The divergence from Gaussian of peak shapes in gamma-ray spectra observed with germanium detectors, *J. Radioanal. Chem.* 48 (1979) 83–90.
- [16] I.O.B. Ewa, D. Bodizs, Sz. Czifrus, Zs. Molnar, Monte Carlo determination of full energy peak efficiency for a HPGe detector, *Appl. Radiat. Isot.* 55 (2001) 103–108.
- [17] J. Ródenas, A. Pascual, I. Zarza, V. Serradell, J. Ortiz, L. Ballesteros, Analysis of the influence of germanium dead layer on detector calibration simulation for environmental radioactive samples using the Monte Carlo method, *Nucl. Instrum. Methods A* 496 (2003) 390–399.
- [18] C.M. Salgado, C.C. Conti, P.H.B. Becker, Determination of HPGe detector response using MCNP5 for 20–150 keV X-rays, *Appl. Radiat. Isot.* 64 (2006) 700–705.
- [19] K. Debertin, R.G. Helmer, *Gamma- and X-ray Spectrometry with Semiconductor Detectors*, North-Holland, Amsterdam, 1988.
- [20] K. Debertin, B. Grosswendt, Efficiency calibration of semiconductor detectors by primary standard sources and Monte Carlo calculations, *Nucl. Instrum. Methods* 203 (1982) 343–352.

- [21] J. Atanackovic, J. Grinyer, D.R. Chettle, S.H. Byun, The comparison of two MCNP models used for prompt gamma in vivo detection of cadmium and mercury, Nucl. Instr. and Meth. B 263 (2007) 169–174.
- [22] M.B. Chadwick et al., ENDF/B-VII.0: next generation evaluated nuclear data library for nuclear science and technology, Nucl. Data Sheets 107 (2006) 2931–3060.
- [23] S.A. Enger, P.M. af Rosenschöld, A. Rezaei, H. Lundqvist, Monte Carlo calculations of thermal neutron capture in gadolinium: a comparison of GEANT4 and MCNP with measurements, Med. Phys. 33 (2006) 337–341.
- [24] Database of prompt gamma rays from slow neutron capture for elemental analysis, International Atomic Energy Agency (IAEA), Vienna, 2006.
- [25] ICRP P103, The 2007 Recommendations of the International Commission on Radiological Protection, Chapters 3 and 4, Ann. ICRP 37, 2007, pp. 49–79.
- [26] D.M. Franklin, R. Armstrong, D.R. Chettle, C. Scott, An improved in vivo neutron activation system for measuring kidney cadmium, Phys. Med. Biol. 35 (1990) 1397–1408.
- [27] T. Goorley, H. Nikjoo, Electron and photon spectra for three gadolinium-based cancer therapy approaches, Radiat. Res. Soc. 154 (2000) 556–563.

3.3 Additional Material

The model can be used to characterize the collimating and shielding properties of the $^{238}\text{Pu}/\text{Be}$ isotopic irradiation system. Two examples are shown here. To determine the effectiveness of the beam collimation, the beam profile was computed at a distance of 5 cm from the front face of the collimating and shielding apparatus. The beam profile is shown in Figure 3.1. The beam Full Width at Half Maximum (FWHM) is 13 cm. This demonstrates that even though the inner steel tube collimator has a physical dimension of 9 cm in diameter the collimated neutron beam is actually larger. The beam width at 80% of the maximum is, however, comparable to the physical collimator dimensions at 10.3 cm.

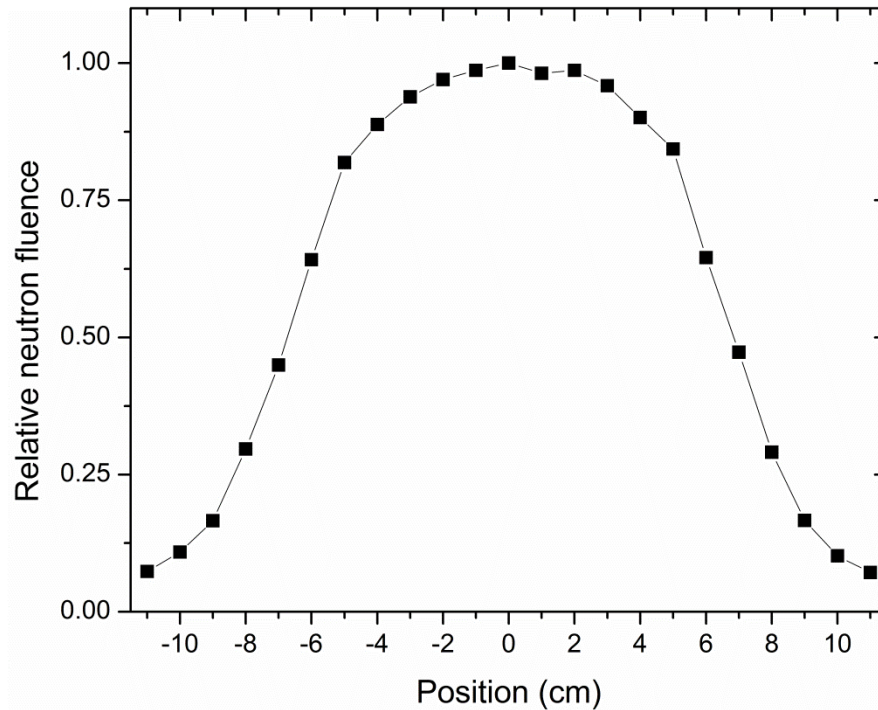


Figure 3.1. Simulated neutron beam profile 5 cm away from the shielding and collimating apparatus.

The neutron fluence rate profile in water is shown in Figure 3.2 for thermal neutrons (< 0.1 eV), epithermal and resonance neutrons (0.1 eV – 1 keV), intermediate neutrons (1 keV – 1 MeV), and fast neutrons (>1 MeV). The total neutron fluence rate peaks at approximately 1.5 cm in water and the thermal neutron fluence rate peaks at approximately 3 cm in water. These are just some examples of the applications of the model that could be used to characterize the system as well as investigate different system optimizations.

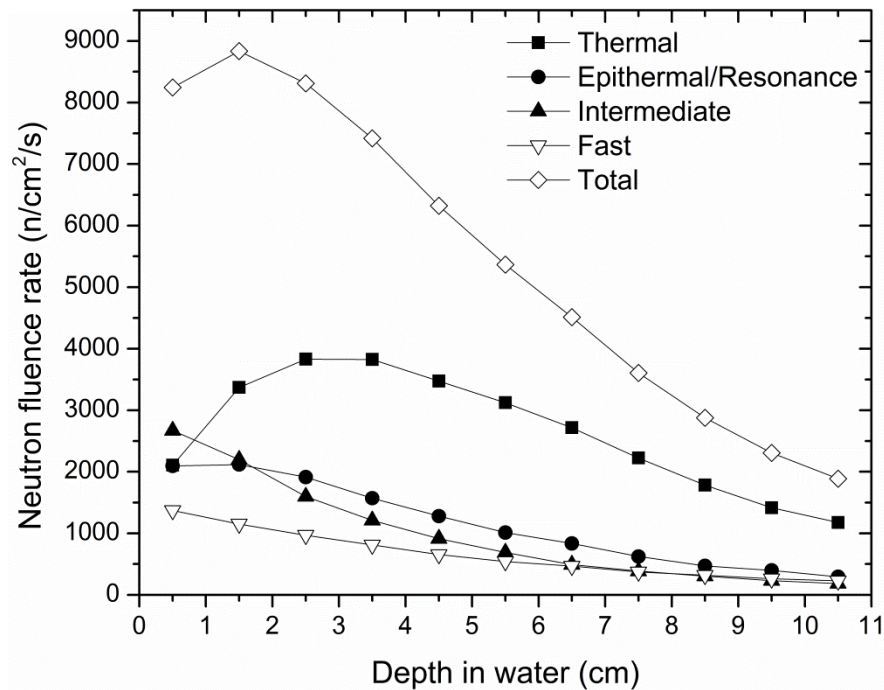


Figure 3.2. Neutron fluence rate profile as a function of depth in water for the $^{238}\text{Pu}/\text{Be}$ system.

Chapter 4

Characteristic X ray emission in gadolinium following neutron capture as an improved method of *in vivo* measurement: a comparison between feasibility experiment and Monte Carlo simulation (Article III)

4.1 Introduction to Article III

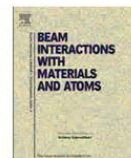
This paper is an extension of my previously described Monte Carlo work on the detection of Gd to include the characteristic K X ray emissions that occur due to internal conversion de-excitations following neutron capture. Initially in the prompt gamma ray experiments on Gd we were only looking for the most dominant neutron capture prompt gamma rays, but a subsequent analysis of the spectra identified a significant number of characteristic Gd K X rays. It can be calculated from the available nuclear data, the probability of a K X ray emission due to internal conversion electron emission (a competing process to gamma ray emission) resulting from neutron capture on natural Gd is actually more probable than the most dominant prompt gamma ray from the ^{157}Gd isotope. This is partly due to the fact that another isotope, ^{155}Gd , which contributes about 19% to the neutron capture in natural Gd, also has a high probability for internal conversion and subsequent X ray emission. The observation of significant numbers of Gd X rays in the experimental spectra is a further validation to the model and provides confidence in the available nuclear data on gadolinium.

The experimental and simulation work in Article III was performed by the author of this thesis under the supervision of Dr. Fiona McNeill and under the guidance of Dr. David Chettle and Dr. Soo Hyun Byun. Drs. McNeill and Chettle assisted in the analysis of the comparison of measurement to simulation, and Dr. Chettle also assisted in

optimizing the peak fitting functions. The manuscript was prepared by the author of this thesis and edited by Drs. Fiona McNeill, David Chettle, and Soo Hyun Byun.

4.2 Contents of Article III

The following article is reproduced with permission. Copyright © 2012, Elsevier.



Characteristic X ray emission in gadolinium following neutron capture as an improved method of *in vivo* measurement: A comparison between feasibility experiment and Monte–Carlo simulation

J.L. Gräfe*, F.E. McNeill, D.R. Chettle, S.H. Byun

Department of Medical Physics and Applied Radiation Sciences, McMaster University, Hamilton, Ontario, Canada L8S 4K1

ARTICLE INFO

Article history:

Received 25 January 2012

Received in revised form 16 March 2012

Available online 29 March 2012

Keywords:

In vivo neutron activation analysis

Gadolinium

Monte–Carlo simulation

Internal conversion

Characteristic K X rays

ABSTRACT

We have extended our previous experimental and Monte–Carlo work on the detection of Gd by *in vivo* prompt gamma neutron activation analysis to include X ray emission. In this paper we incorporate the characteristic K X ray emission that occurs due to internal conversion from the de-excitation of the $^{156}\text{Gd}(n,\gamma)^{156}\text{Gd}^*$ and $^{157}\text{Gd}(n,\gamma)^{157}\text{Gd}^*$ reactions. The experimental Gd K X ray intensities are compared with the Monte–Carlo model and demonstrate excellent agreement. The experiment was consistently higher than simulation by 5%. For the detection system used, the Gd K_α X rays are about 1.5 times as intense as the most dominant prompt gamma ray from the $^{157}\text{Gd}(n,\gamma)$ reaction. The partial elemental cross section for K_α X ray emission is ~1.35 times larger than that of the most dominant prompt gamma ray from neutron capture of ^{157}Gd alone. The use of the K X rays was found to improve the sensitivity of the proposed system to measure Gd retention after exposure to a Gd-based MRI contrast agent. The detection limit in phantoms was ~30% better when the X ray signal was incorporated into the analysis method, reducing the detection limit from 0.89 to 0.64 ppm Gd.

© 2012 Elsevier B.V. All rights reserved.

1. Introduction

Gadolinium (Gd) is an element possessing unique properties. It is a strongly paramagnetic element that is routinely used in chelated form as an MRI contrast agent. It also possesses the largest thermal neutron cross section of all the stable elements. In our work, we have been developing a method to detect Gd *in vivo* by prompt gamma neutron activation analysis (PGNAA) after Gd contrast agent injection to investigate Gd retention and toxicity [1]. With a total neutron absorption cross section of nearly 48,800b, Gd is a well suited candidate for detection by PGNAA. The ^{155}Gd and ^{157}Gd isotopes, with natural abundances of 14.8% and 15.65%, respectively, contribute most significantly to the thermal neutron absorption cross section, representing nearly 99.99% of the elemental cross section. The ^{155}Gd isotope has a thermal neutron absorption cross section of 60,900b, while the ^{157}Gd isotope has the largest thermal neutron absorption cross section of all the stable isotopes at 254,000b [2].

We have previously described the feasibility and methodology of this technique using the prompt gamma rays from neutron activation of the ^{157}Gd isotope [1]. We have also developed an *ab initio* benchmarked Monte–Carlo model of the system demonstrating

excellent agreement [3]. In this paper, we present our experimental and Monte–Carlo simulation work looking at the characteristic K X ray emission following neutron capture on Gd. After neutron capture the first and second excited states of the resultant $^{156}\text{Gd}^*$ and $^{157}\text{Gd}^*$ nuclei are relatively low lying in energy. These low lying excited states combined with a relatively high atomic number for Gd ($Z = 64$) leads to a high probability for internal conversion electron emission, which is a competing process to gamma ray emission. With the internal conversion electron emission leaving vacancies in the atomic shells, orbital electron shuffling occurs leading to the emission of characteristic X rays from Gd. Therefore, neutron activation of natural Gd leads to the production of elemental characteristic atomic X rays as well as the isotope specific prompt gamma rays. We demonstrate here that the X ray signal can significantly improve the sensitivity of the *in vivo* Gd measurement system which has been proposed for retention studies investigating the safety of Gd-based MRI contrast agents.

2. Methods

Aqueous 2 L Gd phantoms ranging in concentration between 0 and 151 ppm were developed in our earlier work to simulate both the human liver and lower leg muscle [1]. In this lower leg phantom study, lower concentration phantoms of Gd concentration 0, 2, 5, 10, and 25 ppm Gd phantoms were measured a total of 10

* Corresponding author. Tel.: +1 289 244 3238; fax: +1 905 522 5982.
E-mail address: grafejl@mcmaster.ca (J.L. Gräfe).

times, and higher concentration phantoms, of concentration 50, 75, 100, 125, and 150 ppm Gd were measured three times each. The phantom spectra were acquired using a LO-AX model HPGe detector (10% relative efficiency, ORTEX 51700/20-S), which we have modeled using the Monte-Carlo code MCNP5 [3]. The acquisition time was for a fixed 2000 s live time (the detection system dead time was less than 3.7% for all measurements). This time has been chosen as optimal for both detection limits and participant comfort. The entire phantom measurement procedure has been previously described in Ref. [1].

2.1. Spectral analysis

The Gd characteristic K X ray energies and relative intensities are shown in Table 1 [4]. A typical spectrum in the Gd K X ray region for a 151 ppm phantom is shown in Fig. 1.

The K_α lines are very close in energy, with a separation of only ~ 0.7 keV, which is comparable to the detector's energy resolution in this region (~ 0.95 keV) and therefore these peaks are not well resolved. The K_α lines do not quite merge to form a perfect Gaussian, and therefore a double Gaussian function is used to fit this peak feature. There is also a noticeable step in the background which increases with Gd concentration. Therefore the K_α peaks were fitted with the following function:

$$y = mx + B + f_1 A \left[\exp \left(-\frac{1}{2} \left(\frac{x - x_c}{\sigma} \right)^2 \right) + S_A \sigma \sqrt{2\pi} \operatorname{erfc} \left(\frac{x - x_c}{\sigma} \right) \right] + f_2 A \left[\exp \left(-\frac{1}{2} \left(\frac{x - x_c + s}{\sigma} \right)^2 \right) + S_A \sigma \sqrt{2\pi} \operatorname{erfc} \left(\frac{x - x_c + s}{\sigma} \right) \right] \quad (1)$$

where m is the slope of the linear background, B the intercept of the linear background, f_i are the normalized X ray intensities (i.e., $f_1 = 1$ and $f_2 = 0.556$ for the $K_{\alpha 1}$ and $K_{\alpha 2}$ peaks, respectively), A is the peak amplitude, x_c is the peak centroid, σ is the peak width (standard deviation), S_A is the step amplitude fraction of the peak amplitude, and s is the number of channels between the two X ray peaks (determined from the gain settings and energy calibration). The step amplitude is a property of the detector and incident photon energy and is mainly a result of electrons escaping the detector active volume, reducing the charge collection. Therefore, the step function in this case, is a fixed proportion of the peak amplitude determined from fitting the 53.53 keV prompt gamma ray from the $^{72}\text{Ge}(n, \gamma)$ reaction in the Ge detector volume [5]. This gamma ray is close enough in energy to the Gd K X rays to provide an estimate of the background step. To maintain the stability of the fits for the low concentration phantoms, the peak width and centroid were determined from the high concentration phantoms with high numbers of counts in the peaks, and subsequently were fixed in the fitting procedure.

The $K'_{\beta 1}$ peaks are close enough in energy to be merged into a single Gaussian, while the $K'_{\beta 2}$ is separated from these peaks by

Table 1
Gd K X ray energies and relative intensities.

Line	Energy	Relative intensity
$K_{\alpha 2}$	42.309	0.556
$K_{\alpha 1}$	42.996	1
$K'_{\beta 1}$	48.7	0.292
$K'_{\beta 2}$	50	0.0899

Relative intensities from Ref. [4].

$K'_{\beta 1} = K_{\beta 1} + K_{\beta 3} + K_{\beta 5}$.

$K'_{\beta 2} = K_{\beta 2} + K_{\beta 4}$.

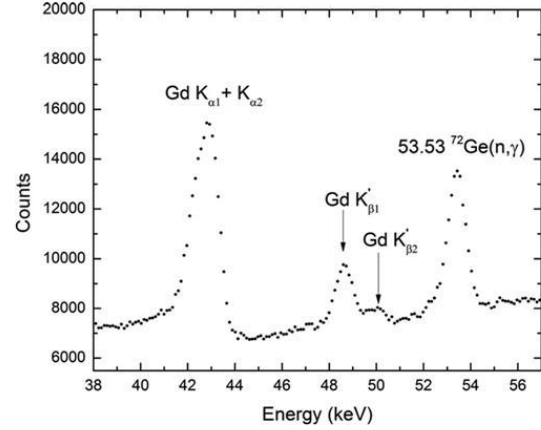


Fig. 1. A representative spectrum in the Gd K X ray region for a 151 ppm 2 L Gd phantom.

more than 1.3 keV (i.e., greater than the energy resolution of the detector). Therefore, the $K'_{\beta 1}$ peaks are fitted with a single Gaussian and a second Gaussian is used to fit the $K'_{\beta 2}$ peak. The K_β X rays were also fitted with Eq. (1). The values of f_1 and f_2 are 0.308 and 1 for the $K'_{\beta 2}$ and $K'_{\beta 1}$ peaks, respectively. The f_i values in this case are normalized with respect to the combined $K'_{\beta 1}$ line (see Table 1), and thus the K_β amplitudes are not constrained by the result obtained from the K_α .

2.2. MCNP simulation

We have developed a simple benchmarked simulation for the detection of the prompt gamma rays from Gd neutron capture [3]. We have done this in a binary fashion. Firstly, the number of neutron capture reactions with ^{157}Gd is determined by the MCNP5 code [6] in neutron mode. Secondly, a simulation of a volume source of the prompt gamma rays in photon mode is run to determine the detection efficiency. The simulation is easily modified, as shown below, to also incorporate the number of interactions with the ^{155}Gd isotope and to determine the detection efficiency of the characteristic K X rays.

The Gd neutron absorption cross section is dominated by the $^{155,157}\text{Gd}$ isotopes. The (n, γ) reactions with these isotopes subsequently leads to K X ray emission. The number of neutron captures per source neutron in either ^{155}Gd or ^{157}Gd from MCNP is:

$$N_i(n, \gamma) = C_i \iint \phi(\vec{r}, E) \sigma_i(E) dE dV \quad (2)$$

where the index i represents either ^{155}Gd and ^{157}Gd , C_i is the number density, $\phi(\vec{r}, E)$ is the neutron fluence spectrum, and $\sigma_i(E)$ is the energy dependent (n, γ) cross section.

The number of counts in the detector for the K X rays can then be determined by:

$$R(E_{X_K}) = n \bar{\epsilon}(\vec{r}, E_{X_K}) \sum_{i=1}^2 N_i(n, \gamma) p_i(X_K) \quad (3)$$

where n is the number of neutrons emitted from the source in 2000 s, $\bar{\epsilon}(\vec{r}, E_{X_K})$ is the volume averaged X ray peak efficiency, and $p_i(X_K)$ is the probability per neutron capture for either K_α or K_β X ray emission defined as:

Table 2Relevant nuclear data used to determine KX ray emission probability from neutron capture in the $^{155,157}\text{Gd}$ isotopes.

Isotope	γ ray energy (keV)	Energy level (excited state)	Multi-polarity	γ ray emission probability (%) ^a	α_{Kj}	
					Brlcc [7] ^b	Rösel et al. [8] ^c
^{155}Gd	88.970	88.968 (1st)	E2	20.9 \pm 3.1	1.559 \pm 0.022	1.54
	199.219	288.186 (2nd)	E2	31.6 \pm 1.9	0.1565 \pm 0.0022	0.156
^{157}Gd	79.5132	79.5128 (1st)	E2	9.75 \pm 0.69	2.02 \pm 0.03	2.00
	181.943	261.4568 (2nd)	E2	18.33 \pm 1.69	0.206 \pm 0.003	0.209

Nuclear data for ^{155}Gd and ^{157}Gd from Refs. [9,10].^a $p_{ij} \times 100\%$; percent per neutron capture.^b Values from “Frozen Orbital” approximation.^c Values are determined by linear interpolation (estimated uncertainties are less than 5%, with a mean of 2% by this method, see Ref. [8]).**Table 3**X ray emission probabilities expressed as the percent per neutron capture in $^{155,157}\text{Gd}$.

Isotope		$p_i(X_K) \times 100\%$	
		Current ^a	Stepanek ^b
^{155}Gd	K_{α}	29.1 \pm 3.8	–
	K_{β}	7.1 \pm 0.9	–
^{157}Gd	K_{α}	18.2 \pm 1	17.5
	K_{β}	4.5 \pm 0.3	4.27

^a Calculated using Brlcc [7], nuclear data sheets [9,10], and Ref. [4].^b From Ref. [11] using Dirac Chen’s extension method.

$$p_i(X_K) = P(K_{l,m})\omega_K \sum_{j=1}^2 p_{ij}\alpha_{Kj} \quad (4)$$

where $P(K_{l,m})$ is the probability for either K_{α} or K_{β} emission (i.e., the probability that a K shell vacancy will be filled by an electron from the L or M shell, respectively), ω_K is the K -shell fluorescence yield, p_{ij} is the gamma ray emission probability, and α_{Kj} is the K -shell internal conversion coefficient. The ω_K for Gd , $Z = 64$, is 0.966 [4]. The internal conversion coefficients are conveniently determined using the Brlcc v2.3S program available through the National Nuclear Data Centre [7]. For comparison they were also determined from the data of Rösel et al. [8]. The gamma ray emission probabilities are obtained from the Nuclear data sheets for $A = 156^*$ and $A = 158^*$ [9,10]. The internal conversion coefficients and nuclear data for the Gd isotopes considered are shown in Table 2. The summation in Eq. (4) is over the first and second excited states for both Gd isotopes. The summation can be extended to higher excited states but these states are populated less frequently, also the internal conversion coefficients decrease quite dramatically with transition energy. Therefore to a good approximation the total KX ray yield can be estimated from the first two excited states of ^{155}Gd and ^{157}Gd .

The K_{β}/K_{α} ratio for Gd is 0.245 [4], from this ratio, $P(K_{l,m})$ is 0.803 for K_{α} X rays, and 0.197 for the K_{β} X rays. Using these probabilities and the nuclear data from Table 2, the K_{α} and K_{β} X ray emission probabilities (in% per neutron capture) for $^{155,157}\text{Gd}$ are calculated and shown in Table 3. The values compiled here are compared with the data derived by Stepanek [11] for $^{158}\text{Gd}^*$ based on a more sophisticated computation. A strong agreement is noted based on using only the two most dominant transition levels in the calculation for $^{157}\text{Gd}(n,\gamma)^{158}\text{Gd}$. Unfortunately, no such comparison can be made for ^{155}Gd .

3. Results and discussion

The average reduced- χ^2 for the fits to the experimental K_{α} peaks was 1.2 ± 0.3 , and 0.9 ± 0.2 for the K_{β} peaks (\pm one standard deviation). This demonstrates that the peak fitting functions accurately fit the data. A representative example for the K_{α} and K_{β} peaks with resulting fits are shown in Fig. 2 for a 151 ppm phantom.

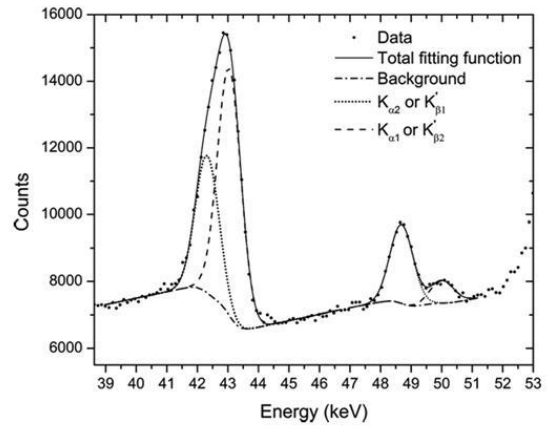


Fig. 2. A spectrum of the $\text{Gd } K_{\alpha}$ and K_{β} X ray peaks along with the fitting components for a 151 ppm Gd phantom. The individual Gaussian components include the background. Note that the K_{α} and K_{β} peaks were fitted separately.

A significantly non-zero intercept (i.e., different at a greater than 95% confidence level), 7.3 uncertainties different from zero was discovered when performing a least-squares linear fit on the K_{α} data from 0 to 25 ppm, a region where the self-shielding and fluence depression is less than 6% [3]. This offset is most likely to be from the germanium (Ge) KX ray escape peaks resulting from the 53.53 keV gamma ray from the $^{73\text{m}}\text{Ge}$ isomer (see Fig. 1) produced by the $^{72}\text{Ge}(n,\gamma)$ reaction in the Ge detector volume [5]. The $\text{Ge } KX$ ray escape peaks from the 53.53 keV gamma ray would be in the energy region of 42.4–43.7 keV (directly overlapping with the $\text{Gd } K_{\alpha}$ X ray energies). When the average peak area of 543 ± 108 counts (\pm average uncertainty divided by \sqrt{N}) from the zero concentration phantom is subtracted from the K_{α} peak areas the intercept is within 0.86 uncertainties of zero. Therefore, subtracting the average peak area that we attribute to a Ge escape peak signal removes the non-zero intercept in the calibration line for the K_{α} X rays, indicating no contamination of Gd in the phantoms or surrounding materials, and a well fitted background function.

The inverse variance weighted mean ratio of K_{β} to K_{α} peak areas was 0.262 ± 0.002 when comparing the peak areas from all the phantoms. The K_{β}/K_{α} ratio from the MCNP computation was 0.27 ± 0.02 . (The uncertainties in the MCNP values are from the uncertainty in the X ray line emission probability per neutron capture, the source certification yield (3%), and the statistical uncertainty from the neutron and photon simulation, which are less than 4% and on the order of 1%, respectively.) This latter simulation derived value is about 10% higher than the value of 0.245 from Ref. [4] due to the higher detection efficiency of the K_{β} X rays for this

experimental set-up (K_{β} X rays are attenuated less than the K_{α} on their path to the detector active volume). Given the changes in detection efficiency, the average experimental K_{β}/K_{α} ratio agrees well with the theoretical.

The simulated and average measured K_{α} and K_{β} peak areas are plotted in Fig. 3, and demonstrate relatively good agreement. The non-linearity of peak area versus concentration due to self-shielding and neutron fluence depression is evident as the Gd concentration increases. This demonstrates and confirms that the Gd K X rays are due to neutron capture reactions. Performing a linear fit on the plot of measured peak area against simulated yields a slope of 1.053 ± 0.006 for the K_{α} data, and 1.05 ± 0.01 for the K_{β} data. Both regressions yielded an r^2 value of 0.999. This suggests that there is a consistent offset between the model and experiment, with the experiment providing, on average, a K X ray signal that is 5% higher than MCNP. There are, of course, several potential reasons for the differences observed. For example, positioning of the detector and sample may not be perfectly matched, the position of the detector inside the canister may be marginally incorrect, the thickness of the detector canister could have a margin of error, the “dead” layer on the detector may not be perfectly known, the phantoms may not be perfectly positioned, and so on. There are so many potential sources of uncertainty that, in fact, we would argue that an agreement of 5%, without normalization, between the X ray signal derived from an *ab initio* combined neutron-photon simulation and experiment is very good.

The emission probabilities per neutron capture of the K_{α} X ray and the most intense gamma ray from neutron capture in ^{157}Gd are comparable at $18.2 \pm 1\%$ and $18.33 \pm 1.69\%$, respectively. The sensitivity (counts/ppm) of the K_{α} X ray peak is about 1.53 times more intense than the 181.9 keV prompt gamma ray. This is partly due to the nearly 1.15 times higher efficiency in the 43 keV region for this detection geometry, but more significantly the remaining factor of ~ 1.35 is due to neutron capture with the ^{155}Gd isotope which also produces characteristic X rays. This can be shown by calculating the partial elemental cross section, which is typically used for neutron capture gamma rays [12,13], but can be adapted for X ray emission as:

$$\sigma_X^Z(E_X) = \sum \theta_i p_i(X_K) \sigma_i(E_0) \quad (5)$$

where θ_i is the isotopic abundance, and $\sigma_i(E_0)$ is thermal neutron capture cross section for isotope, i .

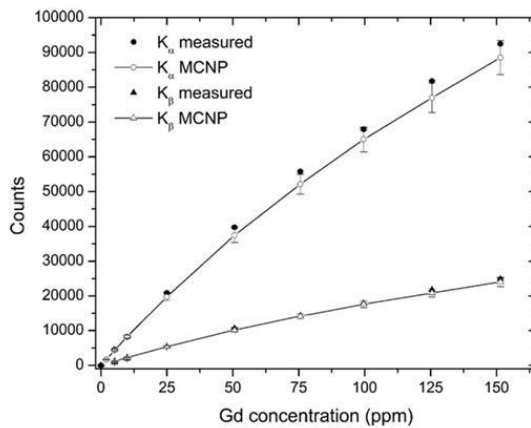


Fig. 3. Comparison plot of the simulated and average measured Gd K_{α} and K_{β} X ray peak areas.

The K_{α} X ray partial cross section is:

$$\sigma_X^Z(E_X) = (0.1565)(0.182)(254000b) + (0.148)(0.291)(60900b) = 9860b \quad (6)$$

This value is a factor of 1.35 times higher than the partial elemental cross section of $\sim 7300b$ for the 181.9 keV gamma ray from ^{157}Gd . Similarly the K_{β} partial cross section is $\sim 2400b$.

The leg muscle detection limit is 0.89 ppm [1] when using the 181.9 and 79.5 keV prompt gamma rays from neutron capture of ^{157}Gd . The detection limits from multiple emission lines are combined using the inverse variance weighting method to produce a final detection limit that is a reflection of the overall sensitivity of the system. When including the K_{α} X ray the final detection limit is reduced (improved) by a factor of ~ 1.4 to 0.64 ppm. This improvement is obtained from the exact same system under the same conditions of time and dose to a subject. Including the K_{β} X rays was found not to reduce the detection limit significantly. Therefore including the K_{α} X ray emission from Gd significantly improves the sensitivity of detecting Gd by a combination of prompt gamma ray and “prompt X ray” neutron activation analysis. In the future, the K X rays may also provide a depth correction for overlying tissue thickness due to the differential attenuation between the prompt gamma rays and the K X ray energies. This analysis could not be performed in these homogenous phantoms, but is an area of potential further work. The improvement in the detection limit from incorporation of the K X rays will occur to a varying degree for organs in which there is a significant amount of overlying tissue, such as the kidney and liver. This is because of the significantly higher attenuation of the X ray energies compared to the prompt gamma ray energies in tissue. Through Monte-Carlo simulation there is still a significant improvement of a factor greater than 1.15, when including the K X ray signal, to the kidney and liver detection limits for these organs with an overlying tissue thickness of 10 cm (the tissue thickness is defined as the distance from the skin surface to the center of the organ).

4. Conclusions

We have extended the *ab initio* Monte-Carlo model of our *in vivo* prompt gamma neutron activation analysis system to incorporate the characteristic X ray emission following neutron capture with Gd. The measurement of Gd by PGNA is now based on characteristic elemental X rays and isotopic prompt gamma rays. Excellent agreement between experiment and simulation has been demonstrated with an agreement, on average, of X ray signal per source neutron to within 5%. These results demonstrate the quality of some of the nuclear and atomic data available for Gd. The use of the Gd K X rays improves the detection limit of Gd by *in vivo* neutron activation analysis by a factor of ~ 1.4 .

References

- [1] J.L. Gräfe, F.E. McNeill, S.H. Byun, D.R. Chettle, M.D. Noseworthy, The feasibility of *in vivo* detection of gadolinium by prompt gamma neutron activation analysis following gadolinium-based contrast-enhanced MRI, *Appl. Radiat. Isot.* 69 (2011) 105–111.
- [2] S.F. Mughabghab, M. Divadeenam, N.E. Holden, *Neutron Cross Sections from Neutron Resonance Parameters and Thermal Cross Sections*, Academic Press, New York, 1981.
- [3] J.L. Gräfe, F.E. McNeill, S.H. Byun, D.R. Chettle, M.D. Noseworthy, A benchmarked MCNP model of the *in vivo* detection of gadolinium by prompt gamma neutron activation analysis, *Nucl. Instrum. Meth. Phys. B* 268 (2010) 2451–2457.
- [4] W.T. Elam, B.D. Ravel, J.R. Sieber, A new atomic database for X-ray spectroscopic calculations, *Radiat. Phys. Chem.* 63 (2002) 121–128.
- [5] R.L. Bunting, J.J. Kraushaar, Short-lived radioactivity induced in Ge(Li) gamma-ray detectors by neutrons, *Nucl. Instrum. Meth.* 118 (1974) 565–572.
- [6] X-5 Monte Carlo Team, MCNP – A General Monte Carlo N-particle transport code manual, Version 5, Los Alamos National Laboratory, 2003.

- [7] T. Kibédi, T.W. Burrows, M.B. Trzhaskovskaya, P.M. Davidson, C.W. Nestor Jr., Evaluation of theoretical conversion coefficients using Brlcc, Nucl. Instrum. Meth. Phys. A 589 (2008) 202–229.
- [8] F. Rösel, H.M. Fries, K. Alder, H.C. Pauli, Internal conversion coefficients for all atomic shells, At. Data Nucl. Data Tables 21 (1978) 91–289.
- [9] C.W. Reich, Nuclear Data Sheets for $A = 156$, Nucl. Data Sheets 99 (2003) 753–1030.
- [10] R.G. Helmer, Nuclear Data Sheets for $A = 158$, Nucl. Data Sheets 101 (2004) 325–519.
- [11] J. Stepanek, Emission spectra of Gadolinium-158, Med. Phys. 30 (2003) 41–43.
- [12] W.V. Prestwich, M.A. Islam, T.J. Kennett, A determination of the carbon thermal neutron capture cross section, Nucl. Sci. Eng. 78 (1981) 182–185.
- [13] Database of Prompt Gamma Rays from Slow Neutron Capture for Elemental Analysis, International Atomic Energy Agency (IAEA), Vienna, 2006.

4.3 Additional Material

With the creation of this well benchmarked model, the measurement sensitivity for Gd in the kidney and liver can now be conveniently determined for varying overlying tissue thicknesses. The Gd sensitivity (counts/ppm) in various target organ geometries is simulated and combined with the experimentally measured zero concentration background peak area error in each of the target organ positions. A total of 9 positions for the kidney and 6 positions for the liver were measured. The detector is moved for each measurement so that it is aligned with the centre of the phantom to optimize detection sensitivity. The work presented in this section combines the findings of Articles I, II, and III. The optimizations determined for the lower leg muscle in Article I are applied to the kidney and liver. These optimizations were namely the use of 2.5 cm of Pb detector shielding, and the increased slope determined from the 0-25 ppm phantoms (because of self-shielding and fluence depression at higher concentrations verified by simulation in Article II). The K X ray signal (Article III) is used here to improve the detection of Gd in the kidney and liver.

The experimental/Monte-Carlo geometrical set-up for the kidney irradiation for axial and lateral organ depths of 7 cm is shown in Figure 4.1. The axial depth is the depth from the torso phantom surface along the beam direction to the phantom center, and the lateral depth is from the phantom center to the torso phantom surface where the detector is positioned. This is demonstrated in Figure 4.1. These are representative of skin to organ depths. Since the detector is now shielded by a $33 \times 20 \times 2.5 \text{ cm}^3$ lead block, this additional shielding required the torso phantom to be placed 2.5 cm further from the collimator face. The neutron sources were moved 2.5 cm towards the collimator exit in order to maintain the same sensitivity as the original configuration. For the 4 cm lateral kidney depths only, the kidney was misaligned by 2 cm laterally with the central axis of the neutron beam so that the detector could be moved away from the neutron beam axis by 2 cm. So the kidney, torso phantom, and detector are moved laterally by 2 cm. The Monte-Carlo simulation shows moving the detector both axially (to incorporate the 2.5 cm of Pb

shielding) and 2 cm laterally effectively reduced the neutron fluence above 0.7 MeV (energy region considered to be the most dangerous for neutron damage in germanium (Darken 1980)) in the detector by a factor of about 3, and the total neutron fluence by about 2.3 for the closest detector position. This improvement suggests that the neutron beam is fairly well collimated. The kidney misalignment did not have an effect on the neutron capture rate in the kidney phantoms because the kidney phantom was still positioned within the dimensions of the collimated neutron beam.

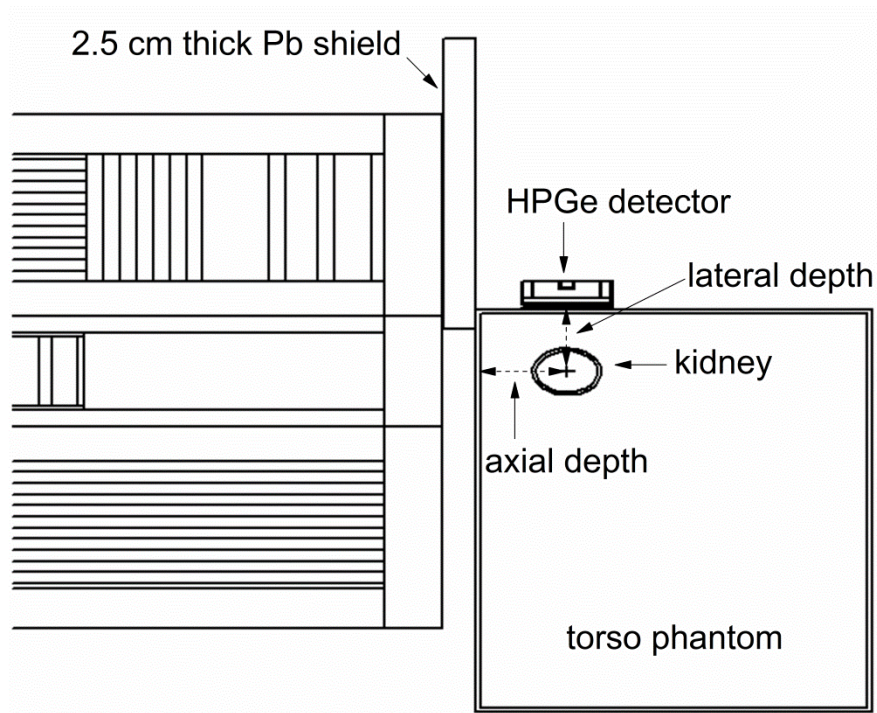


Figure 4.1. Geometry for the kidney phantom placed in 7 cm axial and lateral depths in the torso phantom. The detector is placed behind 2.5 cm of Pb photon shielding. (Monte-Carlo model of the geometrical set-up.)

The detection limits are calculated from four photon lines. This includes the 79.5 and 181.9 keV prompt gamma emissions from neutron capture of ^{157}Gd , and the K_{α} and K_{β} X ray transitions from internal conversion following neutron capture of both ^{155}Gd and

^{157}Gd . The detection limits are combined via the inverse variance weighted method to give the total detection limit M_{DL}^T :

$$(M_{DL}^T)^2 = \left(\sum \frac{1}{M_{DL_i}^2} \right)^{-1}$$

The total detection limits for the kidney in the 9 positions considered are shown in Figure 4.2. The uncertainty in the estimation of these detection limits is less than 6%. The uncertainties propagate from the error in the photon line emission probability per neutron capture, the source certification yield (3%), and the errors from the neutron and photon simulation (< 4% and on the order of 1% respectively). The detection limits range from 2.3 ppm (0.28 mg) Gd for the shallowest kidney depth considered to 35 ppm (4.4 mg) Gd for the greatest kidney depth. The detection limits in the kidney can be presented as an absolute mass (mg), since the kidney phantom size is small enough to be encompassed in the neutron beam. As an example, the detection limits for each line in the two extreme depths are shown in Table 4.1. In the shallowest depth the K_α X ray gives the best detection limit, but as the kidney is placed at greater depths the 181.9 keV gamma ray gives the best detection limit. This is because of a significantly higher attenuation of the X ray energies at these tissue thicknesses.

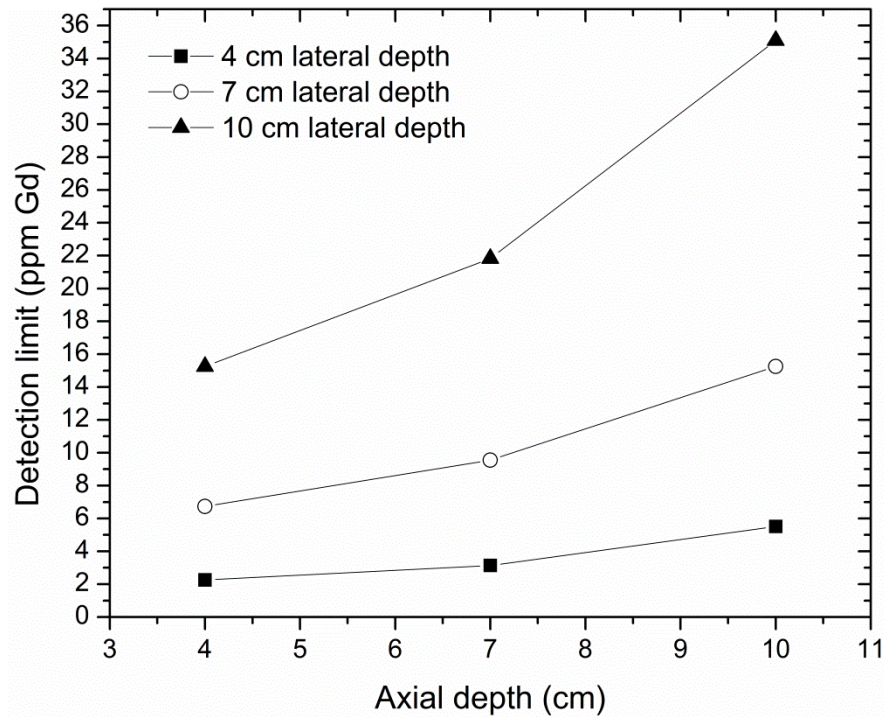


Figure 4.2. Gadolinium kidney detection limits for various overlying tissue thicknesses.

Table 4.1. Individual kidney detection limits for the shallowest and greatest depths considered (the positions represent lateral and axial depths respectively).

Transition	Photon energy (keV)	Detection limits (ppm; mg)	
		Position: 4 cm – 4cm	Position: 10 cm – 10 cm
K_{α} X ray	42.309, 42.996	(3.2; 0.39)	(68; 8.5)
K_{β} X ray	48.7, 50	(16; 2)	(321; 40)
Prompt γ ray	79.5	(5.4; 0.67)	(95; 11.9)
Prompt γ ray	181.9	(3.9; 0.49)	(46; 5.7)

The detection limits for the 6 liver positions are shown in Figure 4.3. The liver detection limits vary from 0.74 ppm to 4.3 ppm for the depths considered. The individual detection limits for the liver in the shallowest and greatest depth are shown in Table 4.2. It appears that the liver demonstrates reasonable detection limits over a wide variety of body types.

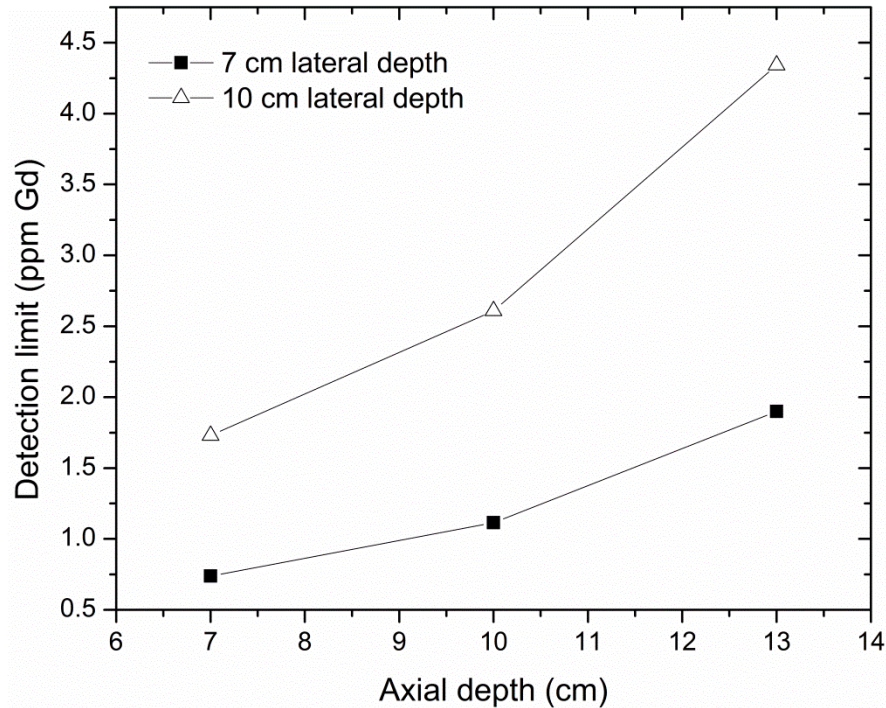


Figure 4.3. Gadolinium liver detection limits for various overlying tissue thicknesses.

Table 4.2. Individual liver detection limits for the shallowest and greatest depths considered (the positions represent lateral and axial depths respectively).

Transition	Photon energy (keV)	Detection limits (ppm)	
		Position: 7 cm – 7 cm	Position: 10 cm – 13 cm
K_{α} X ray	42.309, 42.996	1.19	8.6
K_{β} X ray	48.7, 50	5.3	36
Prompt γ ray	79.5	1.59	9.0
Prompt γ ray	181.9	1.20	6.1

Since the sensitivity is determined from the Monte-Carlo simulation, the detection limits calculated here are for the most ideal circumstances. However, based on the previously determined agreement between the model and the experiment, I suggest that these detection limits should be a fairly accurate estimation over many different body

types. In addition, the background error measurement for each phantom and detector position has been measured experimentally and therefore physical measurements are incorporated into these simulated detection limit estimates.

Chapter 5

Radiation dosimetry for the measurement of gadolinium by PGNAa using the $^{238}\text{Pu}/\text{Be}$ source-based system

5.1 Simulated phantom dosimetry

In order to justify the use of any radiation based technique and its application in studies of human health, it is necessary to determine the radiation dose delivered to the patient by the technique. One method which can be used to accomplish this is Monte Carlo computation. The dosimetry of this particular technique is calculated here using the Monte Carlo model of the irradiation facility developed in Chapter 3, and the Oak Ridge National Laboratory (ORNL) mathematical computer model of the adult male (Eckerman, Cristy & Ryman 1996, Krstić, Nikezić 2007). The ORNL adult male (AMALE) is an analytical computer model composed of all organs of the human body and with a height and weight representative of an ‘average’ adult male (Krstić, Nikezić 2007). The tissues are categorized as either skeletal, soft, or lung tissues, with densities and compositions adopted based on body composition surveys (Krstić, Nikezić 2007, ICRP 2002). The adult male model was arranged within the simulation geometry so that the target tissue was centered in the neutron beam. This was done for each of the lower leg muscle, kidney, and liver irradiation geometries: they are described in detail below. The Monte-Carlo model was then compared with experimental survey measurements as a method of validating the model.

The absorbed neutron dose to the target organs was calculated using the MCNP methodology called the ‘FM4 heating tally’. The FM4 tally was combined with DE/DF cards, which are lines of code in the input file which multiply the absorbed dose ($\text{J/kg} = \text{Gy}$) per neutron energy bin by appropriate radiation weighting factors, w_R . This calculated the conversion from absorbed dose, D , to the equivalent dose, H_T , in Sv. The neutron energy bin widths from Chadwick et al. (1999) were used so that a comparison

could be made between the Chadwick kerma coefficients and the heating numbers available in MCNP5. The radiation weighting factors used here are those given as a function of neutron energy by the International Commission on Radiological Protection (ICRP) in publication 60 (ICRP 1991), which were further modified in publication 103 (ICRP 2007). The doses were computed using both ICRP publications and are compared. For the computation of the equivalent dose based on the ICRP60 recommendations, EN/EM cards (instead of DE/DF cards), (that is, slightly different lines of code in the input file) were used. This is because the w_R are given as a step function in ICRP60 and the EN/EM cards allow for histogram binning of the absorbed dose and subsequent multiplication of the w_R . The w_R in ICRP103 are a continuous function of neutron energy and therefore the DE/DF cards were used in this instance.

The photon doses were calculated using a method called by MCNP the ‘F6 tally’ which is equivalent to the kerma approximation FM4 tally. Since the radiation weighting factor for photons of all energies is 1, the absorbed dose for photons in Gy is equal in magnitude to the equivalent dose in Sv. A tally called ‘*F8’ which calculates energy deposition was also computed and the result divided by the cell mass to determine the dose. The *F8 tally was computed as a secondary check to confirm the results obtained from the F6 tally.

Finally, the potential dose enhancement from the presence of Gd in tissues is considered in detail, and some discrepancies in nuclear data tables are discussed.

5.1.1 Lower leg muscle irradiation

The lower leg muscle is one of the target locations for the measurement of gadolinium retention. The measurement requires the participant to position their lower left leg muscle against the collimator exit of the irradiation facility. In the model, the left leg of the computer phantom is positioned in front of the collimated beam of neutrons from the $^{238}\text{Pu}/\text{Be}$ isotopic source. The Monte-Carlo geometry is shown in Figure 5.1. Due to geometric constraints between the model of the adult male and the irradiation

facility, the collimating apparatus needed to be moved 2.8 cm away from the leg of the adult male model. This removed any problems with intersections in the torso of the phantom and the irradiation facility. In order to keep the same distance effect on the dose to the phantom from the neutron beam, the sources were moved 2.8 cm closer to the exit face of the collimator. This may have an effect on reducing the beam collimation; however, this is not expected to have a significant effect on the dose estimates at these particular dose levels. In the adult, there is no active red bone marrow in the tibia, but there is in the femur (Cristy 1981). Therefore, in order to account for this in the calculation of the effective dose to the radiosensitive tissues defined by the ICRP (ICRP 1991, ICRP 2007), the ORNL phantom model was modified to separate the leg bone into two sections. The bottom section being designated as the tibia, and the top section designated as the femur. In the original ORNL phantoms the skin is defined as one cell, in this study the cell was separated to determine the leg skin dose only.

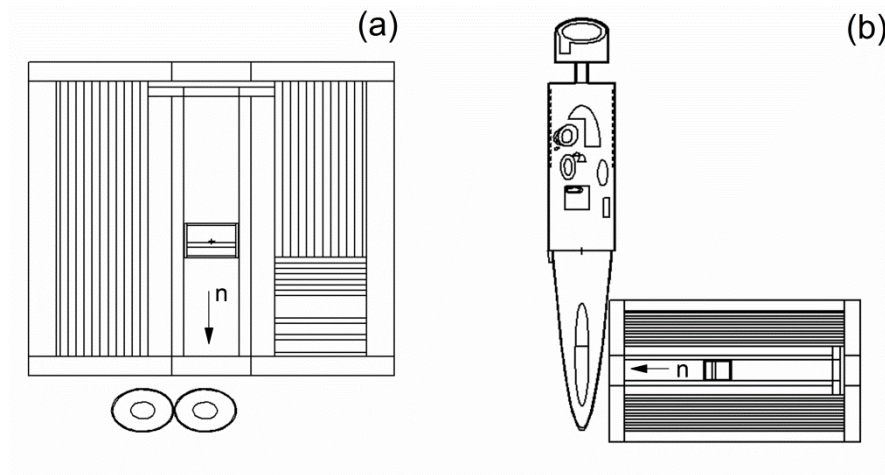


Figure 5.1. The top (a) and side view (b) of the irradiation geometry for the lower leg muscle. Image output from MCNP Visual Editor.

The neutron and photon dose components for the leg irradiation geometry are listed in Table 5.1. The tissue weighting factors, w_T , in Table 5.1 are from ICRP publication 103 (2007). The w_T converts the equivalent dose to the effective dose, E , taking into account the relative radio-sensitivities of the organs of the body. The table

gives the equivalent dose rate (H_T^*) components to the tissues considered, and also shows the different radiosensitive tissues that were considered in this calculation of the effective dose. The tissue fractions were estimated from ICRP publication 89 (ICRP 2002), descriptions of how these tissue fractions were determined are given in the footnotes to Table 5.1. The relative statistical uncertainties from the computation are also given in the table. A 3% error could also be added in quadrature to the relative uncertainties to account for the error in the source emission rate. The main tissues contributing to the effective dose are the muscle and skin. The bone tissues are reasonably shielded by the skin and muscle. The effective dose rate (E^*) for the leg irradiation is quite low at 1.1 $\mu\text{Sv/hr}$ (1.07 $\mu\text{Sv/hr}$ using the recommendations in ICRP60). In a typical year we are exposed to 3000 μSv of radiation from natural sources of radiation and radioactivity. During one leg muscle scan (2000 s), the participant is exposed to a dose that is the same as that which one would receive from natural sources in 1.8 hours of daily life, that is, 0.6 μSv . In other words, this radiation exposure is extremely low. In addition, for an adult, the measurement is approximately 50 times less dose than a panoramic dental X ray and about 135 times less dose than a standard chest X ray. I suggest, therefore, that this exposure is justifiable as a routine measurement procedure for Gd retention in muscle, as the exposure levels are so much lower than routine diagnostic X-ray imaging procedures. Although the dose to the radiosensitive tissues were calculated for the adult male phantom, no other tissues or organs, especially sex specific organs were considered as they were located far enough from the irradiation site not to contribute to the effective dose significantly. Therefore, the doses calculated here can be applied to both sexes.

Table 5.1. MCNP calculated dose rates to the leg tissues of the ORNL adult male phantom.

ORNL phantom tissue	Neutron \dot{H}_T ($\mu\text{Sv/hr}$)	Photon \dot{H}_T ($\mu\text{Sv/hr}$)	Total tissue \dot{H}_T ($\mu\text{Sv/hr}$)	Tissue	^a w_T	^c Tissue fraction	\dot{E}^* ($\mu\text{Sv/hr}$)
Leg soft tissue	154 (0.5)	10 (0.4)	164	muscle	^b 0.009	^d 0.275	0.41
Femur	10 (4.7)	9 (1)	19	bone marrow	0.12	^e 0.037	0.084
				bone surface	0.01	^f 0.05	0.0095
Tibia	268 (0.9)	12 (0.7)	280	bone marrow	0.12	^g 0	0
				bone surface	0.01	^h 0.04	0.12
Leg skin	230 (0.5)	11 (0.4)	241	skin	0.01	ⁱ 0.2	0.48
Total							1.1

Relative errors in % are given in parenthesis.

^a tissue weighting factors are from ICRP 103.

^b muscle is part of the 13 remainder organs with weighting factor 0.12, therefore the tissue weighting factor for muscle is $0.12/13 = 0.009$

^c calculated from data in ICRP 89.

^d In the adult 55% of the skeletal muscle is in the lower extremities. The tissue fraction for the skeletal muscle of one leg is half this value.

^e In the adult (25 yrs old) 7.4% of the active bone marrow is contained in the upper half of the femora (Cristy 1981). The resultant tissue fraction of bone marrow in the femur is $0.074/2 = 0.037$. The division by 2 is for the calculation of the dose to one leg.

^f In the adult the femora amounts for 15.3% of the total fresh skeletal mass. It is assumed that the bone surface is composed of cortical bone, for the femur cortical bone amounts to 67% of the mass. The resultant tissue fraction of cortical bone in the femur is $0.153 \times 0.67/2 = 0.05$. The division by 2 is for the calculation of the dose to one leg. Calculation of the fraction of bone surface, is in fact, much more complicated than this, but it is expected that the estimate here will provide a conservative estimate.

^g The adult tibiae contain no active bone marrow.

^h In the adult the tibiae and fibulae amount to 11.3% of the total fresh skeletal mass. The cortical bone amounts to 74% of tibia mass. The resultant tissue fraction of cortical bone in the tibia is $0.113 \times 0.74/2 = 0.04$. The division by 2 is for the calculation of the dose to one leg.

ⁱ mass fraction

5.1.2 Kidney irradiation

The kidney irradiation geometry is shown in Figure 5.2. The individual neutron and photon equivalent doses for each organ considered are shown in Table 5.2, and the effective dose components are shown in Table 5.3. The statistical uncertainties for the simulated dose to each organ are also given in Table 5.2. The uncertainties are generally less than 3.5% and 1.2% for the neutron and photon simulations, respectively. However the brain, bladder, thymus, and gonads did have significantly larger uncertainties in the neutron doses. As an example, the gonads (testes) in the male, a radiosensitive tissue, had an uncertainty of 42%. The reason for this large relative uncertainty is that the gonads are a small organ located far away from the incident neutron field and shielded by the rest of the body. This would be somewhat similar for the female ovaries. To reduce the uncertainty to the 10% level, 3 days of computation time would be required. For practical purposes this was not performed as these organs will have a combined contribution to the overall effective dose of less than 0.9%. The organs for which there is a tabulated ICRP radiation weighting factor, but were not included in the effective dose calculation, are the thyroid, lymphatic nodes, oral mucosa, salivary glands, and prostate. These organs like the brain, bladder, thymus, and gonads are far enough away from the irradiation site that they are not exposed to a significant radiation dose. In addition, these organs, with the exception of the thyroid, are not included in the ORNL phantom geometry. The soft tissue region of the trunk surrounding the organs was considered to be composed entirely of muscle. This is meant to be a conservative estimate as there is only a tissue weighting factor for muscle as opposed to adipose tissue which is not considered in the estimate of radiation risk by the ICRP. The bone dose listed in Table 5.2 is for the total dose to the ribs and spine, this dose is further separated in the calculation of effective dose into the cortical and trabecular components in order to determine the dose to the bone surface and bone marrow, respectively. The kidney dose in Table 5.2 is averaged over both kidneys, the neutron equivalent dose rate to the left kidney is 1.78 mSv/hr, and the photon equivalent dose rate is 0.038 mSv/hr. The organs receiving the largest equivalent doses

are the kidneys, spleen, stomach and colon. This is expected as these organs are closest to or are directly targeted by the collimated neutron beam. The photon dose component contributes about 8% to total equivalent dose. The organ receiving the largest contribution to the effective dose is the stomach (45%), and the second largest contribution is the dose to the kidneys (12%), followed by the colon (11%) and the bone marrow (9%). The overall effective dose rate for the kidney irradiation geometry for the adult male is 74 $\mu\text{Sv/hr}$. A similar value would be expected for the adult female as the uterus/cervix, breast, and ovaries are all located a significant distance away from the incident neutron beam and therefore expected to receive negligible dose. The effective dose calculated using the ICRP60 recommendations is comparable at 75 $\mu\text{Sv/hr}$.

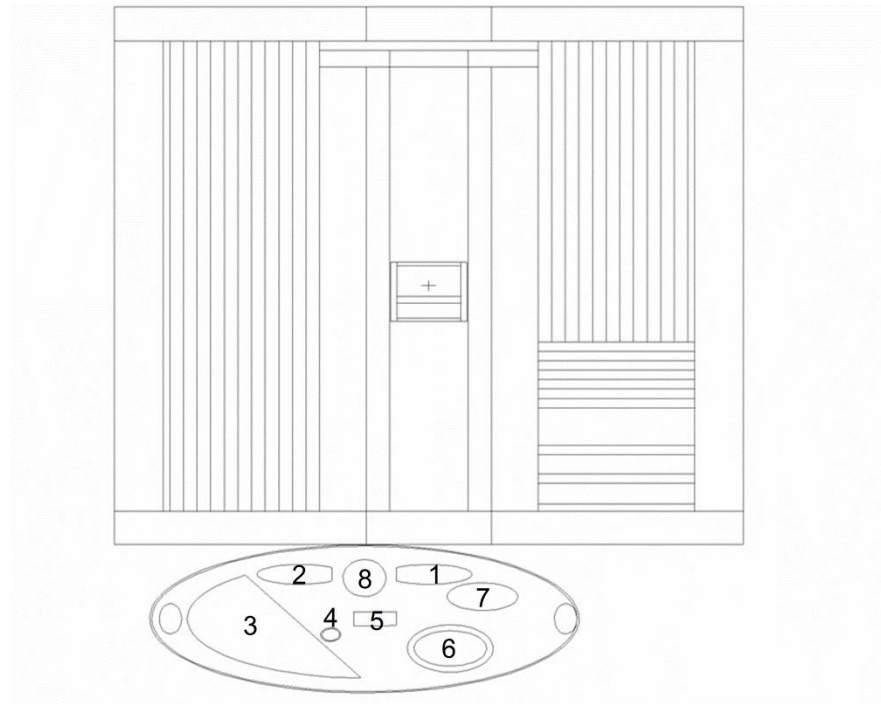


Figure 5.2. Kidney irradiation geometry showing the (1) left kidney aligned with the collimated neutron beam from the irradiation facility. Also visible in this plane are the (2) right kidney, (3) liver, (4) gall bladder, (5) pancreas, (6) stomach, (7) spleen, and (8) spinal cord. Image adapted from MCNP Visual Editor.

Table 5.2. MCNP calculated equivalent dose rates to the organs at risk for the kidney irradiation geometry.

Organ/Tissue	Neutron H_T ($\mu\text{Sv/hr}$)	Photon H_T ($\mu\text{Sv/hr}$)	Total H_T ($\mu\text{Sv/hr}$)
^a Bone	33.6 (0.6), 144 (0.7)	7.10 (0.3), 16.5 (0.4)	201
Colon	57.1 (1.2)	8.69 (0.5)	65.8
Lung	12.3 (1.9)	7.23 (0.4)	19.5
Stomach	258.2 (0.9)	16.36 (0.5)	275
Gonads	0.4 (42)	1.8 (3.7)	2.2
Bladder	3.2 (10)	3.94 (1.4)	7.2
Oesophagus	34 (3.5)	9.07 (0.95)	43
Liver	20.5 (1.7)	8.88 (0.4)	29
Brain	2.3 (6.5)	3.07 (0.9)	5.4
Skin	72.1 (0.3)	7.61 (0.15)	79.7
Remainder tissues			
Adrenals	197 (2.6)	22.5 (1.1)	219
Gall bladder	70 (3.2)	11.8 (1.2)	82
Heart	14.1 (3.3)	7.52 (0.7)	21.6
Kidneys	924 (0.4)	28.5 (0.7)	952
Muscle	50.3 (1.7)	5.77 (0.9)	56.1
Pancreas	251 (1.2)	18.7 (0.7)	270
Small intestine	74.8 (1.0)	11.5 (0.4)	86.3
Spleen	466 (0.8)	23.1 (0.5)	490
Thymus	2.1 (25)	3.4 (2.8)	5.5
Total	2687	223	2910

Relative errors in % are given in parenthesis.

^a Total dose to ribs and spine, respectively

Table 5.3. MCNP calculated effective dose components for the kidney irradiation.

Organ/Tissue	w_T	Tissue fraction	E ($\mu\text{Sv/hr}$)	% of total E
Bone marrow (red)	0.12	(^a 0.152, ^b 0.307)	6.7	9.05
Colon	0.12	1	7.89	10.7
Lung	0.12	1	2.34	3.18
Stomach	0.12	1	33	44.8
Gonads	0.08	1	0.18	0.24
Bladder	0.04	1	0.29	0.39
Oesophagus	0.04	1	1.71	2.32
Liver	0.04	1	1.18	1.60
Bone surface	0.01	(^c 0.066, ^d 0.065)	0.13	0.18
Brain	0.01	1	0.05	0.07
Skin	0.01	^e 0.49	0.39	0.53
^f Remainder tissues	0.12			
Adrenals		1	2.0	2.75
Gall bladder		1	0.8	1.02
Heart		1	0.20	0.27
Kidneys		1	8.8	11.9
Muscle		^e 0.42	0.2	0.30
Pancreas		1	2.5	3.38
Small intestine		1	0.80	1.08
Spleen		1	4.5	6.14
Thymus		1	0.05	0.07
		Total	73.7	100

^a For ribs; bone marrow = 15.2 % (Cristy 1981)^b For spine; bone marrow = 30.7 % (Cristy 1981)^c For ribs; (% bone mass \times % cortical) = 0.07×0.94 ^d For spine; (% bone mass \times % cortical) = 0.19×0.34 ^e mass fraction^f The radiation weighting factor is applied to the mean dose from the 13 remainder tissues (not all 13 are listed here, see text); based on the recommendations of the ICRP (2007) the mean dose is weighted by 0.12 and divided by 13.

5.1.3 Liver irradiation

The liver irradiation geometry is shown in Figure 5.3. The individual neutron and photon equivalent dose rates for each organ considered are shown in Table 5.4, and the effective dose components are shown in Table 5.5. The liver and gall-bladder receive the largest total equivalent doses, with dose rates of 606 and 476 $\mu\text{Sv/hr}$, respectively. The main organs contributing to the overall effective dose are the liver (51%), colon (11%), gall-bladder (9%), stomach (8%), and lung (7%). The overall effective dose rate for the liver irradiation geometry is 48 $\mu\text{Sv/hr}$ when using the recommendations of ICRP103. The effective dose rate is comparable at 46 $\mu\text{Sv/hr}$, when using the ICRP60 recommendations. The effective dose rate using the ICRP60 recommendations should, in fact, be higher since the w_R for liver is 0.05 compared to 0.04 in ICRP103. One of the reasons the ICRP60 calculated dose is not significantly higher than the ICRP103 calculated dose is because there is no w_R for the gall-bladder in the ICRP60 recommendations.

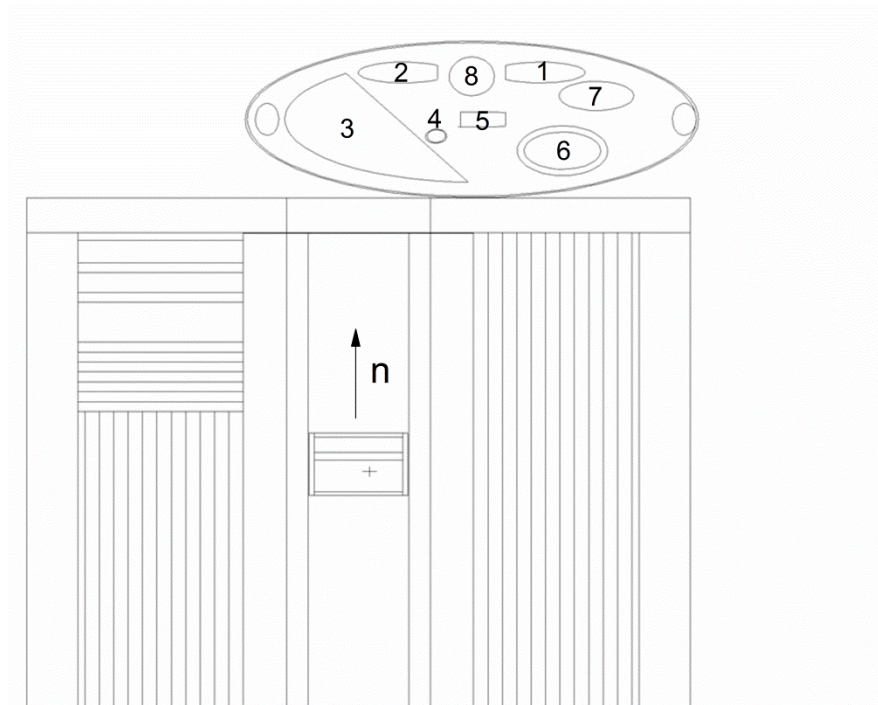


Figure 5.3. Liver irradiation geometry showing the (3) liver aligned with the collimated neutron beam from the irradiation facility. Also visible in this plane are the (1) left kidney, (2) right kidney, (4) gall bladder, (5) pancreas, (6) stomach, (7) spleen, and (8) spinal cord. Image adapted from MCNP Visual Editor.

Table 5.4. MCNP calculated equivalent dose rates to the organs at risk for the liver irradiation geometry.

Organ/Tissue	Neutron H_T ($\mu\text{Sv/hr}$)	Photon H_T ($\mu\text{Sv/hr}$)	Total H_T ($\mu\text{Sv/hr}$)
^a Bone	56.3 (0.5), 15.9 (1.9)	6.91 (0.3), 6.19 (0.6)	85.3
Colon	34.7 (1.5)	9.34 (0.4)	44.0
Lung	21.5 (1.4)	7.00 (0.4)	28.5
Stomach	18.9 (3.2)	12.26 (0.6)	31.2
Gonads	1.5 (25)	2.73 (2.9)	4.3
Bladder	3.5 (9.2)	4.70 (1.3)	8.2
Oesophagus	12.1 (5.4)	6.47 (1.1)	18.6
Liver	584 (0.3)	21.98 (0.3)	606
Brain	2.3 (6.2)	3.58 (0.8)	5.9
Skin	72.6 (0.3)	7.02 (0.2)	79.6
Remainder tissues			
Adrenals	52 (4.7)	9.1 (1.7)	60.5
Gall bladder	453 (1.2)	23.45 (0.8)	476
Heart	14.1 (3.1)	9.68 (0.6)	23.7
Kidneys	90 (1.3)	8.9 (2.2)	99
Muscle	33.2 (1.7)	4.80 (0.9)	38.0
Pancreas	42 (3.2)	11.4 (0.8)	53
Small intestine	30.8 (1.5)	10.21 (0.4)	41
Spleen	5.5 (7.5)	5.7 (1.1)	11.2
Thymus	5.8 (15)	6.3 (2.1)	12.0
Total	1548	178	1726

Relative errors in % are given in parenthesis.

^a Total dose to ribs and spine, respectively

Table 5.5. MCNP calculated effective dose components for the liver irradiation.

Organ/Tissue	w_T	Tissue fraction	E ($\mu\text{Sv/hr}$)	% of total E
Bone marrow (red)	0.12	(^a 0.152, ^b 0.307)	1.97	4.1
Colon	0.12	1	5.28	11.0
Lung	0.12	1	3.42	7.1
Stomach	0.12	1	3.75	7.8
Gonads	0.08	1	0.34	0.71
Bladder	0.04	1	0.33	0.68
Oesophagus	0.04	1	0.74	1.5
Liver	0.04	1	24.22	51
Bone surface	0.01	(^c 0.066, ^d 0.065)	0.06	0.12
Brain	0.01	1	0.06	0.12
Skin	0.01	^e 0.49	0.39	0.81
^f Remainder tissues	0.12			
Adrenals		1	0.56	1.2
Gall bladder		1	4.40	9.2
Heart		1	0.22	0.46
Kidneys		1	0.92	1.9
Muscle		^e 0.42	0.15	0.31
Pancreas		1	0.49	1.0
Small intestine		1	0.38	0.79
Spleen		1	0.10	0.22
Thymus		1	0.11	0.23
		Total	47.9	100

^a For ribs; bone marrow = 15.2 % (Cristy 1981)^b For spine; bone marrow = 30.7 % (Cristy 1981)^c For ribs; (% bone mass \times % cortical) = 0.07×0.94 ^d For spine; (% bone mass \times % cortical) = 0.19×0.34 ^e mass fraction^f The radiation weighting factor is applied to the mean dose from the 13 remainder tissues (not all 13 are listed here, see text); based on the recommendations of the ICRP (2007) the mean dose is weighted by 0.12 and divided by 13.

5.2 Benchmark measurements: comparison of experimental and simulated dose rates

It is, of course, important to benchmark Monte Carlo results against experimental measurements. Neutron dosimetry was performed experimentally with an Anderson-Braun type detector (“Snoopy”, Tracerlab NP-1 Serial No. 5109), as well as with a Tissue Equivalent Proportional Counter (TEPC) (Rem-500 Neutron Survey Meter, Far West Technology, Inc.). Photon dosimetry was performed experimentally with an ionization chamber (Nuclear Enterprises LTD, Portable Dose RateMeter Type PDR2 Serial No. 375). The neutron and photon dose rates are determined in MCNP5 by combining the fluence rates at the detector positions with the fluence-to-ambient dose equivalent conversion coefficients published in ICRP 74 (ICRP 1996). The Rem-500 and ionization chamber measurements were performed at the collimator exit face. The Snoopy detector was placed directly against the collimator face, but due to its relatively large size, the position of the dose rate it measures is assumed to be at its center (which is located ~10.75 cm away from the exit face).

The results of the simulation and experimental survey measurements are shown in Table 5.6. The variability in the air ionization chamber measurement is due to the orientation of the hand-held device in the photon field (the lowest value was measured with the side facing the beam opening, and the highest was measured with the front of the hand-held detector facing the beam opening). A remarkably good agreement is seen between the simulated and surveyed dose rates. The statistical uncertainty in the MCNP calculated dose rates are less than 0.7%. The simulated Rem-500 dose rate is a factor 1.06 times higher than the measured dose rate, and this is more than satisfactory when comparing non-normalised *ab initio* simulation with experiment. The simulated dose rate for the Snoopy detector is a factor of 1.25 times higher than the measured dose rate. The Snoopy detector is calibrated by National Research Council Canada (NRCC). The measured Snoopy dose rate was adjusted based on the calibration coefficients for angular response and for the analogue scale used (NRC Report No. IRS-2007-1117). The

differences observed between simulation and experiment could be due to the differences in the calibration set-up of the NRC and this experimental geometry which consists of a neutron beam from a collimated $^{238}\text{Pu}/\text{Be}$ source. However, the fact that MCNP slightly overestimates the neutron dose is acceptable as this results in a conservative estimate of the dose to a subject. The simulated photon dose rate appears slightly lower than measured. This could possibly be due to neutron contribution to the measured dose rate, and the fact that the simulation does not take into account the gamma rays emitted from the ^{238}Pu decay. However, the photon contribution to the overall dose rates is small (less than 10%), and therefore any underestimation will be of small significance in the final dose estimate. The agreement provides confidence in the derived effective dose rates calculated for the phantoms above. Therefore, I suggest that the Monte Carlo model can be used reliably to determine the dose to an ‘average’ patient for various irradiation configurations. There will, of course, be small variations in the actual dose received by individuals which depend on each person’s size, shape, weight and body composition.

Table 5.6. Comparison of simulated and measured survey dose rate measurements.

Detector	MCNP dose rate (mSv/hr)	Measured dose rate (mSv/hr)	Radiation field
^a Snoopy	1.20	0.96 ± 0.06	neutron
^b Rem-500	2.84	2.67 ± 0.01	neutron
^c Air ionization chamber	0.036	0.05 - 0.07	photon

^a Detector was placed against the collimator exit face; the BF_3 counter is located 10.75 cm deep within the polyethylene cylinder.

^b Center of detector is directly aligned with the collimator exit face centered in the neutron beam.

^c The air ionization chamber is calibrated with tolerance limits of 20%.

5.3 Gadolinium dose enhancement

Neutron capture therapy (NCT) is a two-step process in which a drug carrying a high neutron absorbing material is selectively targeted to tumour cells and subsequently

irradiated by a neutron field. The idea is that neutrons would be absorbed preferentially in the tumour because of interactions with the drug and the reaction products would ideally deposit their energy locally, providing a high tumour-to-normal tissue dose ratio. In practice, this goal has proven to be quite elusive, and NCT still remains investigational. This is because of the difficulty in developing drugs that selectively deposit in tumour cells. The concept of NCT has been under investigation since the mid 1930s (Slatkin 1991). The main compounds investigated contained ^{10}B as the principal neutron capture agent. Neutron capture with ^{10}B results in the emission of an alpha particle and a ^7Li ion. These heavy particles share 2.79 MeV of kinetic energy, and have a short range in tissue on the order of 10 μm , and subsequently deposit all their energy in a small localized volume. More recently Gd has been proposed for neutron capture therapy (Miller et al. 1993, Stepanek 2003, Goorley, Nikjoo 2000, Salt et al. 2004, Yasui et al. 2008). This is due to the enormous thermal neutron capture cross section of Gd and the fact that 7.94 MeV (Q -value) of energy is released per neutron capture with ^{157}Gd ($\sigma_o = 254\,000\text{ b}$). The energy released is mostly given to penetrating prompt gamma ray radiation; taking away more than 99% of the Q -value (Miller et al. 1993). The remaining energy is given to internal conversion (IC) electrons, and subsequently to the emission of Auger and characteristic X rays (Miller et al. 1993, Sakurai, Kobayashi 2002). Gadolinium is now routinely used as a contrast agent in MRI and since the contrast agents selectively pool in tumour regions these agents could be potentially applied as NCT agents (Franken et al. 2006, De Stasio et al. 2001). The literature has proposed variable mechanisms for the effectiveness of NCT with Gd. Some groups have proposed that the photon dose, which is not in fact localized, provides the beneficial dose enhancing effect (with some contribution from internal conversion electrons) (Miller et al. 1993, Wangerin, Culbertson & Jevremovic 2005, Culbertson, Jevremovic 2003, Matsumoto 1992). This would mean that there is no requirement for a therapeutic agent which is selectively accumulated in the tumour. Other groups propose that the agents must be taken-up by the tumour cells and located intranuclearly so that the short range and biologically damaging high linear energy transfer (LET) Auger electrons can inactivate the tumour cells by directly

producing DNA double-strand breaks (Salt et al. 2004, Yasui et al. 2008, De Stasio et al. 2001, Goorley, Zamenhof & Nikjoo 2004). The path lengths of the Auger electrons are on the order of nano-meters to a few micro-meters (Stepanek 2003, Goorley, Nikjoo 2000) and if this second hypothesis of direct DNA damage is valid, then if the Gd is located extra-cellularly, these short range Auger electrons will deposit their energy outside the cell, and therefore no radiological advantage will be achieved.

The goal of this thesis work is not therapy, but diagnosis, and so less dose enhancement would be preferred. The technique should have as low a risk as possible. The contrast agents studied in this thesis are extracellular agents, and studies of *in vitro* uptake kinetics of the contrast agent Gd-DTPA on human glioblastoma cells demonstrate only moderate cellular uptake on the order of a few percent (Salt et al. 2004, De Stasio et al. 2001). The cell culture exposure times ranged from 24 hr to 120 hr, and are therefore much longer than the *in vivo* biological elimination half-life, 1-2 hr, for the routinely used MRI contrast agents.

It appears that the dose enhancement due to Gd in tissues is a very complex process and relies on knowledge of Gd agent uptake kinetics and very precise knowledge of the excited state decay characteristics of $^{158}\text{Gd}^*$. An attempt is made below to understand this complex process further and to contextualize any excess risk. For the purposes of this current research the microscopic dose enhancing DNA damage from Auger electron emission can be neglected, due to the negligible cellular uptake of routinely used Gd-based contrast agents, and only macroscopic dose effects need to be considered.

To calculate the dose in MCNP, users can use the available heating table information from ENDF that comes with the MCNP version 5 package, input their own kerma values, or input accepted neutron kerma coefficients (Chadwick et al. 1999). As I shall discuss in the following sections, there is some discrepancy in the nuclear heating data available for Gd. The Chadwick neutron kerma coefficients were developed for biologically relevant isotopes only, as at the time there was no obvious need for non-biologically relevant materials when dealing with human radiation dosimetry. In this case,

the kerma coefficients were initially not accurately known for Gd, because there had been no concern regarding neutron irradiation of Gd in the human body. However, as new applications for Gd have developed, such as in magnetic resonance imaging, and the proposed use in neutron capture therapy, it has become more critical to develop accurate dosimetry data for Gd. This thesis describes a method to measure Gd retention by PGNA and care must be taken in dosimetry calculations if this technique is to be justified as a non-invasive low risk monitoring procedure.

5.3.1 Macroscopic Gd dose enhancement: a comparison of ENDF data

The proposed use of gadolinium agents for NCT raises the question of whether there is an enhancement of dose due to the presence of Gd in tissue during *in vivo* measurements of Gd retention using NAA. In a first test to assess the potential macroscopic dose enhancement, a simulation was performed to determine the dose to an ICRU sphere (International Commission on Radiation Units and Measurements). An ICRU sphere is a tissue equivalent sphere with density 1 g/cm³, a diameter of 30 cm, and tissue composition of 76.2% oxygen, 2.60% N, 10.1% H, and 11.1% C by weight. In the simulation, the ICRU sphere was centered at the end of the collimator and the dose to the sphere from the ²³⁸Pu/Be source was calculated as a function of Gd concentration. This was performed using three different material data tables (called ZAIDs in MCNP) for gadolinium, 64157.55c, 64157.60c, and 64157.70c, which represent cross section and nuclear data from ENDF-B-V.0:T (1986), ENDF-B-VI.0 (1977) and ENDF-B-VII.0 (2006), respectively (evaluation date in parentheses).

The dose is calculated in MCNP by using the ‘heating numbers’ H(E) which are in units of MeV per collision. Using the H(E) method to calculate the neutron dose, the neutron fluence is integrated over the interaction cross section as well as the H(E), and therefore these heating numbers act much like a kerma coefficient. The kerma is the

kinetic energy released to matter by neutral radiation. The final result is multiplied by a conversion factor which converts the dose into S.I. standard units of J/kg (Gy) (described in detail in the following section). A comparison was made between the dose calculated using the $H(E)$ from the most recent nuclear data available in MCNP5, ENDF-B-VII.0, and the kerma coefficients from Chadwick et al (1999). The neutron absorbed dose rate as a function of energy for the energy bins given in Chadwick et al (1999) are compared in Figure 5.4. The neutron fluence rate spectrum is also shown on the secondary y-axis. The ratio of MCNP to Chadwick calculated absorbed dose ranged from 0.95 to 1.03 over all the energy bins above thermal, with an average of 0.99 ± 0.01 . In the thermal neutron energy bin the ratio was 1.4, suggesting some discrepancies in the kerma coefficients of ^1H and ^{14}N , as neutron captures with these elements are the main contributors to dose in tissues in the thermal neutron energy region. On further analysis, it appears that one reason for the difference is the energy deposited from the $^{14}\text{N}(n,p)^{14}\text{C}$ reaction. The MCNP kerma is a factor 1.98 larger than the Chadwick (1999) kerma in the thermal energy bin for this reaction, and the average ratio is 1.0 ± 0.1 for the remaining energy bins. It will be shown below that there are also discrepancies in the data for ^1H . There was no difference in the total calculated absorbed dose rate of $15 \mu\text{Gy/hr}$ to the ICRU sphere for both data-sets. It is obvious from Figure 5.4 that the largest contribution to the absorbed dose is from high energy neutrons above 0.01 MeV, despite the fact that they are the smallest contribution to the neutron fluence rate. This has been acknowledged previously in the work by Atanackovic et al. (2007).

The equivalent dose rate, which is the absorbed dose rate folded in with the neutron radiation weighting factors from one of the two relevant ICRP publications (ICRP60 and ICRP103) is shown in Figure 5.5. It is clear that the main contribution to dose is from the high energy, radio-biologically damaging neutron components of the $^{238}\text{Pu/Be}$ source. These neutrons do not contribute to system sensitivity and only contribute to radiation dose. The shape of the equivalent dose rate as a function of neutron energy in Figure 5.5 is similar to the absorbed dose rate in Figure 5.4. This is because the radiation weighting factors (unfortunately) roughly match the shape of the absorbed dose

rate curve from the $^{238}\text{Pu}/\text{Be}$ source as function of energy. The recently adopted ICRP103 radiation weighting factors are a continuous function of neutron energy as opposed to the older ICRP60 step function; both are shown in Figure 5.5. One significant difference is the recently adopted radiation weighting factor of 2.5 for thermal neutrons compared to the older factor of 5. The equivalent dose rate to the ICRU sphere using the ICRP103 weighting factors was 212 $\mu\text{Sv/hr}$, 7% higher than that calculated using the ICRP60 weighting factors. This is mainly due to the larger neutron radiation weighting factors in the $\sim 2\text{-}6$ MeV region (main region contributing to dose; see Figure 5.4) for the continuous w_R function of ICRP103 (shown in Figure 5.5).

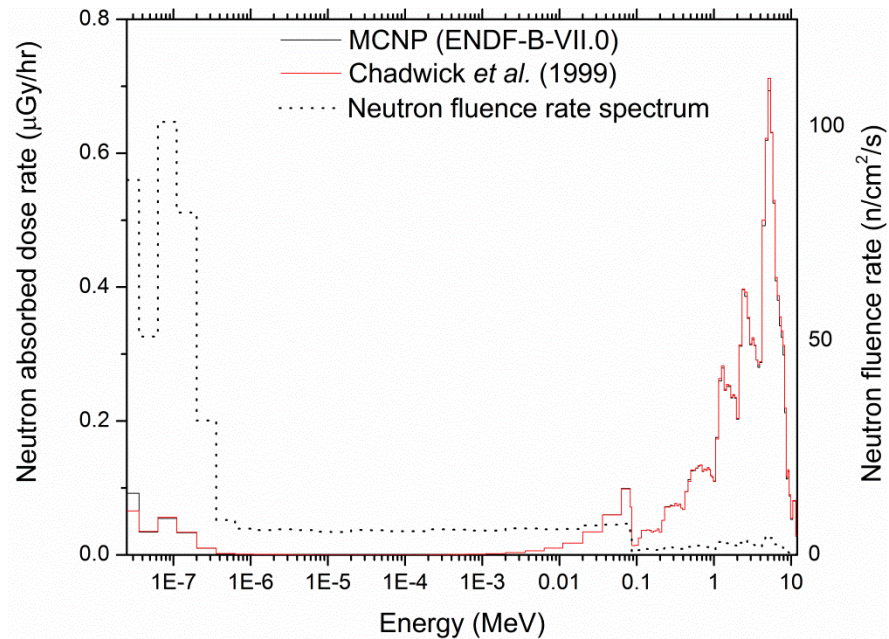


Figure 5.4. Comparison of the absorbed dose rate to an ICRU sphere from two kerma data-sets as a function of neutron energy from the $^{238}\text{Pu}/\text{Be}$ source. Also shown is the neutron fluence rate spectrum.

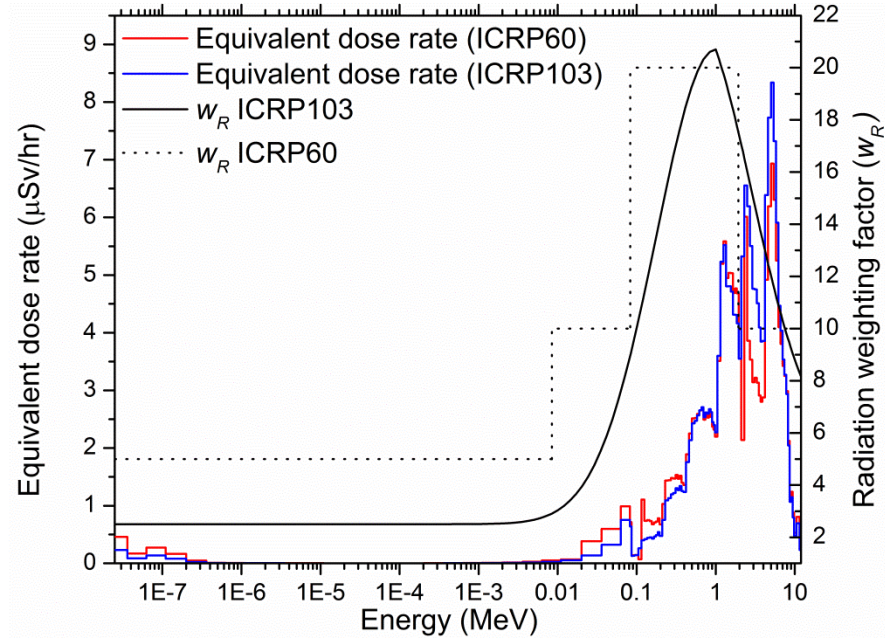


Figure 5.5. The equivalent dose rate to an ICRU sphere as function on neutron energy, calculated based on the ICRP60 & 103 recommendations. Also shown are the ICRP60 & 103 radiation weighting factors.

The absorbed dose as function of Gd concentration for the three different data libraries are shown in Figure 5.6. A significant dose enhancement is observed for the ENDF-B-V.0 and ENDF-B-VI.0 data, and no dose enhancement for the ENDF-B-VII.0 data. The statistical uncertainties in the computation are less than 2%. The heating numbers, obtained from the graphing interface on the MCNP Visual Editor for ENDF-B-V.0 (same as ENDF-B-VI.0) and ENDF-B-VII.0 are shown in Figure 5.7. The heating numbers from ENDF-B-V.0 are many orders of magnitude higher than that of ENDF-B-VII.0. The trends appear similar at low energies, but for energies approaching ~1 keV and above, they are remarkably different. The ENDF-B-V.0 data are actually an updated data set (MISC5XS) and it is acknowledged in the MCNP manual (Appendix G) that the photon-production data are only valid up to 1 MeV. It also states on the website for the Los Alamos National Laboratory (LANL) that since the photon data are added to the existing data set, the neutron heating data are incorrect (LANL 2006). It is subsequently acknowledged in Chadwick et al (2006) that there were energy balance issues found in

processing the ^{157}Gd data for the older versions, and this has been resolved in the recent data (ENDF-B-VII). Nevertheless, the kerma from Gd neutron capture is investigated further in the subsequent sections.

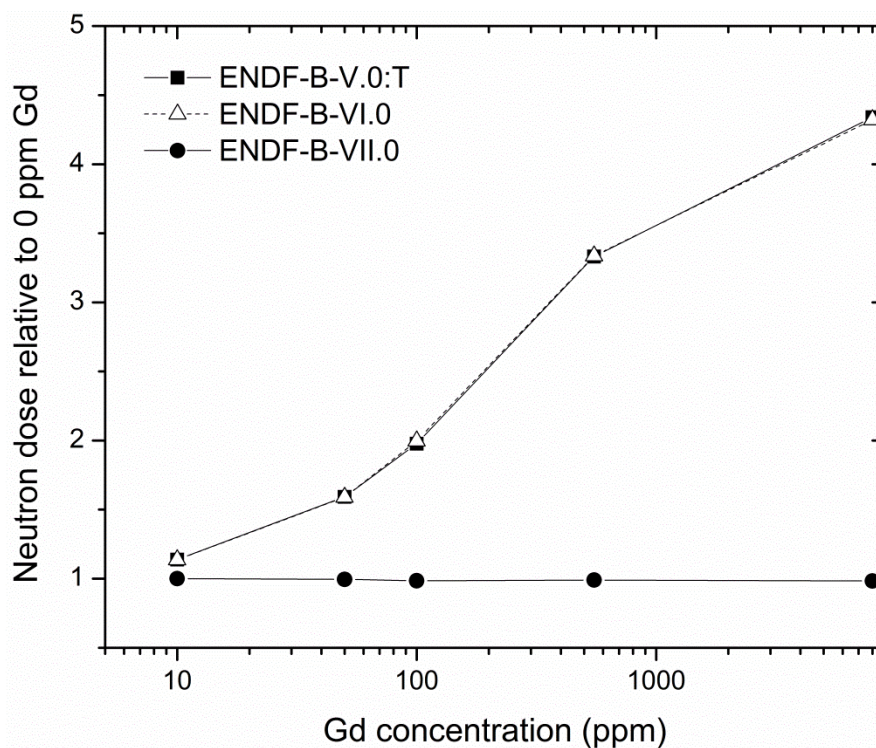


Figure 5.6. Neutron dose enhancement as a function of Gd concentration in an ICRU sphere for three different data libraries.

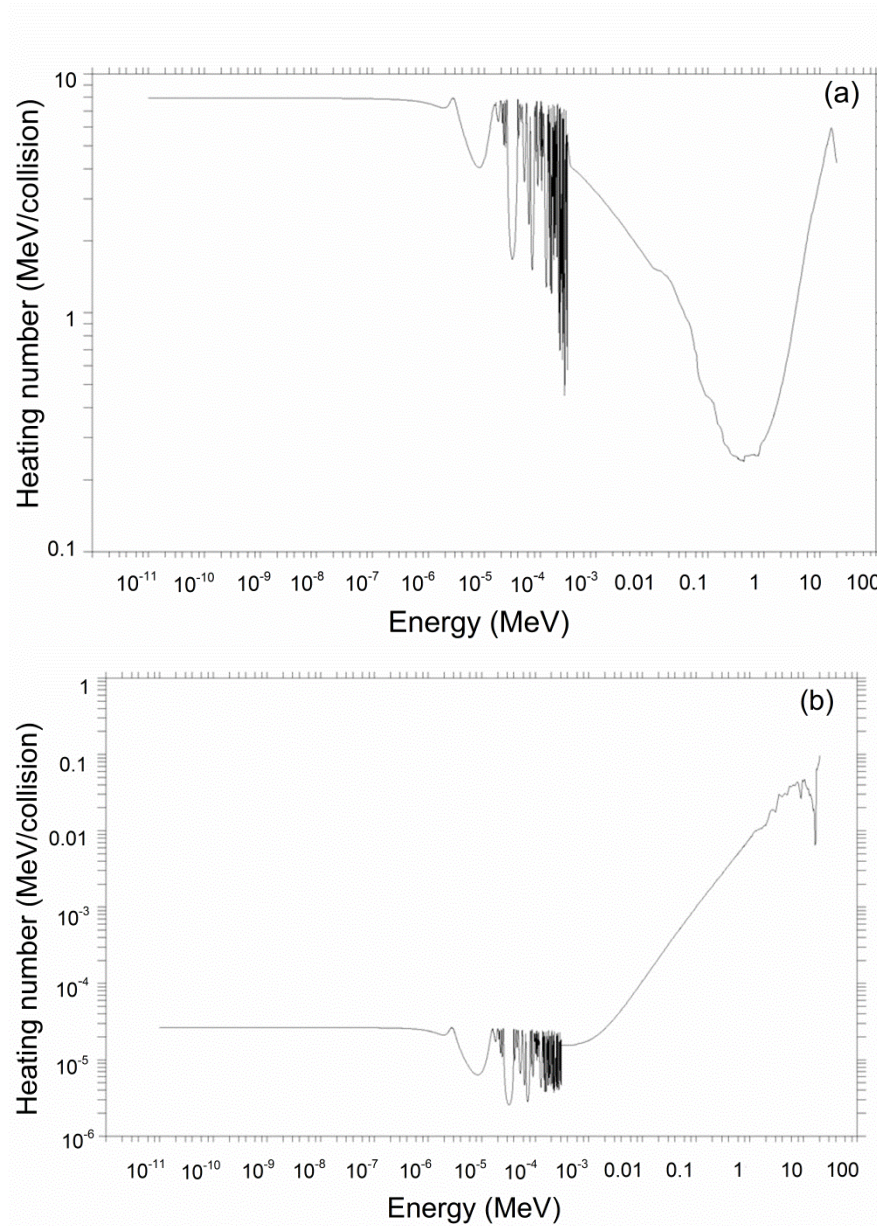


Figure 5.7. Comparison of the average heating numbers for ^{157}Gd from (a) ENDF-B-V.0 and (b) ENDF-B-VII.0. Images adapted from ‘Cross Section Plotting’ feature of MCNP Visual Editor.

The dose-enhancement as a function of Gd concentration for the photon contribution to the dose is shown in Figure 5.8. The photon absorbed dose rate when zero ppm of Gd is present in the ICRU sphere is $12\ \mu\text{Gy/hr}$, comparable to the neutron

absorbed dose rate, 15 $\mu\text{Gy/hr}$. It can be seen that the ENDF-B-V.0 and ENDF-B-VII.0 data sources produce the same photon dose-enhancement as a function of Gd concentration. This is expected as more Gd present will increase the number of Gd neutron captures increasing the number of prompt gamma rays produced, and hence photon energy deposited, through subsequent photon interaction, especially in a large 30 cm diameter sphere. The ENDF-VI.0 data source contains no photon production data, and therefore what is observed is a decrease in photon dose as a function a Gd concentration due to neutron self-shielding and fluence depression phenomena.

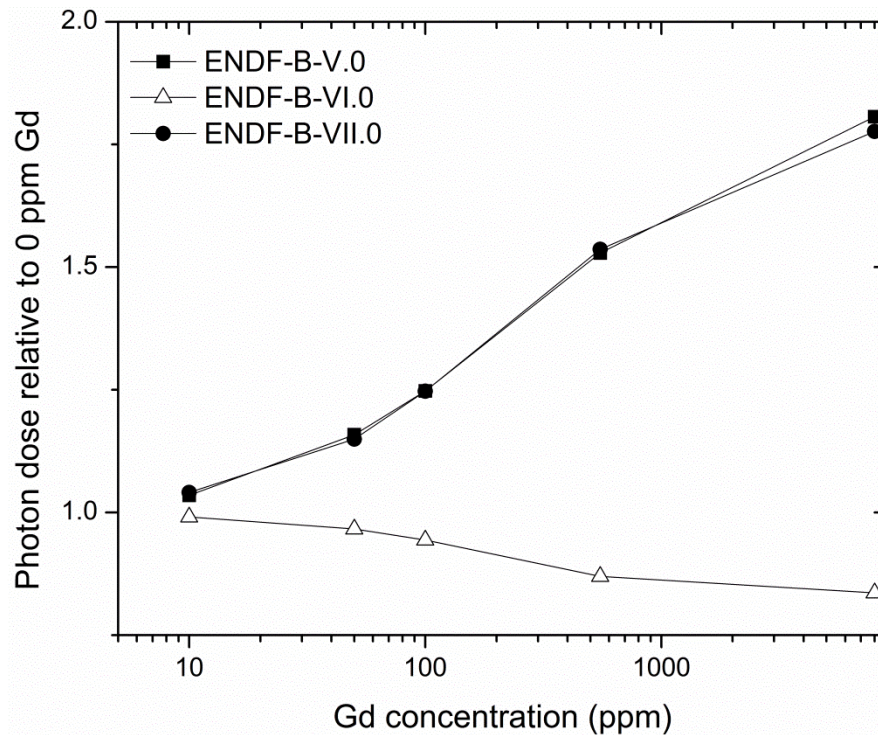


Figure 5.8. Photon dose enhancement as a function of Gd concentration in an ICRU sphere for three different data libraries.

5.3.2 Heating numbers: kerma approximation

In order to extract the heating numbers, $H(E)$, from MCNP a simple simulation was created. A void sphere with a radius of 1 cm was created, and a point source of neutrons with equal energy distribution in the same energy bins as the ENDF-VII.0 (Chadwick et al. 2006) nuclear cross section data (for comparison below) was placed in the center. In this case, it would be more convenient to have the kerma coefficient (Chadwick et al. 1999) in Gy cm^2 rather than the heating number (MeV/collision). The kerma coefficients are determined by the ratio of the FM4 heating tally (Gy) to F4 neutron fluence (cm^{-2}). The FM4 heating tally multiplies the reaction rate as a function of energy in a cell by the appropriate heating number to give energy deposited in MeV . The FM4 heating tally permits (for convenience) that the tally cell need not be filled with any material. This permits uniform fluence in the cell without any neutron interaction. This avoids significant self-shielding and fluence depression that is typical in high neutron absorbing materials such as Gd. The kerma coefficient per energy bin, i , in Gy cm^2 , determined from the MCNP output is:

$$k_{fi} = C \frac{\iint H(E)_i \sigma(E)_i \varphi(E)_i dE_i dV}{\varphi(E)_i} = C \frac{K(E)_i}{\varphi(E)_i}$$

The quantity $C = 9.64853 \times 10^{-11}/M$, where M is the molar mass of the material, converts the MCNP FM4 tally output $K(E)$ from $\text{MeV b cm}^{-2}/\text{atom}$ into Gy (J/Kg) (the cross sections in MCNP are in barns), $\sigma(E)$ is the neutron cross section, and $\varphi(E)$ is the neutron fluence (n/cm^2) at neutron energy E . Together the quantity $CK(E)$ is the kerma dose in Gy at neutron energy E . The energy bins from the cross section data ENDF-B-VII were used to bin the kerma and neutron fluence. The kerma coefficients from MCNP determined by this method are shown in Figure 5.9. The kerma coefficient data from ENDF-B-V.0 are significantly larger than that of ENDF-B-VII.0. In order to determine

the correct kerma coefficients for ^{157}Gd they were also derived based on reaction kinematics in the following section.

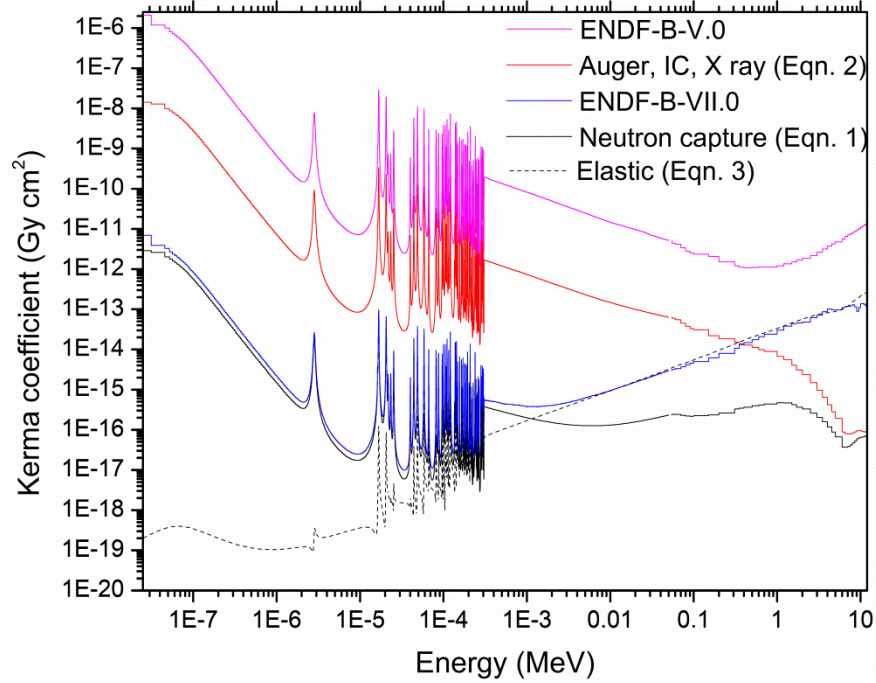


Figure 5.9. ^{157}Gd kerma components determined from available libraries in MCNP and derived based on kinematics. See text below for the kerma coefficients from equations 1-3.

5.3.3 Kerma coefficients based on kinematics

The kerma coefficients can also be derived based on the kinematics of the neutron interactions with the medium of interest. The neutron kerma for the $^{157}\text{Gd}(n,\gamma)$ reaction includes nuclear recoil from capture as well as elastic scattering, and the local energy deposition from IC/Auger electrons, and low energy X rays. The nuclear recoil from neutron capture comes from the energy imparted by the incident neutron and the recoil from γ -ray emission (Caswell, Coyne & Randolph 1980):

$$K_R = C \left[\frac{m_n E_n}{m_t + m_n} + \frac{\langle E_{\gamma i} \rangle^2}{2m_R c^2} \right] \sigma(n, \gamma) \quad 1$$

where m_t , m_n , and m_R are the atomic mass of the target, neutron, and recoil nucleus in units of u, E_n is the incident neutron kinetic energy in MeV, and $\langle E_{\gamma i} \rangle^2$ is the square of the i th γ -ray energy emitted per (n, γ) reaction with cross section $\sigma(n, \gamma)$ in b.

The local energy deposition from charged particle (IC/Auger electrons) and low energy X ray kerma is calculated as:

$$K_{ACX} = C \overline{E_{ACX}} \sigma(n, \gamma) \quad 2$$

where $\overline{E_{ACX}}$ is the sum of the average locally deposited energy from IC/Auger electrons, and low energy X rays.

The other important component of the neutron kerma for ^{157}Gd at energies greater than a few hundred eV is elastic scattering. The average kinetic energy transferred to the recoil nucleus for elastic scattering can be solved by simple kinematics applying both conservation of energy and momentum:

$$K_{el} = C \left(2E_n \left[\frac{m_n M}{(m_n + M)^2} \right] \right) \sigma_{el} \quad 3$$

where σ_{el} is the elastic scattering cross section. The total neutron kerma for ^{157}Gd is the sum of equations 1-3 above.

The derived kerma components are shown in Figure 5.9 above. The derived kerma components from recoil (Equations 1 and 3) appear to match quite well with the kerma from ENDF-VII.0 in terms of order of magnitude. The main discrepancy is due to the gamma ray energy used to calculate the nuclear recoil in Equation 1. The gamma ray energy used to calculate the neutron capture kerma in Figure 5.9 was the average gamma ray energy per neutron capture, 2.346 MeV. Since the decay of $^{158}\text{Gd}^*$ is a complex cascade of prompt gamma rays, it was much simpler to calculate the recoil based on the

average value. For energies below 500 eV (before elastic scattering is important) the ratio of MCNP to derived value ranged from 1.2 to 8 with an average ratio of 1.7 ± 0.7 . If, for example, 3 MeV is used as the photon energy to calculate the recoil the average ratio reduces to 1.0 ± 0.4 .

The Gd photon production data from the ENDF-B-V.0 and ENDF-B-VII.0 libraries are shown in Table 5.7. The photon production data from both libraries are a continuous spectrum with energies ranging up to the 7.94 MeV (Q -value the reaction). The average photon energy emitted per neutron capture is given in Table 5.7, along with the amount of energy emitted per source neutron. The remaining energy (Q -value minus E per SN) from the excited $^{158}\text{Gd}^*$ nucleus is the energy not given to photons and therefore not taken into account in the dose deposition. From Figure 5.9 we can see that this is the case for the ENDF-B-VII.0 as the derived kerma from IC/Auger electron, and X-ray emission is larger than the ENDF-B-VII.0 kerma. The ENDF-B-V.0 gives all the Q -value to gamma emission, there is remaining energy of about 80 keV not transported in the ENDF-B-VII.0 data. This energy can be attributed to IC and Auger electrons, and low energy X rays. This is comparable to the computed value of 60 keV given to IC and Auger electrons, and low energy X rays from Stepanek (2003). The average energy for IC electrons given in Miller et al. (1993) and used in calculations by Gierga et al. (2000) was 91 keV. The energy used in Equation 2 and plotted in Figure 5.9 was 91 keV to be conservative. Therefore the IC/Auger electron, and low energy X ray dose is not included in the heating numbers in MCNP. The dose from these emissions can easily be calculated using the kerma coefficients in Figure 5.9 above or by simply determining the number of neutron captures occurring in a specific volume and multiplying that result by the average energy and dividing by the mass to get the dose in Gy.

Table 5.7. Photon production data from two libraries available in MCNP5.

Library (ZAID)	Weight per SN	Energy (MeV) per SN	Average photon energy (MeV)	Remaining from Q -value (keV)
64157.55c	4.19	7.94	1.894	< 1
64157.70c	3.35	7.86	2.346	80

SN, source neutron.

It appears that the new ENDF-B-VII.0 heating data are correct for calculating the kerma due to nuclear recoil (however it does not include the IC/Auger electron, and low energy X ray kerma) and that the energy released per neutron capture with Gd in the ENDF-B-V.0 data was simply the reaction Q -value. This can be shown by inserting 7.94 MeV as the average locally deposited energy in Equation 2. The results are plotted in Figure 5.10. (The discrepancies at greater than a few MeV are due to the fact that the elastic scattering kerma has not been included in this figure.) Assuming local energy deposition of the full Q -value would be correct for a reaction such as $^{10}\text{B}(n, \alpha)^7\text{Li}$ which results in local energy deposition of two heavy charged particles, but for the (n, γ) reaction on Gd this is completely incorrect because ~99% of the Q -value is carried away by penetrating photon radiation (Miller et al. 1993, Sakurai, Kobayashi 2002). The deposition of energy for this radiation type depends on the volume, density, and composition of the material they traverse. The average photon energy from the neutron capture reaction with ^{157}Gd is about 2.35 MeV (depending on the data source). The mean free path of photons in tissue with this energy is greater than 20 cm. Therefore, on average, much of the photon radiation from Gd neutron capture will escape the participant or target volume. The photon dose from Gd neutron capture is computed separately from the neutron dose in MCNP by transporting the capture gamma rays from the site of interaction and tallying their dose deposition.

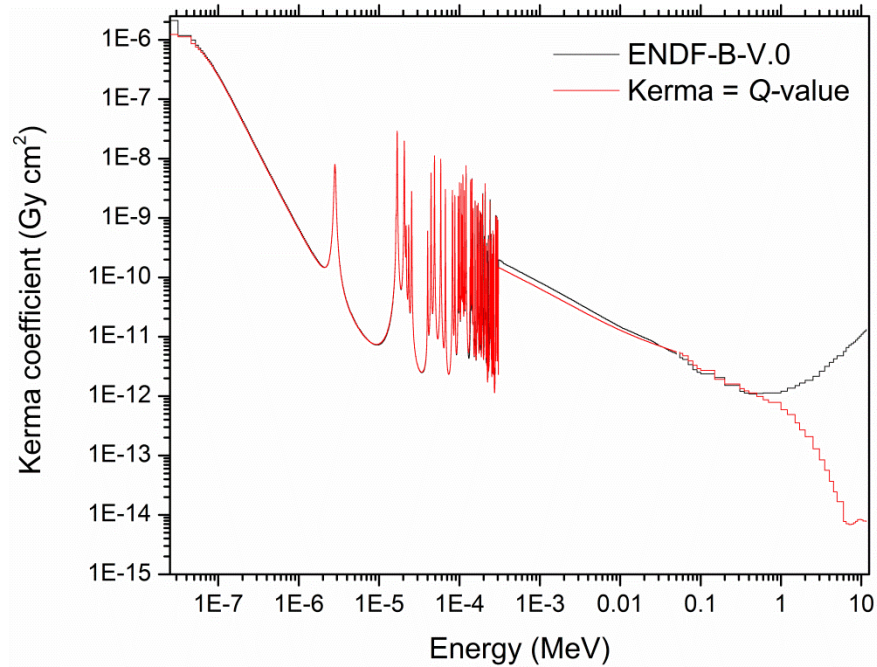


Figure 5.10. The kerma calculated from the local deposition of the full Q -value from the $^{157}\text{Gd}(n,\gamma)$ reaction and compared with the ENDF-B-V.0 data.

5.3.4 Hydrogen benchmark calculation

In order to confirm the above method, a benchmarking calculation was performed with hydrogen, the simplest nucleus for which to calculate the kinematic neutron kerma. Inelastic scattering between a neutron and the hydrogen nucleus is not possible because the proton does not possess any nuclear excited states. Therefore, the neutron kerma in hydrogen consists of nuclear recoil from neutron capture and subsequent emission of a single 2.223 MeV gamma-ray from the excited $^2\text{H}^*$ nucleus, as well as (proton) recoil from elastic scattering. The former interaction is significant at low neutron energies with the main contribution being recoil from gamma emission. As the neutron energy increases, the recoil energy increases from capture (the first term in Equation 1) but this becomes insignificant in the contribution to the neutron kerma because the cross section

drops off as a function of $1/v$. Elastic scattering interactions become the significant contribution to the neutron kerma on hydrogen for neutron energies above a few eV.

A comparison of the kerma coefficients determined from kinematics and those from the MCNP data libraries is shown in Figure 5.11. The derived components appear to match well with the kerma coefficients developed by Chadwick et al. (1999). The ENDF-VI.0 data appear to follow mostly the same trend, with some discrepancies, especially for thermal neutrons. Oddly, the newest data set, ENDF-B-VII.0, appears to not include the recoil kerma from gamma ray emission. This is a significant discrepancy and ^1H is not flagged as having any energy balance issues on the T-2 Nuclear Information Service website (MacFarlane 2007). The kerma coefficients for some of the available cross-section libraries for ^1H were determined and the results are summarized in Table 5.8. It appears that the data libraries for ENDF-B-V and ENDF-B-VII do not contain the recoil heating from neutron capture, while the remaining data-sets contain both the heating from recoil and elastic scatter.

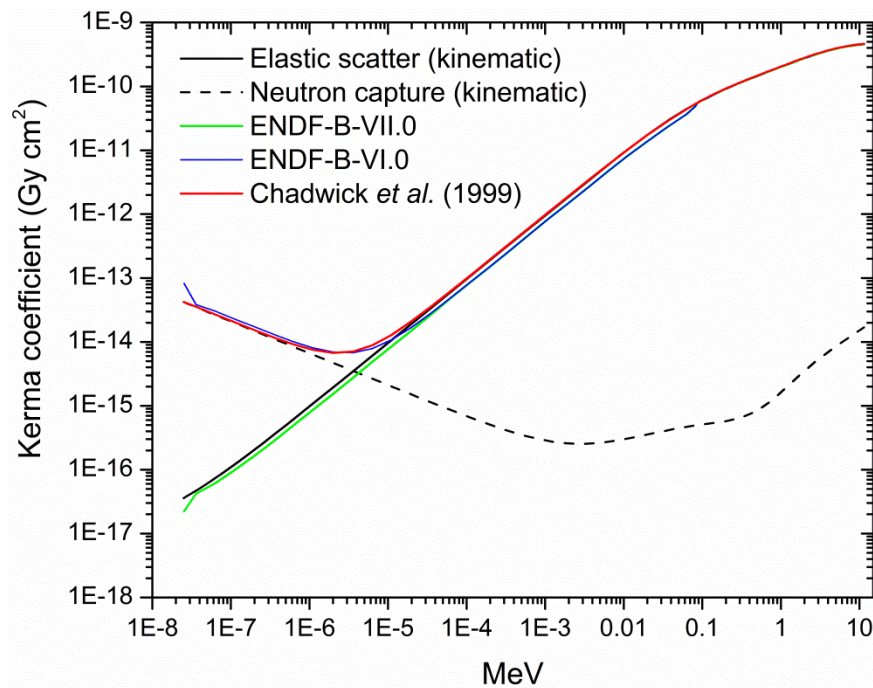


Figure 5.11. Comparison of the kinematic neutron kerma coefficients in ^1H and those available in two MCNP data libraries.

Table 5.8. Summary of the neutron heating data from the available cross-section libraries for ^1H in MCNP.

Library (ZAID)	Source	Evaluation Date	Includes recoil heating
1001.24c	B-VI.6	1998	YES
1001.42c	LLNL	<1992	YES
1001.50c	B-V.0	1977	NO
1001.53c	B-V.0	1977	YES
1001.60c	B-VI.1	1989	YES
1001.62c	B-VI.8	1998	YES
1001.66c	B-VI.6:X	1998	YES
1001.70c	B-VII.0:x	2005	NO

From Appendix G- MCNP data libraries
 LLNL, Lawrence Livermore National Laboratory

In this example calculation the kerma coefficients were derived based on kinematics and compared with the available datasets in MCNP. There were some discrepancies observed. From my findings, I therefore strongly encourage other researchers carefully to evaluate the available nuclear data themselves and determine the suitability of use for their specific purpose.

5.4 Gadolinium dose enhancement: phantom dosimetry

For the $^{157}\text{Gd}(n,\gamma)$ neutron capture reaction, it has been discovered above that we need to consider the dose contributions from two components that can be separated as (1) prompt gamma rays, and (2) IC and Auger electrons, and low energy X rays. The calculation of the dose rate to a specific organ or tissue from IC/Auger electrons and low energy X rays is determined in MCNP by using the FM4 tally multiplier and can be described by the following equation:

$$D = n f C_d \frac{\bar{E} \iint \varphi(\vec{r}, E) \sigma(E) dE dV}{m}$$

where n is the neutron emission rate, f is a conversion factor converting $\text{MeV b kg}^{-1} \text{ cm}^{-2}$ into J/kg (Gy) , C_d is the number density of ^{157}Gd in the tissue volume, \bar{E} is the average locally deposited energy from IC/Auger electrons, and low energy X rays, in this case conservatively assumed to be 0.091 MeV (Miller et al. 1993), m is the tissue or organ mass in kg, $\varphi(\vec{r}, E)$ is the neutron fluence spectrum, and $\sigma(E)$ is the (n, γ) cross section for ^{157}Gd . In MCNP, the cross sections are given in barns and that is why the f conversion factor is required. The equivalent dose for the IC/Auger electrons, and low energy X rays was found by multiplying the absorbed dose by a radiation weighting factor of 1. For Auger electrons, the w_R can be significantly higher if the Auger emitter is located in close proximity to the cellular DNA (ICRP 2007). There was no assumed increase in biological effectiveness from the Auger electrons in this instance because it was assumed that there was no significant cellular uptake. The prompt gamma ray dose enhancement is determined in MCNP simply by adding the appropriate concentration of Gd to the tissue and measuring the increased dose due to the increased photon production from neutron capture in Gd. This calculation was performed using the models described above for the leg muscle, kidney, and liver irradiation geometries. To the best of this author's knowledge the highest concentration measured in patients with NSF was less than 500 ppm (Swaminathan et al. 2008), therefore to be conservative the concentration of Gd in the target organs was assumed to be 550 ppm. This value was arbitrarily chosen and should provide a conservative upper bound on the potential dose enhancement from a measurement of Gd retention after exposure to a Gd-based MRI contrast agent.

The neutron kerma coefficients for soft tissue (ICRU 4 component; 76.2 % oxygen, 2.60% N, 10.1% H, and 11.1% C by weight) are shown in Figure 5.12. If we assume 550 ppm Gd in the soft tissue then the concentration of ^{157}Gd would be 86 ppm (natural abundance 15.65%). The kerma coefficients for IC/Auger electrons and low energy X rays for 86 ppm ^{157}Gd are also shown in Figure 5.12. Also given in Figure 5.12 are the soft tissue kerma coefficients weighted with the ICRP103 neutron radiation

weighting factors. This can be called the “equivalent dose” coefficient. The IC/Auger electron and low energy X ray kerma coefficients are larger than the soft tissue neutron kerma coefficients from thermal energies up to approximately 0.15 eV. Considering, for example, the kerma coefficients for a purely thermal neutron fluence in tissue with 550 ppm Gd present the absorbed dose-enhancement would be 6.8, and the equivalent dose enhancement would be 3.3. This difference between the absorbed dose enhancement and the equivalent dose enhancement is due to the radiation weighting factor of 2.5 for thermal neutrons and 1 for IC/Auger electrons and low energy X rays. This dose-enhancement would be significant for an optimized low energy neutron beam as would be considered for radiation therapy applications. However, the majority of the dose from the $^{238}\text{Pu}/\text{Be}$ source is from high energy neutrons so the dose enhancement is not expected to be significant for this measurement system. This is discussed in the following sections.

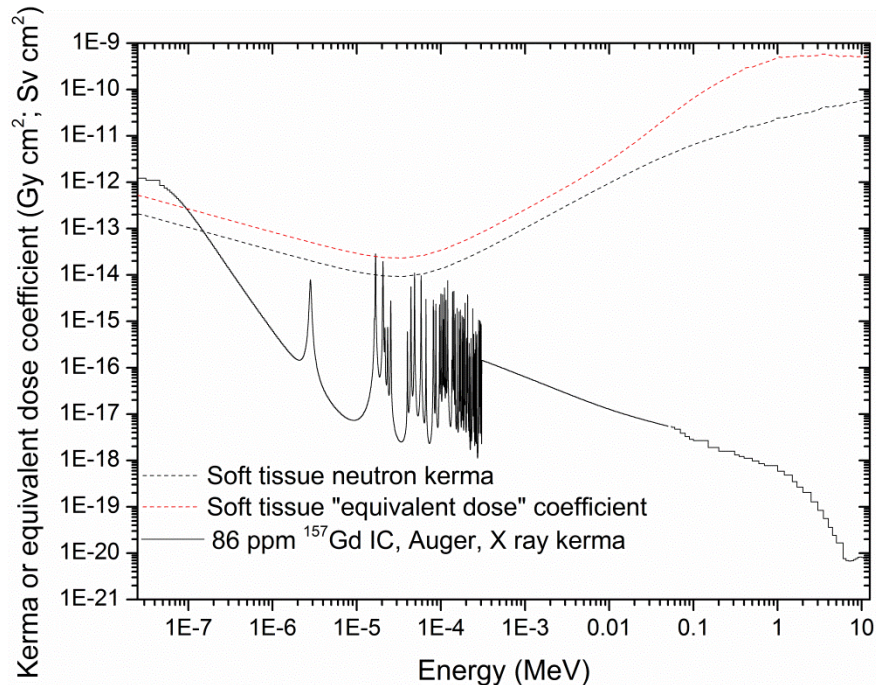


Figure 5.12. Comparison of the neutron kerma in soft tissue with the IC/Auger electron and low energy X ray kerma from 550 ppm Gd. The neutron soft tissue kerma is from Chadwick et al (1999). Also shown is the “equivalent dose” coefficient which is the neutron soft tissue kerma weighted with the ICRP103 neutron radiation weighting factors.

5.4.1 Dose enhancement: leg irradiation

A pilot study measuring the concentration of Gd in the leg muscle tissues at pre-determined times after injection of a Gd-based contrast agent was conducted and is described in Chapter 6. After injection, the Gd-based contrast agents are rapidly distributed to the extracellular/extra-vascular spaces. To model the dose-enhancement, the Gd concentration of 550 ppm was assumed to be evenly distributed in the soft-tissue of the leg in the ORNL phantom and this soft tissue was assumed to be composed entirely of muscle. The photon equivalent dose-enhancement is shown in Table 5.9. This is the ratio of the dose with 550 ppm in the leg soft tissue to the dose with zero Gd in the leg soft tissue. In other words this is the increase in dose due to the presence of Gd in tissue compared to dose to the tissue without Gd present. The dose to tissue without Gd present is from photons produced through neutron interactions in the collimating and shielding apparatus and in the tissue itself. The soft tissue and tibia receive the highest enhancement, this is because the concentration of Gd is present in the soft tissue and capture photons produced in the surrounding soft-tissue will irradiate the tibia. The IC/Auger and low energy X ray dose was minimal at 0.2 $\mu\text{Sv/hr}$, this is less than 2% of the photon dose to the soft tissue, which in turn is less than 10% of the total equivalent dose. Overall, there was no significant increase in the effective dose. This is because the photon contribution to the equivalent dose is less than 10%. The reason no significant enhancement is seen from the IC/Auger and low energy X ray components is because the dose from thermal neutrons is relatively small compared to the dose from the fast neutron component of the fluence from the $^{238}\text{Pu}/\text{Be}$ source in tissue, and therefore any enhancement from thermal neutron capture in ^{157}Gd is found to be minimal for this system. Therefore the measurement of the retention of Gd in the muscle is a procedure with minimal radiation exposure with no significant enhancement to the effective dose from the presence of Gd in the muscle tissues.

Table 5.9. The photon equivalent dose-enhancement from 550 ppm Gd in the leg soft tissue. The table shows the ratio of the dose with 550 ppm in the leg soft tissue to the dose with zero Gd in the leg soft tissue.

ORNL phantom tissue	Ratio
Leg soft tissue	1.27
Femur	1.12
Tibia	1.37
Leg skin	1.21

5.4.2 Dose enhancement: kidney irradiation

The photon dose-enhancement for 550 ppm Gd in the kidneys is shown in Table 5.10. The photon dose to both the kidneys is significantly increased by a factor of 1.49. The only other organ receiving a significant enhancement on the order of 10% is the spleen. The photon equivalent dose to the left kidney increased by a factor of 1.64 to 61.9 $\mu\text{Sv/hr}$. The IC/Auger electrons, and low energy X ray dose was found to be 4.94 $\mu\text{Sv/hr}$. This is about a 7% contribution to the dose enhancement from the $^{157}\text{Gd}(n,\gamma)$ reaction products. However, since the photon contribution to the total dose is small (10% level) there was no significant observed change in the effective dose when 550 ppm of Gd is present in the kidneys.

Table 5.10. The photon equivalent dose-enhancement from 550 ppm Gd in the kidneys. The table shows the ratio of the dose with 550 ppm in the kidneys to the dose with zero Gd in the kidneys.

Organ/Tissue	Ratio
^a Bone	1.03, 1.06
Colon	1.04
Lung	1.03
Stomach	1.05
Bladder	1.02
Oesophagus	1.03
Liver	1.04
Brain	1.00
Skin	1.03
Adrenals	1.05
Gall bladder	1.05
Heart	1.03
Kidneys	1.49
Muscle	1.06
Pancreas	1.06
Small intestine	1.04
Spleen	1.10

^a Ribs and spine, respectively

5.4.3 Dose enhancement: liver irradiation

The photon dose-enhancement for 550 ppm Gd in the liver is shown in Table 5.11. The photon dose to the liver is significantly increased by a factor of 1.62. The liver is a large mass organ and therefore with a concentration of 550 ppm Gd there will be a significant number of neutron captures with Gd. For this reason, many of the other organs receive a photon dose enhancement at the 10% level or greater, as compared to the kidney

simulation described above. The IC/Auger electrons, and low energy X ray dose were found to be minimal: 1.3 $\mu\text{Sv/hr}$. Again, however, there was no significant change to the effective dose, no enhancement, when 550 ppm Gd is present in the liver.

Table 5.11. The photon equivalent dose-enhancement from 550 ppm Gd in the liver. The table shows the ratio of the dose with 550 ppm in the liver to the dose with zero Gd in the liver.

Organ/Tissue	Ratio
^a Bone	1.15, 1.13
Colon	1.11
Lung	1.16
Stomach	1.10
Bladder	1.06
Oesophagus	1.13
Liver	1.62
Brain	1.01
Skin	1.10
Adrenals	1.19
Gall bladder	1.31
Heart	1.12
Kidneys	1.18
Muscle	1.15
Pancreas	1.16
Small intestine	1.10
Spleen	1.09

^a Ribs and spine, respectively

5.5 Concluding remarks on dosimetry for the measurement of Gd using the $^{238}\text{Pu}/\text{Be}$ source-based system

The approach taken in this study of dosimetry was conservative as this is more important for this particular application than the detailed microscopic dosimetry which would be required for studies investigating Gd neutron capture therapy. The agents studied in this thesis remain extracellular so any Auger or nuclear Gd recoil dose enhancement providing direct DNA damage can be ignored. More detailed dosimetry would have to be performed when calculating dose distributions for clinical therapies, whereas for this case it was found that this is a low dose procedure, in the μSv -to- mSv dose range, and the macroscopic dosimetry performed here is sufficient for estimating participant radiation dose levels. As stated in the MCNP users' manual, users should be critical of the cross section data they choose for their computation. As I have described, the cross section data may not be entirely accurate for all purposes and I recommend that other users should carefully evaluate the libraries so that they are aware of any simplifications and the limitations of the data. I observed some discrepancies. I am not aware whether the MCNP user's community already know of some of these issues. I highlight them here as they deal with the important aspects of dosimetry for the purposes of this research. The effective dose rates calculated above for the leg muscle, kidney, and liver irradiation geometries are comparable to other clinical diagnostic tests, and therefore I suggest the dose levels for the measurement of Gd retention with the $^{238}\text{Pu}/\text{Be}$ source-based system are acceptable for research studies. The main reason no significant dose-enhancement was found here is because the dose from thermal neutrons is small and the enhancement from the local energy deposition of IC/Auger and low energy electrons from thermal neutron capture on ^{157}Gd was found not to increase the dose significantly. If an optimized low energy neutron beam similar to the ones proposed for Gd NCT was used then a significant dose-enhancement from IC/Auger and low energy electrons would be expected. This is because the dose per neutron would be much more significant for a lower energy neutron beam where capture in Gd would be dominant. However, the main

contribution to dose from the $^{238}\text{Pu}/\text{Be}$ source is from the high energy neutrons (> 0.01 MeV) and therefore the thermal neutron capture component is not a significant contributor to dose for this source-based system. The high energy neutrons do not contribute to measurement sensitivity and only contribute to dose. This is a limitation that is difficult to avoid when using the $^{238}\text{Pu}/\text{Be}$ source for *in vivo* neutron activation analysis, which has a broad neutron energy spectrum up to 11 MeV.

Chapter 6

Gadolinium detection via *in vivo* prompt gamma neutron activation analysis following gadolinium-based contrast agent injection: a pilot study in 10 human participants (Article IV)

6.1 Introduction to Article IV

It was decided, based on the initial phantom-based feasibility studies and the calculated low radiation dose that the measurement system was at a suitable stage of development for a small pilot study to be performed. The pilot study was performed on 10 healthy individuals. They were injected with a Gd-based MRI contrast agent: the chosen contrast agent was one of the safest on the market, and therefore the risk from contrast agent exposure was minimal. The target tissue was the lower leg muscle which contains tissues with low radiation sensitivity. The effective radiation dose for a single neutron exposure was low: 0.6 μ Sv. The results of this study are described in Article IV.

Full approval was obtained from the McMaster University/St. Joseph's Healthcare Human Research Ethics Boards and McMaster University Health Physics. The Canadian Nuclear Safety Commission (CNSC) approved the study protocol. This study was performed to validate the fact that our measurement system could measure Gd in the lower leg of participants after the type of Gd-based contrast agent administration that is now routinely performed in magnetic resonance imaging (MRI). This low risk study was performed to determine if it would be possible to detect gadolinium in muscle tissue at two pre-determined times after contrast agent injection. A base-line measurement was performed before contrast agent injection. Two post injection time points permitted a) validation of Gd measurement and b) verification of the clearance of Gd after injection. Data from the study were to be used to determine the feasibility of using this Gd detection system for future larger enrollment studies of Gd retention.

The following article presents the results of this study prepared in manuscript form for subsequent submission to a peer reviewed journal for publication. The *in vivo* work was organized and performed by the author of this thesis under the supervision of Dr. Fiona McNeill. The manuscript was prepared by the author of this thesis and edited by Drs. Fiona McNeill, and David Chettle. Dr. Michael Noseworthy secured resources at the Imaging Research Centre (IRC) and set-up the MR imaging protocol.

6.2 Contents of Article IV

J.L. Gräfe¹, F.E. McNeill¹, M.D. Noseworthy^{1,2}, D.R. Chettle¹

¹Department of Medical Physics and Applied Radiation Sciences, McMaster University, Hamilton, Ontario, Canada L8S-4K1

²Department of Biomedical Engineering, McMaster University, Hamilton, Ontario, Canada L8S-4K1

Abstract

Gadolinium (Gd) based contrast agents are routinely used as part of many magnetic resonance imaging (MRI) procedures. The widespread use of these agents, and concerns about Gd toxicity, motivated us to develop a monitoring procedure that could non-invasively measure quantitatively potential retention of toxic free Gd in tissues after use of the agent. We have been developing a method to measure Gd painlessly and non-invasively by prompt gamma neutron activation analysis. In this paper we present the results of a pilot study where we show that we can measure Gd, quantitatively *in vivo*, in the lower leg muscle of 10 participants. A series of three neutron leg scans were performed. The effective radiation dose for a single neutron leg scan was very low, 0.6 μ Sv, so multiple scans were possible. Calibration phantom and *in vivo* detection limits were determined to be identical: 0.58 ppm. Gadolinium was not detectable in muscle prior to exposure to the contrast agent Gadovist[®]. Gadolinium was detected, at greater

than 99% confidence, in 9 participants within 1 hour of contrast administration, and in 1 participant approximately 3.3 hours post-contrast administration. The measured concentrations of Gd ranged from 2.0 to 17.3 ppm (6.9 to 56 uncertainties different from zero). No detectable Gd was measured in any participant in the third neutron scan (conducted 0.7 to 5.9 days post-contrast). The results of this study validate our new measurement technology. This technique could be used as a non-invasive monitoring procedure for exposure and retention of Gd from Gd-based chelates used in MRI.

Keywords: *in vivo* neutron activation analysis; gadolinium; prompt gamma rays; characteristic X rays; gadolinium-based MRI contrast agent; non-invasive monitoring procedure.

1. Introduction

Gadolinium (Gd) is a rare earth element that is routinely used as a contrast agent in MRI. The Gd^{3+} ion interacts strongly with the main magnetic field shortening the tissue relaxation times (T1 and T2), and enhances the ability for diagnosis of a variety of clinical diseases. Exposure to gadolinium-based contrast agents (GBCA) has been a concern in patients with advanced renal failure ever since the first correlation between GBCA and nephrogenic systemic fibrosis was discovered in patients with renal disease (Grobner 2006, Grobner, Prischl 2007). There is also a concern regarding retention of Gd in the general patient population because Gd has been found in bone-biopsy samples post administration obtained from people under-going hip replacement surgery (White, Gibby & Tweedle 2006, Darrah et al. 2009).

We have developed a new method to measure gadolinium in the kidney, liver, and muscle painlessly and non-invasively in humans by prompt gamma neutron activation analysis (PGNAA) (Gräfe et al. 2010, Gräfe et al. 2011). PGNAA is a non-invasive analytical technique in which a beam of neutrons is used to probe matter, or in this case the tissue of a living subject. For the measurement of Gd using the radioisotope-based PGNAA facility at McMaster University, a neutron beam from an isotopic $^{238}\text{Pu}/\text{Be}$ source is used to probe the tissue to look for gamma and X rays produced as a result of

the $^{155}\text{Gd}(n,\gamma)$ and $^{157}\text{Gd}(n,\gamma)$ neutron capture reactions. These reactions have extremely high neutron capture cross sections of 60 900 and 254 000 barns, respectively, and thus have a high probability of occurring when gadolinium is irradiated with thermal neutrons. The reactions result in the production of the compound excited state nuclei $^{156}\text{Gd}^*$ and $^{158}\text{Gd}^*$, which decay by prompt gamma ray emission to the stable ^{156}Gd and ^{158}Gd isotopes, respectively. A quantitative estimate of Gd is derived from the intensity of the reaction prompt gamma rays, and also characteristic Gd X rays emitted as a result of internal conversion electron emission (Gräfe et al. 2012). These photon emissions are measured on a Hyper-Pure Germanium (HPGe) semiconductor detector and the signals from measurement subjects are compared to those from calibration standards to derive a concentration estimate.

The purpose of this research study is to test the new method on healthy volunteers who have received a GBCA. This study was performed to validate the ability of the technology to detect gadolinium and permit predictions to be made of the feasibility of the system to be applied in larger enrollment studies of gadolinium retention or Gd uptake and distribution in other susceptible and more radiosensitive organs such as the kidney and liver. This study also determined if there was any significant long-term, that is, more than 24 hour, retention of Gd in the muscle tissues.

Ten healthy volunteers of both sexes were recruited into this study. The GBCA used in this study was Gadovist[®] (Gadobutrol, Bayer Inc.), a non-ionic, macro-cyclic agent, with a concentration of 1 mmol/mL. The doses administered in this study were clinically relevant doses ranging from 0.1-0.2 mmol per kg of body weight. This particular contrast agent has a well demonstrated and well documented safety profile in greater than 5.7 million subjects (Voth, Rosenberg & Breuer 2011). The risk from contrast agent exposure in this healthy volunteer study was very low. In addition, the lower leg muscle is an area located away from the radiosensitive organs and tissues of the body and therefore the effective radiation dose was low, 0.6 μSv , for a single leg muscle neutron scan. To put this in perspective, the annual natural background radiation exposure level in North America is approximately 3000 μSv . The radiation dose sustained in the

study, for each scan, was approximately equal to the dose from two hours of natural background.

2. Methods

2.1 Study population

Approval was granted by the Hamilton Health Sciences/St. Joseph's Healthcare Hamilton Human Research Ethics Boards to conduct a study on ten healthy volunteers. A total of five female and five male participants, ages 23 to 62, were recruited. The participant demographics are given in Table 1. Each participant was briefed on the risks of both procedures and signed a consent form prior to study commencement. Every participant was carefully screened for MRI suitability including contrast exposure. Pregnant females were excluded from participation in the study. None of the participants reported suffering from kidney disease, peripheral vascular disease, or poor circulation. None of the participants reported previous exposure to a GBCA. Although anatomical data are available from the MRI scan the leg circumference was also physically measured to provide additional data on the participant's leg size at the neutron beam height.

Table 1. Participant demographics.

Participant #	Sex	Age	Weight (kg)	Leg circumference (cm)	Contrast agent dose (mL; ^a mL/kg)
1	F	46	75	40	(15; 0.2)
2	M	26	86	38	(10; 0.12)
3	F	45	68	40.5	(10; 0.15)
4	F	53	68	39	(6.8; 0.1)
5	M	23	68	37	(6.8; 0.1)
6	M	38	85	38.5	(8.5; 0.1)
7	M	50	100	43	(10; 0.1)
8	M	62	110	45	(11; 0.1)
9	F	27	59	33	(5.9; 0.1)
10	F	27	66	36.5	(6.6; 0.1)

^a mL per kg of body weight; equivalent to mmol/kg (Gadobutrol, 1 mmol/mL)

2.2 PGNA measurement system

A schematic drawing of the measurement system located at the Tandem Accelerator Building (TAB) at McMaster University is shown in Figure 1. The measurement system has been described in detail previously (Gräfe et al. 2010, Gräfe et al. 2011, Grinyer, Byun & Chettle 2005). Briefly, the system consists of two ²³⁸Pu/Be sources that are placed within a neutron shielding and collimating apparatus composed of steel, graphite, polyethylene, and borated resin. A modification to the original detection system is the addition of a second larger volume HPGe detector. The primary detector is a LO-AX model detector (10% relative efficiency, 51700/20-S, ORTEC), and the secondary detector is a larger volume GMX model detector (35% relative efficiency, 35195, ORTEC). Due to geometrical constraints (the detectors are mounted on large thermally-insulated liquid nitrogen dewars that cool the detectors to reduce electronic noise) the larger volume detector is placed in the less optimal position at an angle of 40° with respect to the LO-AX and 2 cm away from the phantoms. This particular detector

was chosen to be placed in the less optimal position in terms of detection solid angle because this is the poorer in terms of low energy resolution of the two detectors. The poor energy resolution of the GMX detector is most likely a result of previous neutron exposure and subsequent temperature cycling. Nevertheless this detector acts as a back-up, and as means of verifying the results seen on the primary LO-AX detector.

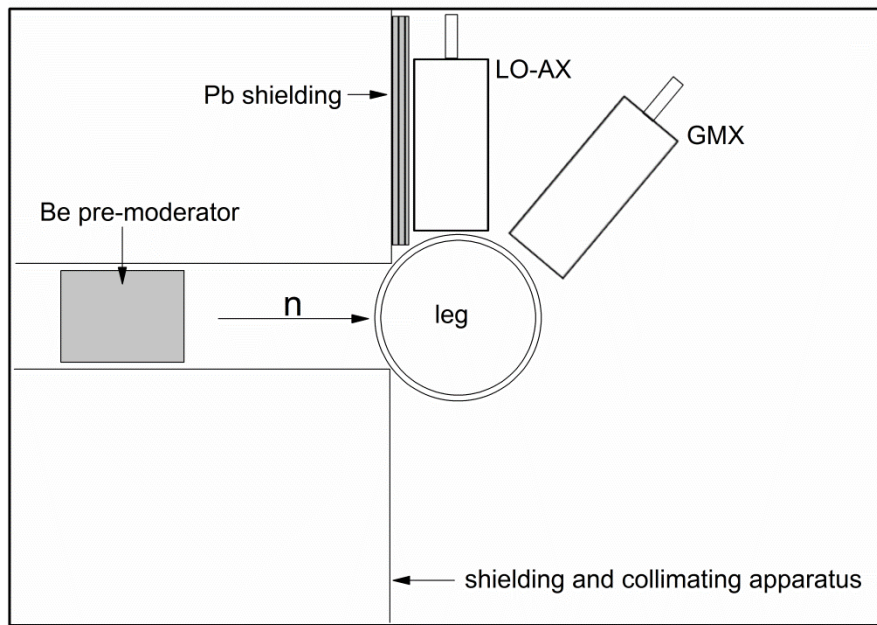


Figure 1. Schematic diagram of the measurement system for Gd in the lower leg muscle.

2.2.1 Phantom measurements

Aqueous 2 L phantoms are used to simulate the lower leg muscle. These phantoms were prepared (using standard-addition methods) to contain 0-151 ppm of Gd (Gräfe et al. 2011). Phantom measurements were interspersed amongst participant measurements to monitor the system stability and to provide valid calibration data for all participants. The phantoms between 0-25 ppm Gd were measured a minimum of 10 times each to improve the calibration line precision in this low concentration range, as it was anticipated that subject measurements would be of the order of this concentration. The higher concentration phantoms were measured 3 times each to monitor peak stability (position),

energy resolution, and to validate the fitting functions using peaks with high numbers of counts. The peak fitting functions and data analysis are described fully in Refs. (Gräfe et al. 2011, Gräfe et al. 2012). The phantom minimum detectable limit, M_{DL} , by convention in our laboratory, is defined as twice the uncertainty in the zero concentration phantom measurement. The M_{DL} is the result of the propagation of uncertainties in the calibration line parameters and zero concentration phantom peak area measurement.

2.2.2 Human neutron leg muscle scan

Participants in this study were asked to have three neutron scans of their lower left leg muscle. The timeline for the neutron scans was: (A) prior to contrast agent administration, (B) within 1 hour after contrast agent administration, and (C) within 1 week after contrast agent administration. The purpose of the first scan was to determine the baseline Gd content. The second scan was to assess and validate our system when Gd is known to be present, and the third scan was to determine if there was any significant retention. The muscle is scanned by a non-invasive analytical technique called neutron activation analysis. With this method the muscle is exposed to a beam of neutrons. The scan looks for signals from neutron capture reactions which result in the emission of a specific signature of gadolinium prompt gamma rays and characteristic X rays. The number of gadolinium gamma rays and X rays is proportional to the amount of Gd present in tissue. The radiation dose for this measurement was determined by Monte-Carlo simulation using our well benchmarked model (Gräfe et al. 2010, Gräfe et al. 2012) combined with the Oak Ridge National Laboratory mathematical computer model of an adult human (Eckerman, Cristy & Ryman 1996, Krstić, Nikezić 2007). The effective radiation dose for a single leg muscle neutron measurement was 0.6 μ Sv. The validity of this radiation dose simulation was determined by comparison of the Monte-Carlo results with experimental survey measurements. Excellent agreement was found between experiment and simulation and thus we place significant confidence in the dosimetry.

For the neutron irradiations, the participants' calf muscle was positioned at the center of the collimated neutron beam (9 cm diameter) and irradiated for approximately

35 minutes. A photograph of an *in vivo* measurement is shown in Figure 2. The participant stands in front of the irradiation facility and the lower leg muscle is centered in the collimated neutron beam, and aligned with the detectors. In the top left corner of Figure 2 a shelf is positioned so that the participant has something to lean on, as well as a rest for reading material to help the time pass quickly. The set-up proved to be successful and was able to accommodate all 10 participants, although, some participants did admit to minor discomfort from having to stand upright and still for the full 35 minutes, as well some reported a slight tingling in their toes from loss of circulation in this position. This irradiation box was initially designed to measure toxic elements in the kidney and liver and therefore was not entirely ergonomically correct for leg measurements. For future measurements, a more comfortable arrangement is obviously an area worth some further effort.

The LO-AX detector “dead time” was approximately 3.7% for each measurement and was set to acquire for a “live time” of 2000 s. (While the system processes a gamma-ray event, it cannot process a second incoming event, and is called “dead”. Live time is when the system is available to process events. Live time plus dead time equal clock or real time.) The GMX detector dead time was approximately 7.4% (higher because of a comparatively larger detector volume), and therefore was set for a live time of 1950 s, to make the real time measurements for the two detectors match. In both cases the real time did not exceed 2100 s (or 35 min), limiting the radiation exposure time to a maximum of 35 minutes for each measurement.



Figure 2. Photograph of a participant measurement. The participants' left leg is aligned with the collimated neutron beam, and the photons from neutron interactions in the tissue and surrounding materials are measured with two radiation detectors.

2.3 MRI

The MRI of each participant's lower leg was performed at the Imaging Research Centre (IRC) at St. Joseph's Health Care Hamilton. After the first neutron scan, which took place in the Tandem Accelerator Laboratory (TAB) on the McMaster University campus, the participant visited the IRC for the MRI scan. The scans were performed using a GE 3T Signa HD MRI system and a single channel quadrature birdcage transmit/receive extremity RF coil (GE Healthcare, Milwaukee, WI). Scanning was performed to mimic what is done clinically for quantitative contrast enhancement, including injection volume and rate. Following a 3-plane localizer a routine axial 3D T1-weighted spoiled gradient recalled echo (SPGR) anatomical scan was performed (TE/TR = minimum/5.6 ms, 18 cm field of view (FOV), 256×224 matrix, 2 mm thick, 0 mm skip, 31.25 kHz rBW). Subsequently a single slice dynamic contrast-enhanced MRI (dceMRI) scan was done through the slice with highest cross sectional area of the lower leg. Scanning parameters were: 2D axial SPGR, TE/TR=2.1/4.9 ms, flip angle = 25°, 244

kHz/pixel receiver bandwidth, 128×128 matrix, 5 mm thick, FOV = 18 cm. A total of 200 dynamic images were collected (temporal resolution = 0.63 s) during antecubital vein injection of MR contrast (Gadovist[®]), performed using a Spectris Solaris power injector (Medrad, Warrendale, PA, USA) using a 4 cc/second injection velocity and 20 gauge IV. Post contrast scanning, the 3D pre-contrast SPGR was repeated. The volume of contrast agent administered to each participant is shown in Table 1. The imaging scan protocol was developed using the first three participants. Therefore the doses administered to the first three subjects are different from the other participants who received a standard Gadovist[®] dose of 0.1 mL/kg (0.1 mmol/kg). The doses administered to the first three participants were still well within the recommended levels of clinical diagnostic doses (Voth, Rosenberg & Breuer 2011). The Gd injection time was recorded, and following the imaging protocol, the participant changed back into their street clothes and was subsequently transported to TAB on the McMaster University campus for their second neutron leg scan. The desired time for transport from the IRC to the TAB was within a one hour time-frame. This is less than the nominal half-life of approximately 1.5-2 hours for Gadovist[®]. This was successful for 9 out of 10 participants. For one participant access was restricted to the TAB due to a false fire alarm. The participant and researcher were not allowed to enter the TAB until authorization from the fire department was granted. Once the fire department declared the incident a false alarm, the participant was able to enter the TAB for their second neutron leg scan ~3.3 hours after contrast agent injection.

3 Results & discussion

3.1 Phantom calibration lines

The phantom detection limits from both detectors for the photon emission lines are shown in Table 2. The K_{β} X ray and 79.5 keV prompt gamma ray signal from the GMX detector were not used in the analysis of the *in vivo* data because they were previously determined to not improve the overall detection limit of the system. The total detection limit is determined by the inverse variance weighted method (Chamberlain et al. 2012a) to be 0.58 ppm. Using the two strongest photon emission lines, the GMX detector

only provides an 8% improvement in the detection limit, but nevertheless provides a further verification for the detection of Gd.

Table 2. Phantom detection limits for the Gd neutron capture photon emission lines from both HPGe detectors.

Transition	Photon Energy (keV)	M _{DL} (ppm)	
		LO-AX	GMX
K _α X ray	42.309, 42.996	0.91	2.30
K _β X ray	48.7, 50	4.26	^a 10.9
¹⁵⁷ Gd(n,γ) prompt γ ray	79.5	1.64	^a 5.3
¹⁵⁷ Gd(n,γ) prompt γ ray	181.9	1.07	1.92

^a Crude estimates.

3.2 Measured Gd concentrations by PGNA

A comparison of the fitted spectra for all three measurements obtained for one of the participants is shown in Figure 3. The spectra show that there is no significant variation in participant set-up as all three spectra overlap quite well. In measurement (B), 12 ± 0.3 ppm of Gd was detected in the muscle, and the spectra clearly demonstrate the presence of Gd. A representative comparison of human and phantom spectra is shown in Figure 4. This figure demonstrates that the water phantoms are adequate representations of the human leg in terms of size and composition.

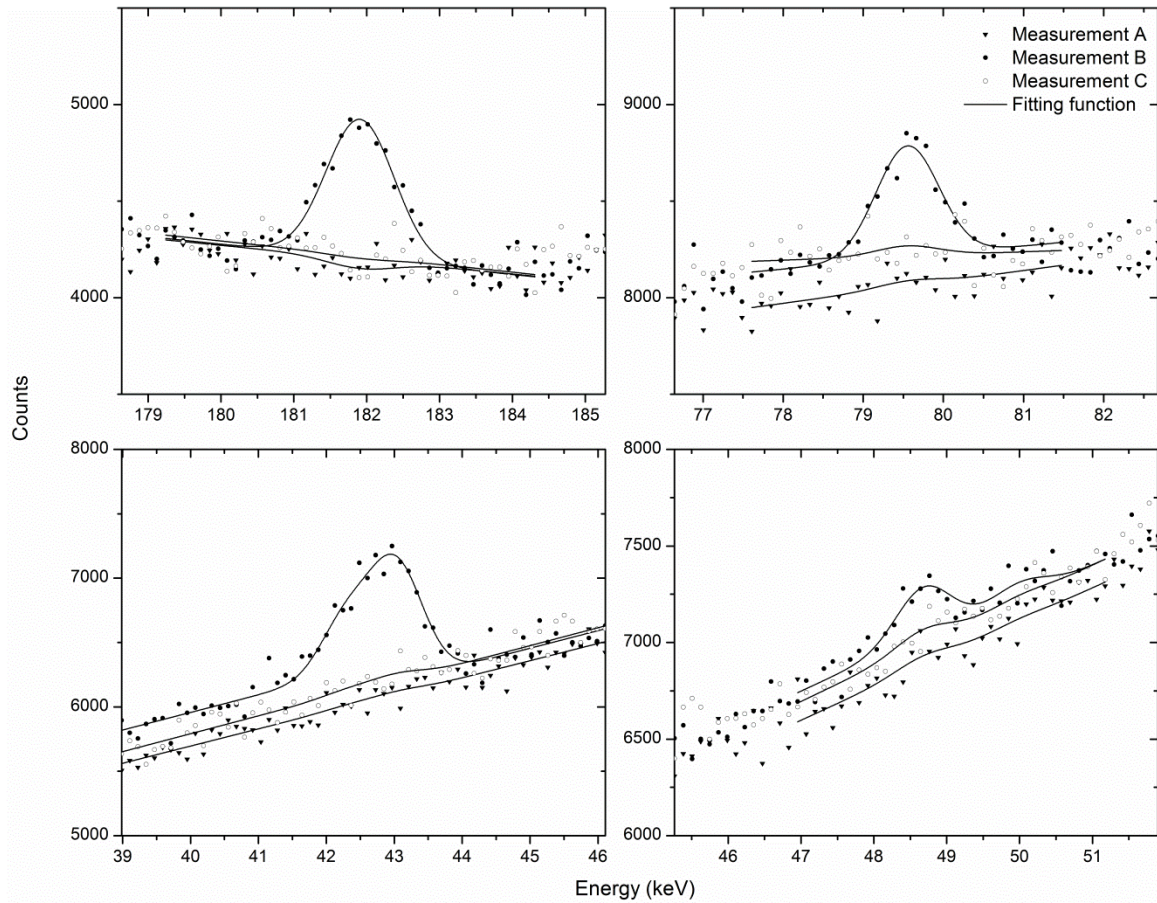


Figure 3. Comparison of the fitted spectra obtained for all three measurements from one of the participants. The four spectra are for the four photon emissions (see Table 2) used to quantify Gd from neutron capture of ^{157}Gd and ^{155}Gd measured by the LO-AX detector. In measurement (B), combined analysis of these four spectra determined a concentration of 12 ± 0.3 ppm Gd in the muscle.

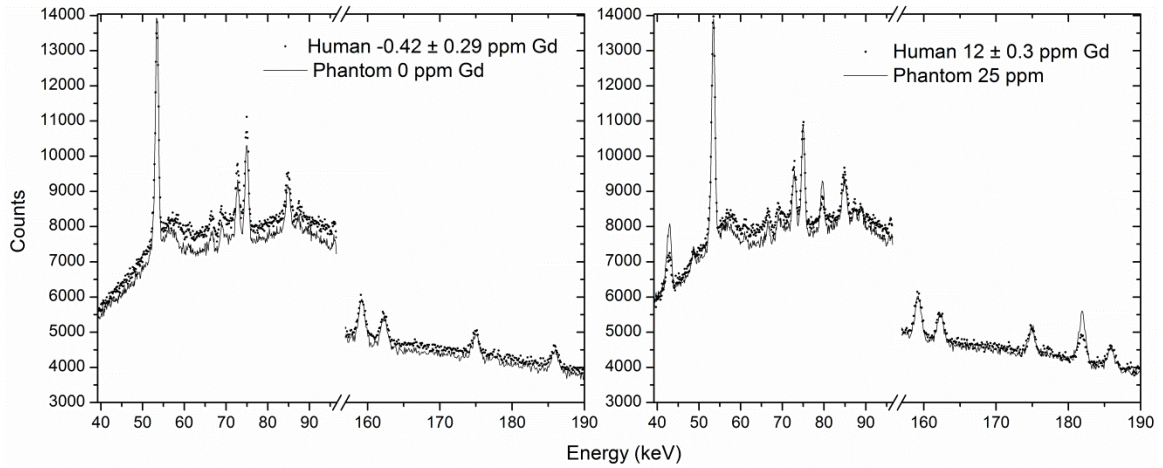


Figure 4. Comparison of human and phantom spectra in the Gd regions of interest.

The concentrations measured for each participant for each neutron scan are shown in Figure 5. In measurement (A), no participant's baseline Gd was significantly above zero, all were below the detection limit. However, two participants' measurements were significantly below zero (at the 95% confidence level), and the inverse variance weighted mean (IVWM) Gd concentration was -0.34 ± 0.09 ppm. This suggests that the peak fitting functions could be improved as the background is overestimated slightly. In measurement (B), all 10 participants had Gd concentrations significantly different from zero and above the detection limit of the system. In fact, the concentrations varied from 6.9 to 56 uncertainties different from zero (measurement divided by uncertainty), and from 4.9 to 54 uncertainties above the detection limit (measurement minus detection limit, divided by measurement uncertainty). The distribution of uncertainties different from zero is shown in Figure 6. The time from injection to measurement B varied from 38 to 50 minutes for 9 participants, and was 196 minutes for the one participant in which the unforeseen circumstances caused a delay in the time of measurement. These measurement concentrations are obtained over a period of 35 minutes. During the actual measurement, the contrast agent will be being cleared in the body by glomerular filtration. If a biological half-life of 90 minutes is assumed for the contrast agent, then the Gd concentration in muscle at the beginning of the neutron irradiation would be a factor of 1.14 times higher than the values in Figure 5B. Therefore because of biological

elimination the values in Figure 5B are an estimate of the time varying concentration of Gd present in muscle over the 35 minute measurement period. By the time of measurement (C), no participant had a Gd muscle concentration significantly above zero or above the detection limit. Again, however, two participants' measurements (different participants than in measurement (A)) were significantly below zero, and the IVWM Gd concentration was -0.27 ± 0.09 . Paired t-tests of the gadolinium concentration between measurement (A) and measurement (C) found no significant difference. The average concentration for the group was also found to be the same to within uncertainties. This demonstrates that there was no significant retention of Gd in the leg muscle 0.7 to 5.9 days post-injection in healthy volunteers to within the measurement uncertainty of this technique.

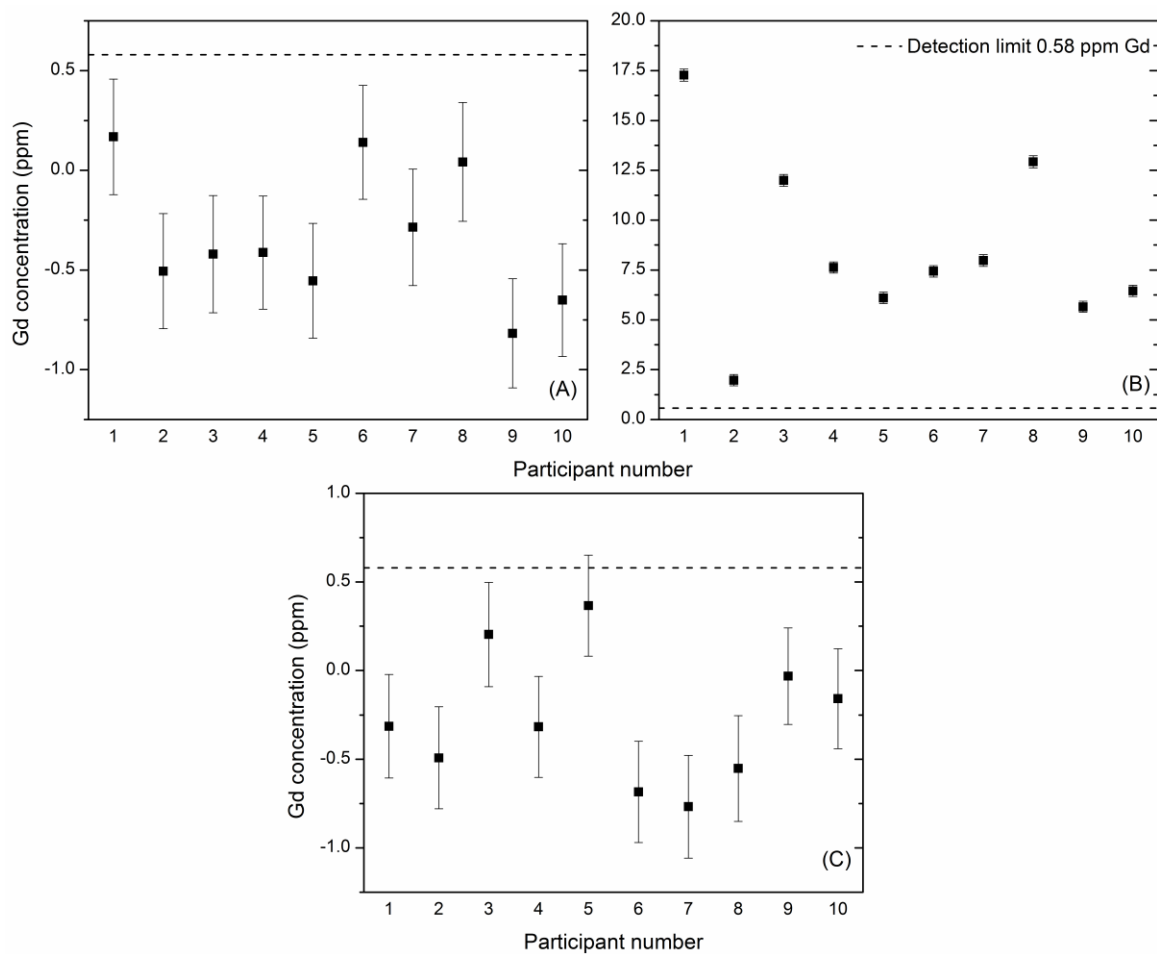


Figure 5. Gadolinium concentrations measured in the muscle for each participant for each of the three neutron leg scans.

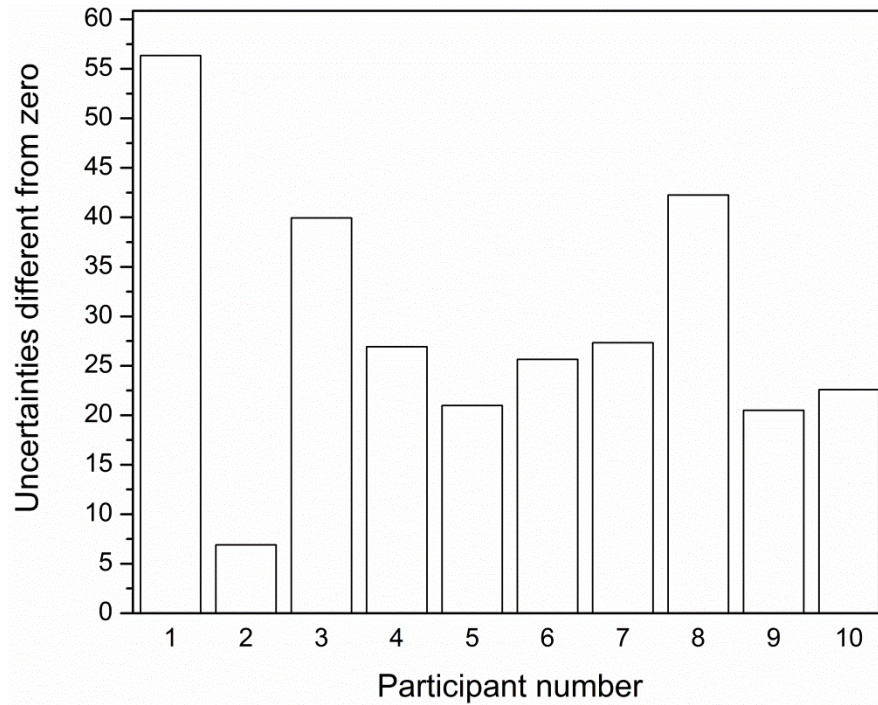


Figure 6. Distance from zero Gd concentration (divided by measurement uncertainty).

The Gd concentrations from measurement (B) were found to correlate significantly with the volume (mL) of contrast agent administered ($r^2 = 0.89$, $p < 0.001$), as well volume per body weight (mL/kg) administered ($r^2 = 0.71$, $p = 0.004$). This is shown in Figure 7. The single time-delayed measurement from participant #2 was excluded from the least-squares linear fits as it was made at a different point in time and Gd concentration could be expected to be lower because of the known biological half-life of the contrast agent.

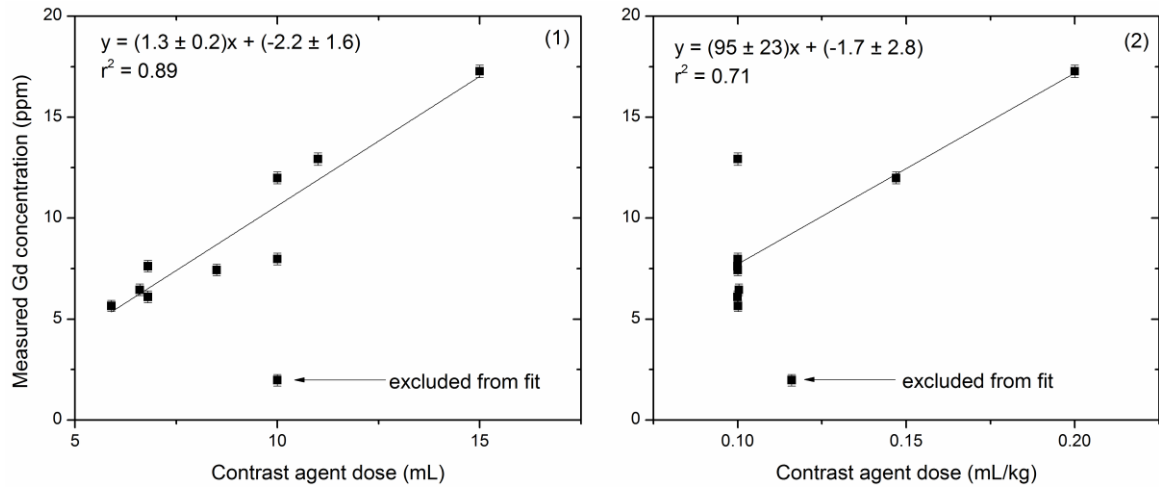


Figure 7. Gadolinium concentrations from measurement B as a function of (1) volume, and (2) volume per weight of contrast agent administered.

The original planned time-course of the experiment was for each of the ten subjects to be measured at similar time frames. The hypothesis was that measurement (A) would be zero for each person, gadolinium would be observed during measurement (B) and the signal would return to zero for measurement (C). The unplanned delay in measurement of subject #2, however, allows for another check and (admittedly crude) validation of the system, as it provides a single measurement of a fourth point in time.

The post-injection *in vivo* data were normalized to both volume (mL), and volume per weight (mL/kg) of contrast agent injected and plotted as a function of time after contrast agent injection. This is shown in Figure 8. If the data are fitted using a non-linear least-squares fitting routine to an exponential decay function, an estimate of a half-life of Gd as measured by the system is 80 ± 26 minutes for the data normalized to volume (a better r^2 was determined for this data). The known biological half-life of Gadovist® is approximately 90 to 120 minutes. The measurement results therefore predict a half-life that is comparable to the published value. This is admittedly a very crude estimate of the half-life since it relies on the one measurement from participant #2 that was significantly delayed. In addition, this participant also admitted to walking vigorously back to the TAB for the measurement and therefore the participants' cardiac output would be elevated, which may in fact increase the clearance rate of the contrast agent in their body.

Nevertheless, this estimate does lie within predicted values and provides some confidence in the measurement technology. We present these data not as a new estimate of half-life, but as some evidence of the system capability. We suggest that it demonstrates that it may be possible with this system to measure biological elimination rates of these contrast agents non-invasively *in vivo*, using an independent method, as the half-life calculated here is comparable to the nominal value.

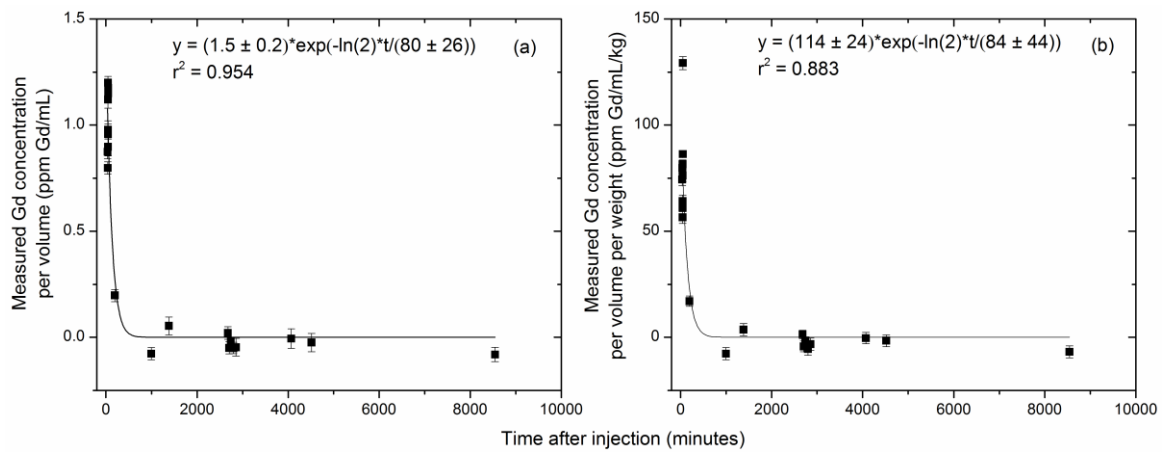


Figure 8. The measured Gd concentrations as a function of time after contrast agent administration normalized to (a) volume, and (b) volume per weight of contrast agent administered.

These findings validate that the measurement system is working as hypothesised. The results found here may also be helpful to researchers investigating diagnostic neutron activated imaging procedures since the measurements were made with a routinely used Gd-based MRI contrast agent and standard clinical doses were administered. Therefore based on the signal-to-noise measurements from these data, estimates can be made on image quality obtained in such procedures.

3.4 Gd *in vivo* detection limit

The *in vivo* detection limit in our laboratory is taken to be twice the median uncertainty of the measurements. The *in vivo* detection limit was 0.58 ppm. There was no significant difference in the uncertainties in all of the measurements, suggesting the participant

positioning was accurate, and that participant muscle size variability does not have a significant effect on measurement precision. The same detection limit found in humans as the phantoms demonstrates that the human leg muscle is adequately modelled by a 2 L aqueous polyethylene phantom.

Conclusions

To the best of our knowledge we report for the first time *in vivo* measurements of Gd in the human leg muscle in 10 healthy volunteers post-contrast agent injection by prompt gamma neutron activation analysis. Both the phantom and *in vivo* detection limit were determined to be 0.58 ppm. All participants had measureable Gd concentration above zero 38 to 196 minutes post-injection at the 99% confidence level. Gadolinium was not detectable in the pre-injection scan. Gadolinium was not found to be retained in muscle 0.7 to 5.9 days post-injection in the small population studied using this method. Some of the peak fitting functions could be improved slightly to remove the small negative offset in Gd concentration observed for the pre and late post-injection measurements. The results of this study promote further measurements in at risk populations to determine the potential retention of Gd after exposure to a Gd-based contrast agent using the PGNA method. The results of this study may also be applicable to researchers investigating neutron activated imaging techniques.

Acknowledgements

We would like to thank Norm Konyer for his assistance in securing resources at the IRC. Jason Falladown and Scott McMaster for all their technical support in the research lab at the Tandem Accelerator Building, and Dr. Mic Farquharson for providing space in his laboratory for the *in vivo* measurements. We also thank Dave Tucker and Christopher Malcolmson for their assistance with radiation safety related issues. We are grateful to all the participants who donated their time to this study. Ethics approval was granted by the Hamilton Health Sciences/St. Joseph's Healthcare Hamilton Research

Ethics Boards (Project # 11-297). This study was funded by McMaster University and the Natural Sciences and Engineering Research Council of Canada.

6.3 Additional material

6.3.1 Comment on the participant MR image data

The contents of Article IV above present the *in vivo* Gd concentration results measured by the PGNAA system developed in this thesis. MR images of the participants' lower left leg were also performed during this study. However the analysis of these images was not performed as part of this Ph.D. work. The MRI data may provide further information on muscle volume, the health of the leg tissues and the tissue perfusion/permeability properties. There may also be a relationship between MR signal enhancement from the contrast agent in the leg tissues and the amount of Gd measured by PGNAA. These data and any correlations determined are an area of potential future work.

6.3.2 Phantom calibration lines

The phantom calibration lines for both detectors and the photon emissions used in Article IV are shown in Figures 6.1 and 6.2. The intercepts of all the calibration lines are within 2 uncertainties of zero, except for the K_{α} line from the GMX detector. As described in Article III there is a germanium (Ge) escape peak in this region. If the data are fitted without subtracting the average background peak area the intercept is within 10.8 uncertainties of zero (ie. significantly greater than zero). When the average background peak area is subtracted the intercept is within -3.1 uncertainties of zero (still significantly different from zero at the 95% confidence level). This negative intercept suggests that subtracting the average background from this sample of 10 zero concentration phantom measurements has slightly overestimated the background Ge escape peak interference. No further adjustments were made as the GMX detector results make only a minor

contribution to the overall quantification of Gd for these measurements. The average reduced- χ^2 for the fits to the peak areas are shown in Table 6.1. All reduced- χ^2 values were within uncertainties of unity and therefore demonstrate that the peak fitting functions accurately fit the data from both phantom and *in vivo* measurements.

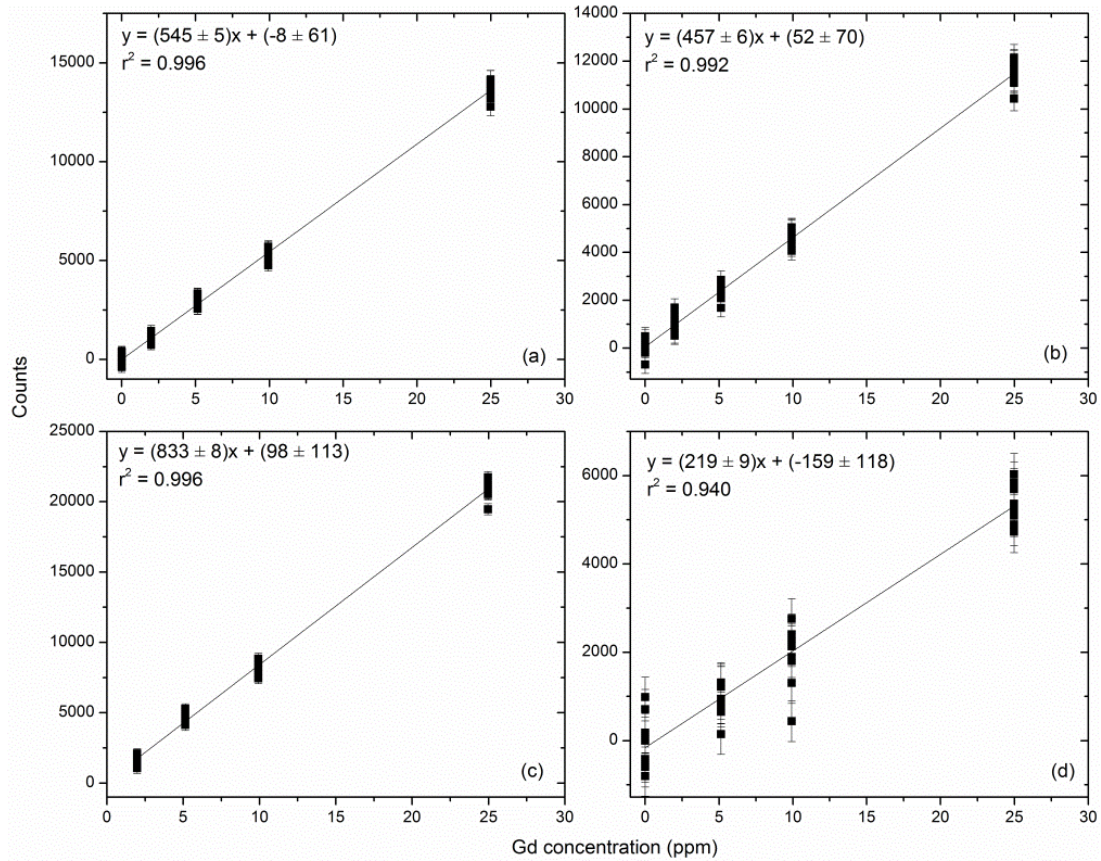


Figure 6.1. Phantom calibration lines from the LO-AX detector for 4 photon emission lines: (a) 181.9 keV, (b) 79.5 keV, (c) Gd K_{α} , (d) Gd K_{β} .

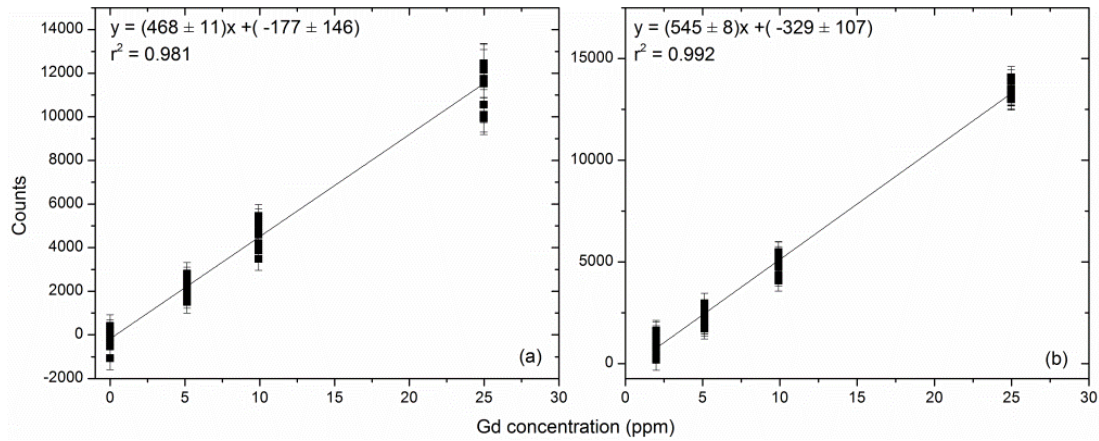


Figure 6.2. Phantom calibration lines from the GMX detector for 2 photon emission lines: (a) 181.9 keV, (b) Gd K_α .

Table 6.1. Average reduced- χ^2 from the peak area fits.

Transition	Photon Energy (keV)	Phantom		<i>In vivo</i>	
		LO-AX	GMX	LO-AX	GMX
K_α X ray	42.309, 42.996	1.2 ± 0.3	1.1 ± 0.2	1.0 ± 0.2	1.0 ± 0.2
K_β X ray	48.7, 50	0.9 ± 0.2	1.1 ± 0.4	0.9 ± 0.4	N/A
Prompt γ ray	79.5	1.0 ± 0.3	1.1 ± 0.3	1.0 ± 0.3	N/A
Prompt γ ray	181.9	1.1 ± 0.3	1.1 ± 0.3	1.1 ± 0.2	1.1 ± 0.2

N/A, not available; these peaks were not analyzed from the *in vivo* data because they will not improve the detection limit or measurement precision.

6.3.3 Spectra from the secondary detector

An example of the human spectra from the secondary GMX detector is shown in Figure 6.3. In measurement B, 17.3 ± 0.3 ppm Gd was found in the leg muscle tissues of this volunteer. The K_β and 79.5 keV emission lines were not used in the *in vivo* quantification of Gd in Article IV. The main reason these emissions were not used is because they are less intense than the K_α and 181.9 keV emission lines and have a larger background uncertainty compared to the LO-AX detector. It was found that these lines do not improve

the detection limit significantly. There are two reasons for the larger background uncertainty: firstly the poorer resolution of this detector and secondly a larger background level. A comparison of the peak resolution and detection limit from both detectors is shown in Table 6.2. A comparison of the spectra from a zero concentration phantom from both detectors is shown in Figure 6.4. This demonstrates how significant an effect the background level and detector resolution can have on the detection sensitivity of a measurement system.

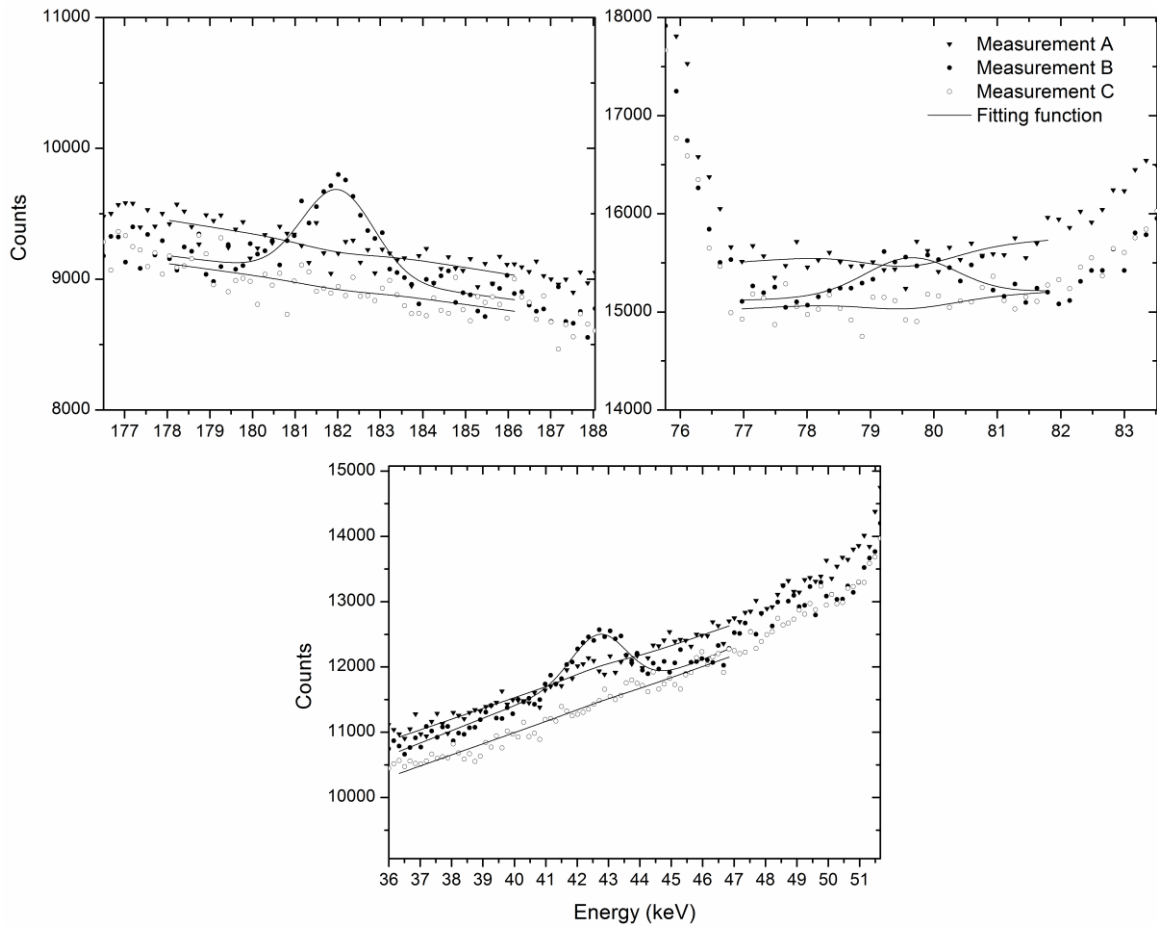
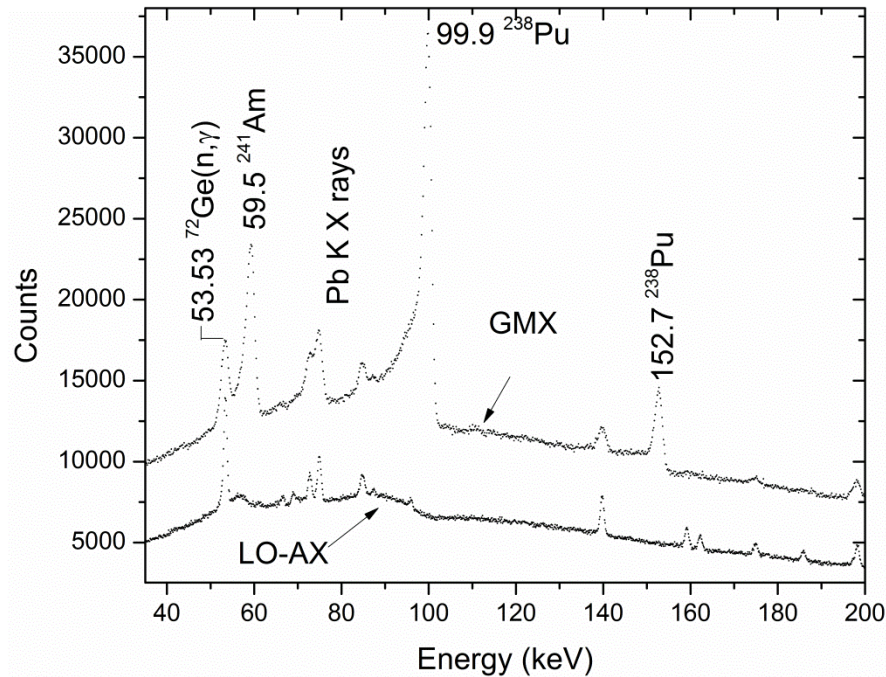


Figure 6.3. Comparison of the fitted spectra obtained for all three measurements from one of the participants. The spectra show four photon emissions from neutron capture of ^{155}Gd and ^{157}Gd measured by the GMX detector. In measurement B, 17.3 ± 0.3 ppm of Gd was detected in the muscle.

Table 6.2. Comparison of peak resolution and detection limits for the Gd photon emission lines from both detectors.

Transition	Photon Energy (keV)	M _{DL} (ppm)		Resolution (keV)	
		LO-AX	GMX	LO-AX	GMX
K _α X ray	42.309, 42.996	0.91	2.30	0.77	1.62
K _β X ray	48.7, 50	4.26	^a 10.9	0.76	1.47
Prompt γ ray	79.5	1.64	^a 5.3	0.85	1.43
Prompt γ ray	181.9	1.07	1.92	0.93	1.69

^aCrude estimates.**Figure 6.4.** Comparison of the spectra from the LO-AX and GMX detectors for a zero concentration phantom.

Also visible in Figure 6.4 are three peaks measured by the GMX detector, but not by the LO-AX, for this detection geometry. The gamma ray at 59.5 keV is most likely from the decay of ^{241}Am contained within the $^{238}\text{Pu}/\text{Be}$ neutron source. The source is enriched in ^{238}Pu , but also contains other isotopes of plutonium (Ellis 1990). The ^{241}Pu isotope, in particular, decays by β^- emission to ^{241}Am with a half-life of 14.3 years. The

other two peaks most closely match the gamma ray emissions from the ^{238}Pu decay of the $^{238}\text{Pu}/\text{Be}$ neutron source. The ^{238}Pu isotope decays by alpha emission to ^{234}U . In 71% of decays ^{238}Pu will decay directly to the ground state of ^{234}U . The remaining fraction of the time ^{238}Pu will decay to excited states of the ^{234}U nucleus, which decay by emitting gamma rays with energies of 43.5, 99.9, and 152.7 keV. The emission probabilities of these gamma rays are 0.039, 0.0073, and 0.00093, respectively (Browne, Tuli 2007). The most intense gamma ray at 43.5 keV is completely attenuated in the $^{238}\text{Pu}/\text{Be}$ source and therefore is not measured. This is an ideal situation because if they were not attenuated the 43.5 keV gamma rays could interfere with the fitting of the K X rays from Gd. The other gamma rays are able to penetrate the source and the Be pre-moderator (encased in Al housing) in significant enough numbers to be detected by the GMX detector. The gamma rays at 99.9 and 152.7 keV are able to escape the source as compared to the 43.5 keV due to the fact that the linear attenuation coefficient of ^{238}Pu for 40 keV photons is 10 and 7.8 times greater than 100 and 150 keV photons, respectively. The 43.5 keV gamma ray is above the L-edge of ^{238}Pu , the 100 keV is below the K-edge of 121.8 keV, and the 152.7 keV is above the K-edge, which explains the differential attenuation seen in the source itself and why the 43.5 keV photons do not escape. These emissions are seen by the GMX detector because the detector is located within the collimator dimensions and directly sees the source emissions (see Figure 1 of Article IV). The LO-AX detector does not measure these gamma ray emissions because these gamma rays are attenuated fully within the collimating and shielding apparatus. In addition, this detector is located behind an additional 2.5 cm of Pb.

Chapter 7

In vivo detection of samarium in the kidney by PGNAA

7 Introduction

Samarium (Sm), like gadolinium, is a lanthanide with a relatively large thermal neutron capture cross section. Samarium is a bright silver metal with atomic number (Z) 62, and atomic weight 150.36, and is present in the earth's crust at 7.05 ppm (Haynes 2012). Samarium has been proposed as a stable tracer for neutron activated imaging (Bell et al. 2011) due to its large cross section and the fact that the chemistry and safety profile for the routinely used ^{153}Sm -EDTMP is very well known. ^{153}Sm -EDTMP is used in the palliative treatment of painful bone metastases and emits a 103 keV gamma ray useful for SPECT imaging (McEwan 2000). The work here presents the feasibility of detecting natural samarium in the kidney. The specific results are useful in determining the general feasibility of neutron activated imaging. These results also potentially demonstrate a technique that permits measurement of samarium retention and exposure from clinical and, perhaps, accidental exposures.

7.1 Materials and methods

The ^{149}Sm isotope has a thermal neutron capture cross section of 40 100 b (S.F. Mughabghab, M. Divadeenam and N.E. Holden 1981), a natural abundance of 13.82%, and contributes 98.7% to the elemental neutron capture cross section. The main prompt gamma rays from the $^{149}\text{Sm}(n,\gamma)$ reaction have energies of 334 and 440 keV. The detection sensitivity of Sm in the kidney presented here is based on the intensity of the peak counts from these two gamma-rays as a function of concentration. These gamma ray peaks in the measured energy spectrum are fitted with a Gaussian function on a linear background. The optimized $^{238}\text{Pu}/\text{Be}$ system described in Section 4.3 of Chapter 4 is used

here to determine the samarium sensitivity in the kidney. The Pb shielded detector geometry resulted in an average background level reduction in the experimental peak regions of interest of about a factor of 1.77 at 334 keV, and 1.87 at 440 keV, compared to the situation in which no additional Pb shielding is present.

Samarium kidney phantoms were prepared by doping 125 mL polyethylene bottles filled with de-ionized water with concentrations of Sm ranging from 0-150 ppm using an atomic absorption solution (Ultra Scientific Inc., Catalogue No. IAA-062). The detector acquisition time of all measurements was set at the standard (i.e. as used in the Gd measurement studies, and previous Cd work) 2000 s live time, to allow a comparison of sensitivity and detection limits with previous results on other elements.

The detection geometry is shown in Figure 4.1 of Chapter 4. The experimental sensitivity is measured for the kidney placed at 4 cm lateral and axial depths and compared to the Monte-Carlo model of the system. The phantoms at 24.7, 50.3, 75.5, 100.6, 124.7, 149.6 ppm Sm were measured a minimum of three times each and the 0 ppm phantom was measured 5 times. A representative spectrum for a 150 ppm Sm phantom is shown in Figure 7.1. The Monte-Carlo model is easily adapted to Sm sensitivity measurements using the new ENDF/B-VII (Chadwick et al. 2006) data libraries for the seven naturally occurring Sm isotopes for the kidney material card composition. The same method described in Chapter 4 is also used to determine the detection limits for the kidney placed in various depths in the torso phantom. These detection limits could of course be applied to any other organ that is closely represented by phantoms of these sizes.

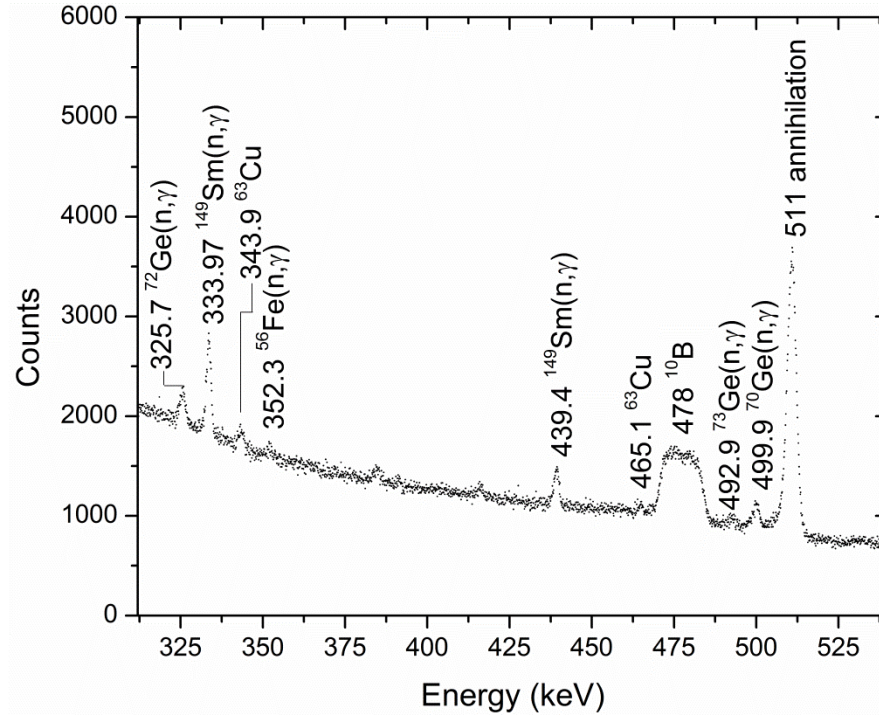


Figure 7.1. Representative spectrum from a 150 ppm Sm phantom showing the 334 and 440 keV prompt gamma ray emissions.

7.2 Results and discussion

7.2.1 Experimental sensitivity and detection limits

The fitted 334 keV and 440 keV gamma lines for a 150 ppm Sm are shown in Figure 7.2. The average reduced- χ^2 for the fits to both the 334 and 440 keV gamma rays was 1.1 ± 0.2 . This demonstrates that the peak fitting function is an accurate model to the data. The initial Sm sensitivity results for the kidney in 4 cm lateral and axial depths are shown in Figure 7.3. When performing a least-squares linear fit to the 440 keV data from 0-150 ppm a significantly non-zero intercept (different at a 95% confidence level), 2.9 uncertainties different from zero, was found. According to the Monte-Carlo simulation the self-shielding and fluence depression becomes greater than 4% above 75 ppm Sm (i.e.

the extrapolated divergence from a linear line determined from the sensitivity of a 5 ppm Sm phantom becomes greater than 4%). This may be “tilting” the straight line fit and creating a positive offset on the intercept. Evidence for this is that when fitting the 0-75 ppm Sm data only, the intercept is within 1.98 uncertainties of zero and so is not significantly different from zero at the 95% confidence level.

No such offset was seen in the 334 keV line and the intercept was actually within 0.4 uncertainties of zero for the fit to the 0-150 ppm data. However, when comparing the slope for the 0-150 and the 0-75 ppm data, the 0-75 ppm slope is significantly higher ($p = 0.02$) for the 334 keV line, which may suggest some curvature in the signal versus concentration relationship due to self-shielding and fluence suppression. To be consistent, both calibration lines were fitted using only the phantoms from 0-75 ppm. The least-squares linear fit results for both methods are shown in Figure 7.3. The detection limit for the 334 keV line is 6.2 ppm (0.79 mg) Sm, and 11.1 ppm (1.4 mg) Sm for the 440 keV line. The combined detection limit using the previously described inverse variance weighting method is 5.5 ppm (0.68 mg) Sm.

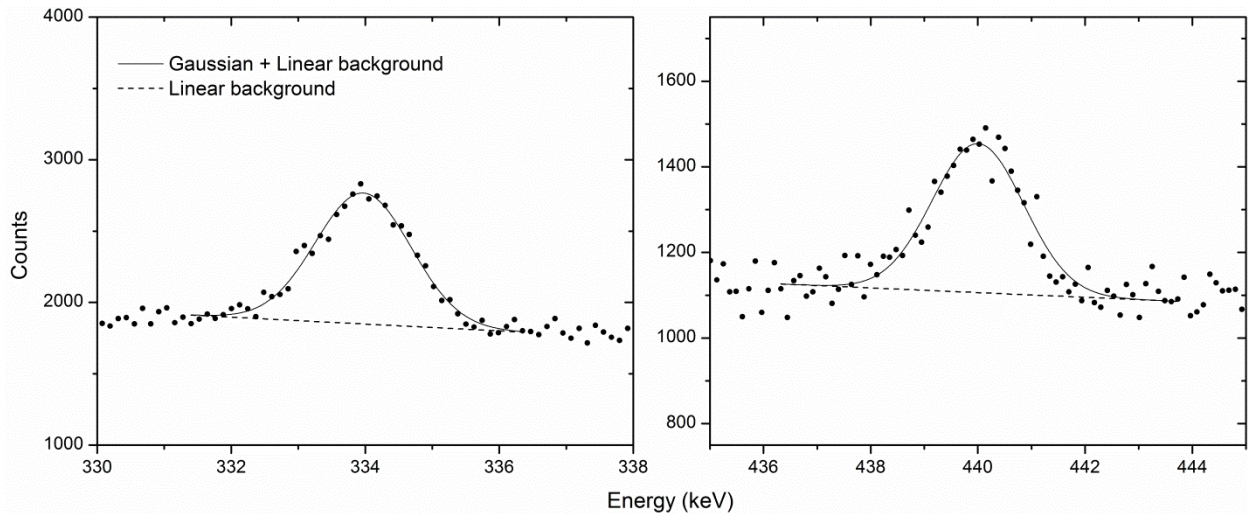


Figure 7.2. Representative spectra for the fitted 334 and 440 keV prompt gamma rays from Sm.

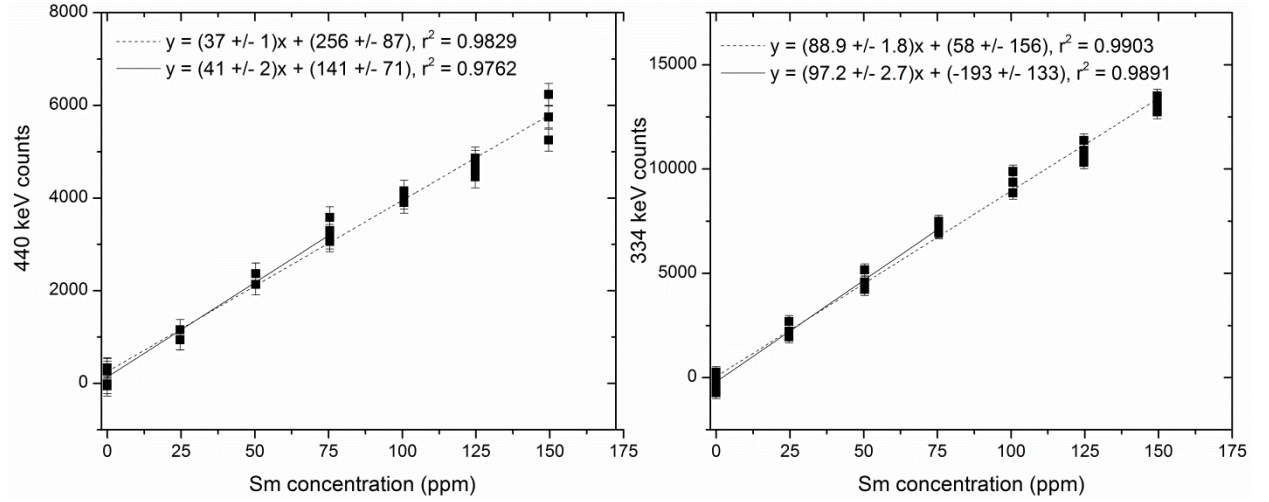


Figure 7.3. 440 and 334 keV experimental calibration lines for the kidney at 4 cm lateral and axial depths.

7.2.2 Monte-Carlo simulation of samarium sensitivity

The MCNP simulation results are presented in Figure 7.4. The agreement between MCNP and the experiment relies heavily on which gamma emission probabilities are used. As shown in Table 7.1, depending on the data source, there is a large variation for the emission probabilities for both the 334 keV and 440 keV ^{149}Sm emission lines; no such variation is seen in ^{157}Gd data. In Figure 7.4 the gamma ray sensitivities are simulated using the adopted Evaluated Nuclear Structure Data File (ENSDF) and International Atomic Energy Agency (IAEA) gamma ray emission probabilities. It should be noted that the IAEA data are based on evaluations which includes data from the references listed in Table 7.1 (except for the Groshev data). Also the Lone and Reedy and Frankle data are elemental emission probabilities, but since the ^{149}Sm isotope accounts for more than 98% of the thermal neutron capture cross section, I suggest that these can be considered as surrogate isotopic emission probabilities. The MCNP simulation agrees most closely with the experiment when the ENSDF adopted emission probabilities are used. A plot of experiment against MCNP using the ENSDF data yields a linear regression with a slope of 0.98 ± 0.03 and 0.99 ± 0.04 for the 334 and 440 keV data respectively. The r^2 values

for the trend-lines were 0.997 and 0.992, respectively. This suggests that the agreement between experiment and MCNP is better than to within 2% using the ENSDF data. It was found in Article II of Chapter 3 that the point source ratio of MCNP-to-experiment was 1.08 for gamma ray energies of 344 and 411 keV (these are close to the emission energies of the $^{149}\text{Sm}(n,\gamma)$ reaction). Therefore a ratio of experiment to MCNP of 0.93 was predicted from the modelled detector efficiency data: the agreement above is comparable but slightly better.

Using a similar analysis, the slope was 0.69 ± 0.02 and 0.68 ± 0.03 , when comparing the experimental and IAEA data for the 334 and 440 keV emissions, respectively, suggesting that the IAEA data are consistently higher by a factor of about 1.4.

A factor adding to the difficulty in determining the correct data set for the prompt gamma ray emission probabilities is a significant loss in detection efficiency noticed over the course of this experimental work. This is discussed in detail in the following section.

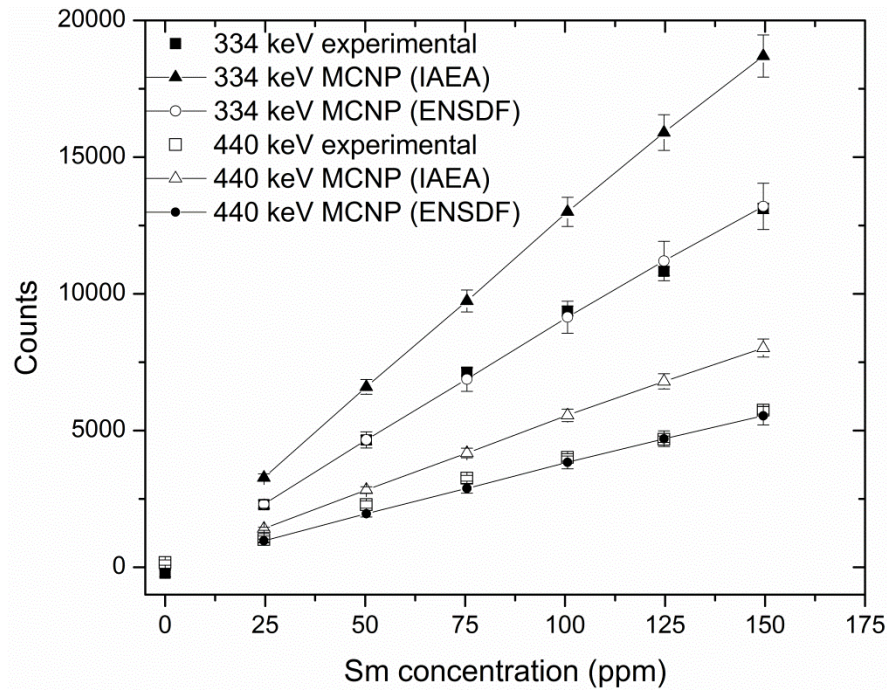


Figure 7.4. Comparison plot of the measured and simulated 334 and 440 keV peak areas. The simulated values are determined based on the gamma emission probabilities from two different sources.

Table 7.1. Comparison of the available data sources for the gamma emission probabilities for neutron capture in ^{149}Sm , and ^{157}Gd .

Isotope	Energy ^a (keV)	Reference				
		^b ENSDF	(Reedy, Frankle 2002)	(Lone, Leavitt & Harrison 1981)	^c (IAEA 2007)	(Groshev et al. 1963)
^{157}Gd	181.93	^d 18.33	18.33	---	18.1	---
	79.51	^d 9.748	9.748	---	10.09	---
^{149}Sm	333.97	^e 61	95.61	98.9	86.4	82
	439.40	^e 35.7	56.11	55.51	51.6	54

^a energies from IAEA Table 7.1

^b ENSDF adopted

^c derived from IAEA Table 7.1

^d (Helmer 2004)

^e (Smither 1966)

7.2.3 Detection efficiency loss

Since the time of the initial detection efficiency measurements presented in Article II, the Ge detector has been annealed twice and has been exposed to an estimated integrated neutron fluence of 3×10^8 n/cm² from the ²³⁸Pu/Be source (1×10^8 n/cm² after first anneal, 2×10^8 n/cm² after second anneal until the time of the Sm measurements; estimated based on exposure time and fluence from MCNP simulation). Before the first anneal, the detector was exposed to 10^9 n/cm². Over the course of this thesis work the detector has been exposed to an integrated neutron fluence of 2×10^9 n/cm². However, the total lifetime exposure of this detector to neutrons is unknown. The first anneal greatly improved the resolution of the detector as demonstrated in Article I. The detector was annealed at a temperature between 90 and 110 °C for approximately 75 hours, a service provided in house at the McMaster Nuclear Reactor. During a period of construction and experimental down-time in the laboratory the detector was also allowed to warm-up to room temperature, which we believe subsequently exaggerated the neutron damage, (as this has been observed by other authors such as (Raudorf et al. 1984, Kraner, Pehl & Haller 1975, Kraner 1980), causing higher than normal leakage current and poor resolution and detector performance. To repair this damage the detector went for its second anneal at 90 °C for 24 hours, and the detector operation and resolution were fully restored. Subsequently the detection efficiency was measured for the same geometrical configuration as in Article II. The ratios of the most current-to-initial detection efficiency measurement are shown in Table 7.2. There is a significant loss in detection efficiency with increasing photon energy. The fact that the loss in detection efficiency was observed for four different isotopes adds more confidence to the observed trend. This phenomenon has been observed in germanium detectors exposed to cosmic-ray proton fluence rates on the order of 10^8 p/cm²/yr (Kurczynski et al. 1999). The authors observed a loss in efficiency which was attributed to a change in the germanium detector from n-type to p-type in the damaged regions (Kraner 1980, Kurczynski et al. 1999). This results in some of the detector becoming un-depleted (when operated under the original high voltage

bias), and therefore acting as dead region that does not contribute to gamma ray detection. The authors estimate an increase in acceptor concentration at a rate of approximately $4 \times 10^8/\text{cm}^3/\text{yr}$. Estimating in the same fashion, using the number of damaging neutron interactions (both elastic and inelastic collisions) determined from MCNP computation, the acceptor concentration is expected to have increased to on the order of $10^9/\text{cm}^3$. This is considering only the neutron exposure after the second annealing. If some of the damage was not repaired after the two annealing periods, this number could be considerably higher. The nominal donor impurity concentration in this type of detector is on the order of 10^9 to $10^{10}/\text{cm}^3$ so the calculated level of change in acceptor concentration would be expected to have a significant effect on detector performance.

Table 7.2. Ratio of the most current-to-initial full-energy peak efficiency measurement. The n-type Ge detector efficiency has decreased as a function of energy due to neutron damage.

Isotope	Photon energy (keV)	Efficiency ratio
^{155}Eu	86.55	1.00
	105.31	0.94
^{152}Eu	244.7	0.74
	344.28	0.71
	411.12	0.68
^{137}Cs	661.66	0.60
^{154}Eu	1004.73	0.62

This has also been observed by other authors in two n-type germanium detectors, both exposed to a large proton fluence (Pirard et al. 2007). The authors irradiated one of the detectors with a proton fluence of $7.5 \times 10^{10} \text{ p/cm}^2$ incident from the side direction and observed a loss in efficiency using gamma ray point sources incident on the irradiated side. The efficiency loss was noticed from the irradiated side because protons have a finite range in matter (in this experiment in the literature 49 MeV protons; range of 7 mm in germanium). The second detector was irradiated from the front with a proton fluence of

10^{10} p/cm². For this second detector the ratio of the intrinsic full-energy peak efficiency after proton exposure to the pre-irradiated efficiency was 0.64 at 1.33 MeV (Pirard et al. 2007); comparable to the loss observed here. The efficiency for both detectors was not recovered to its original value after annealing (annealing temperature ranged from 22-100°C, and time was on the order of days), only the peak resolution was recovered after annealing (Pirard et al. 2007). This could explain why the n-type detector resolution, used here, was recovered after annealing but the loss of efficiency was still present. In fact it has been reported that annealing times on order of months at a temperature 100 °C are required to repair this type of damage (Quarati et al. 2009).

Since the p-n junction of this n-type detector is located at the outer-surface, the depletion region extends inward, and therefore this may explain why the loss in efficiency becomes significant as the photon energy increases. If the efficiency ratios are plotted against the photon mean free path (mfp) in germanium, an exponential relationship is found. This is shown in Figure 7.5. Therefore this demonstrates that the loss of efficiency increases with the penetrability of the photon radiation with an exponential rate of 0.18 per cm of mfp. This also confirms that there were no errors in repositioning between the two experiments because a $1/r^2$ effect in distance would reduce the apparent efficiency by the same amount at each photon energy.

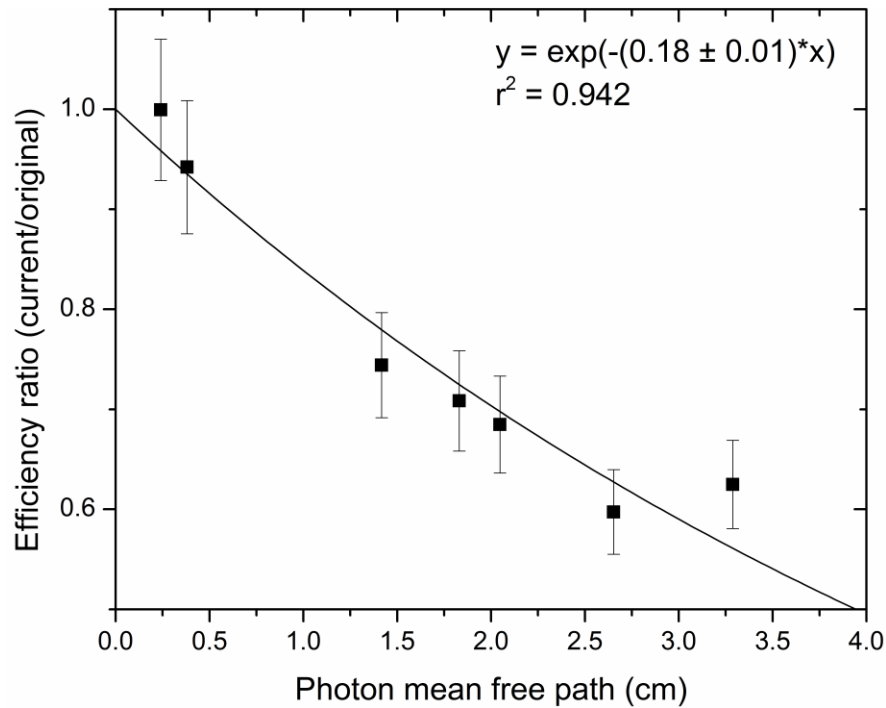


Figure 7.5. Relationship between loss in efficiency and photon mean free path.

Loss of efficiency has also been noticed in a similar germanium detector that was exposed to prolonged annealing at 100 °C, and the phenomenon was explained by diffusion of the inner Li contact by Fick's diffusion law (Owens et al. 2007). Therefore, it cannot be ruled out that there may be an added effect to this detector from the diffusion of the inner Li contact during the annealing that occurred during the room temperature warm-up and the two high temperature annealing periods described above. In addition, this detector is over 13 years old, and through discussions with ORTEC, impurities in the cryostat can build up over time and deposit in the crystal. Therefore the loss of detection efficiency measured here is probably a result of many complex variables.

Since this is a rather unusual phenomenon and the literature on this subject is limited, the originally measured efficiency was re-visited. In order to verify that there were no systematic errors in the peak fitting for the efficiencies measured initially, the peaks areas were determined using two methods of numerical integration and compared with the original fits. The first method of numerical integration was a simple summation over the peak region and the background was subtracted by taking the area under the

linear line through the endpoints. The second method is described in Debertin and Helmer (1988). In this method the peak area is summed over $3w$ (w = full width at half maximum), and the background is summed over $1.5w$ to the left and the right of the peak. Therefore, in this method a step function is formed over the background. When comparing the peak areas obtained from the original fits and that of the two numerical integration methods, the deviation was less than 3.6%, and on average 1.7%. Therefore this is within the precision of the efficiency measurement since the source activities used are known to within 5%, and it can be said that there was no systematic error in the original efficiency measurements.

It may be possible to verify the loss of detection efficiency further by three methods. The first method would be to over-bias the operating high voltage (i.e. apply a voltage above the recommended level) to deplete the damaged detector fully. This was performed by Kurczynski et al. (1999), and an improvement in the efficiency after proton damage was observed as the high voltage was raised from the original 1953 V in steps up to 2753 V. It should be stressed that through correspondence with the manufacturer (ORTEC), raising the high voltage for this detector was not recommended, as there could be the potential for breakdown. The second method could be to anneal the detector for a longer period of time. A time period of 11 weeks of annealing (at 100 °C) was required to restore an n-type Ge detector's relative efficiency at 1332 keV to greater than 85% of its pre-irradiation value (Quarati et al. 2009). Therefore longer annealing times may be more effective than the 24 and 75 hours performed here. The third method could be to have three small volume germanium crystals. For the study period, have one crystal unexposed to neutrons and measure the resolution and efficiency at various intervals. The other two crystals would be exposed to neutrons and the efficiency and resolution would be measured after neutron fluence exposures from zero up to, for example, 10^{10} n/cm². One of the two crystals that were exposed to neutrons would also be subject to a thermal temperature cycle and the resolution and efficiency recorded. This detector could also be annealed at 100°C and the resolution and efficiency measured again. Comparing the results of these three detectors could verify if such a significant efficiency loss is

occurring after neutron exposures and if the thermal temperature cycling and annealing has any effect. Another variable that would need to be considered would be the neutron energy for these experiments, and it may be necessary to repeat these measurements for different neutron energy regions (for example: in a reactor beam port (mostly thermal region), a $^{238}\text{Pu}/\text{Be}$ source (average energy ~ 4 MeV), and the $^7\text{Li}(p,n)$ reaction (typical average energies are on the order of a few hundred keV or less depending on incident proton energy). Although these three methods do have their limitations in terms of practicality, they could be a means of verifying the loss of efficiency, and providing a further understanding to the mechanism. With hindsight, it would have been ideal to measure the detection efficiency monthly over the course of this thesis, but the observations noted here were not anticipated in the original experimental planning.

The detection efficiency loss in the 300-400 keV energy region closely matches the relationship between the ENSDF data and the IAEA adopted data for the Sm gamma ray emission probabilities. In other words the efficiency is factor of approximately 0.7 lower, and the ENSDF data is exactly the same factor lower than the IAEA. This could mean that in reality the best agreement between experiment and MCNP would be with the gamma ray emission probability adopted by the IAEA since the experiment is consistently producing data that is 0.7 times lower than that simulated with the IAEA data. In other words the reason that such a good agreement between experiment and simulation using the ENSDF data may be due to the fact the detector is damaged and therefore has a lower efficiency that would appear to match with the ENSDF data. In this case it just so happens that the ratio of efficiency loss and the ratio between these two data sets coincide quite well. These discrepancies are obviously an area worth further research.

7.2.4 Comment of the loss of efficiency in the Gd photon emission energy region

The loss of efficiency curve in Figure 7.5 could be used to estimate the loss of detection efficiency for the Gd energies of interest. Using the corresponding mfp for the Gd emission energies of 79.5 and 181.9 keV, the efficiency (loss) ratio for point sources of these energies would be 0.966 ± 0.002 and 0.84 ± 0.01 , respectively. No efficiency loss would be expected for the K X ray region (40-50 keV) as no significant loss was noticed at these low energies. A small but insignificant loss in efficiency is estimated for the 79.5 keV line. The estimated loss in efficiency for the 181.9 keV line from the fitted curve is significant, however, this was not noticed in the experimental measurements of the 2 L and 125 mL Gd phantoms. Using the MCNP model for comparison over the course of this thesis work the agreement between the experiment and MCNP model does not seem to be effected by such an experimental loss in efficiency in this energy region. For example, the original ratio of MCNP to experiment was 1.10 ± 0.01 ($r^2 = 0.999$). (The ratio is determined by plotting MCNP against experiment and taking the slope of a least-squares linear fit to data.) After the detector was annealed, the ratio reduced to 0.95 ± 0.02 ($r^2 = 0.999$), in other words the experimental sensitivity increased. This is most likely a result of the improved peak fitting because the detector resolution was improved, and therefore the 181.9 keV peaks could be fitted with a single Gaussian function as opposed to a double Gaussian as described in Article I. The most recent 181.9 keV sensitivity measurements demonstrate that the ratio of MCNP to experiment has increased to 0.99 ± 0.01 ($r^2 = 0.999$). In other words the experiment has decreased only slightly by a factor of 0.96 ± 0.02 . This is not as significant as the estimated loss from the fitted exponential curve above. The reason for this could be that the damage and efficiency loss may not be uniform across all photon energies, and therefore the efficiency loss at 181.9 keV may not be accurately described by the exponential curve that is based on higher photon energies that is shown in Figure 7.5.

7.2.5 Predicted detection limits for various body types

The system, despite a few discrepancies that I suggest are related to detector damage, is now, however, well benchmarked for Sm sensitivity in the kidney. To determine the detection limit dependence on kidney phantom position, the experimental zero ppm measurements were combined with the simulated sensitivity as in Chapter 4. The zero ppm phantoms were measured in various lateral and axial kidney depths, the background zero concentration peak area uncertainty was then determined in each position. The background peak area uncertainty is determined for each position because the detector is repositioned and aligned with the kidney phantom for each position within the torso phantom. The combined experimental and simulated results allows for a simple determination of the detection limit for various patient body types (varying overlying tissue) as shown in Figure 7.6.

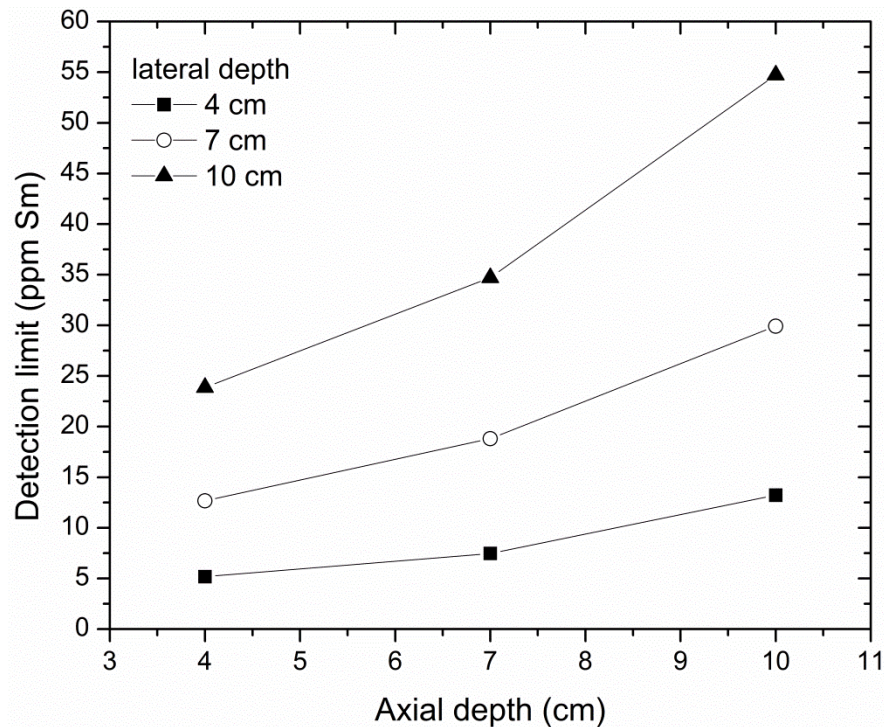


Figure 7.6. Samarium kidney detection limits for various overlying tissue thicknesses.

The detection limits were simulated using the gamma ray emission probabilities from ENSDF (Smither 1966). Although it is yet undetermined which data set is correct, the detection limits were calculated for the current experimental system and the ENSDF emission most closely matches the current system. These detection limits could simply be modified by the ratio of gamma ray emission probabilities if it is determined in the future which data source is the most accurate and if a different detector (of the same size) is used. The simulated detection limits for the 4 cm lateral and axial position are 5.9 ± 0.4 and 11.1 ± 0.7 ppm for the 334 and 440 keV lines, respectively. As a comparison the experimental detection limits determined in Section 7.2.1 above were 6.2 and 11.1 ppm, agreeing quite well with the simulated. The total detection limits range from 5.2 ppm (0.64 mg) to 54 ppm (7 mg) Sm for the shallowest and greatest depths considered, respectively.

The detection limit for the 334 keV line of Sm is 1.5 times higher than the 181.9 keV line from neutron capture in ^{157}Gd . Taking into account the lower background in the 334 keV region compared to the 181.9 keV region, the gamma ray emission probabilities, detection efficiencies, natural abundances, and thermal neutron capture cross sections, the predicted ratio of detection limits would be 3.4. This difference between predicted and measured by more than a factor of 2 can be explained by the fact that both ^{149}Sm and ^{157}Gd are non- $1/\nu$ isotopes, and therefore the neutron capture probability is no longer directly proportional to the thermal neutron capture cross sections, and is strongly dependent on the neutron fluence spectrum (Sun, Byun & Choi 2003). So therefore despite the fact that the ^{157}Gd isotope has a thermal neutron capture cross section some 6.3 times larger than the ^{149}Sm isotope (comparable natural abundances of 15.65% and 13.82% respectively), the simulated ratio of neutron interactions in ^{157}Gd to ^{149}Sm is lower than would be expected by more than a factor of 2 if we were comparing isotopes with cross sections that follow a pure $1/\nu$ trend without any resonance structure. It would appear that the neutron fluence spectrum from the $^{238}\text{Pu}/\text{Be}$ source in the kidney phantoms is more favourable for ^{149}Sm compared to ^{157}Gd . A plot comparing the neutron capture cross-sections of ^{157}Gd to ^{149}Sm is shown in Figure 7.7. The neutron fluence rate

spectrum in the kidney phantom is also shown in Figure 7.7. The neutron fluence rate spectrum appears to match quite well the pronounced resonance seen in the ^{149}Sm neutron capture cross section. Although this is a rather crude comparison since the binning of the neutron fluence spectrum was much larger than the binning of the cross section data. The pronounced resonance occurs at around 0.1 eV and is a region where the ^{149}Sm cross section actually surpasses the ^{157}Gd cross section. There are also many other regions where the ^{149}Sm neutron capture cross is larger than ^{157}Gd . In Table 7.3 the proportion of neutron captures per neutron energy bin are calculated for ^{149}Sm and ^{157}Gd . Also shown in Table 7.3 are the relative capture rates of ^{157}Gd to ^{149}Sm per neutron energy bin. For ^{157}Gd the majority of the neutron captures are in thermal region, whereas for ^{149}Sm a significant proportion of captures (13%) also come from the epithermal component. The ratio of the relative capture rates demonstrates that the number of neutron captures with ^{157}Gd is larger than ^{149}Sm for the thermal region only.

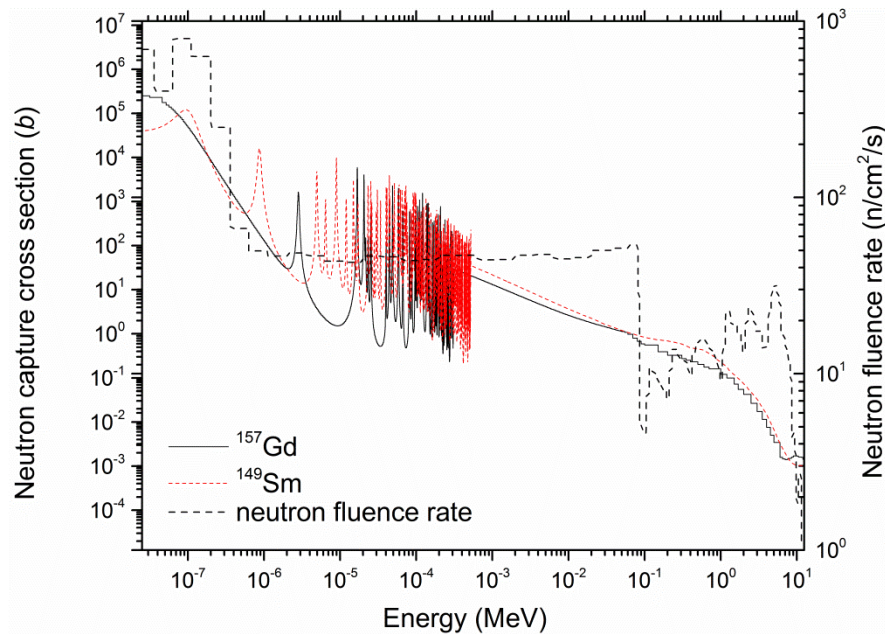


Figure 7.7. Comparison of the neutron capture cross-sections of ^{157}Gd and ^{149}Sm from ENDF/B-VII.0. The neutron fluence rate spectrum in the kidney phantom is also shown on the secondary y-axis.

Table 7.3. Comparison of the proportion of neutron captures per neutron energy bin for ^{149}Sm and ^{157}Gd . Also shown is the ratio of the number of captures in ^{157}Gd to ^{149}Sm per energy bin.

Energy classification	Energy bin	^{149}Sm	^{157}Gd	Ratio ($^{157}\text{Gd}/^{149}\text{Sm}$)
Thermal	0 – 0.1 eV	0.87	0.98	3.40
Epithermal	0.1 eV – 1 eV	0.13	0.02	0.46
Resonance	1 eV – 1 keV	5.9×10^{-4}	7.6×10^{-5}	0.39
Intermediate	1 keV – 1 MeV	1.5×10^{-5}	3.3×10^{-6}	0.65
Fast	> 1 MeV	2.0×10^{-7}	3.7×10^{-8}	0.56

7.2.6 Sm K X rays

Similar to neutron capture with Gd, there were observable Sm K X rays in the spectrum due to internal conversion electron de-excitations from the excited $^{150}\text{Sm}^*$ isotope. A long measurement for a 20 000 s live time was performed to determine the Sm K X ray sensitivity. The fitted Sm K X rays are shown in Figure 7.8. The fitting functions used in Article III were used to fit the Sm K X rays. The normalized amplitude factors, f_i , were modified to correspond to the X ray intensity ratios for Sm. The reduced- χ^2 for the fits was 1.1 and 0.85 for the K_α and K_β peaks, respectively. The number of counts in the K_β peak was, however, low, at 5032 counts after 20 000 s. The ratio of K_β to K_α peak area was 0.20 ± 0.05 , comparable to the expected value of 0.243 (Elam, Ravel & Sieber 2002). Although they have a relatively low emission rate, with only 1.27 ± 0.06 counts/s for the Sm K_α X rays, the Sm K X rays could potentially help determine the correct emission probability for the ^{149}Sm prompt gamma rays since there was no noticeable loss in efficiency in the low energy region. Therefore the simulated Sm K X ray sensitivity calculated by the same method as in Article III using the IAEA and ENSDF adopted gamma ray emission probabilities could be compared to the experimental. However, the calculation with Sm is much more complicated than the Gd situation. It appears that the contribution to internal conversion electron emission in $^{150}\text{Sm}^*$ is a result of many nuclear transitions as compared to the relatively simpler situation in Gd where the majority of the

contribution was from the first and second excited states of $^{156}\text{Gd}^*$ and $^{158}\text{Gd}^*$. This calculation relies on very accurate knowledge of the Sm level scheme, and internal conversion electron and gamma ray emission. Since there is a limited amount of new data on Sm, no such calculation was performed here, but this could be one method to verify the gamma ray emission data-sources.

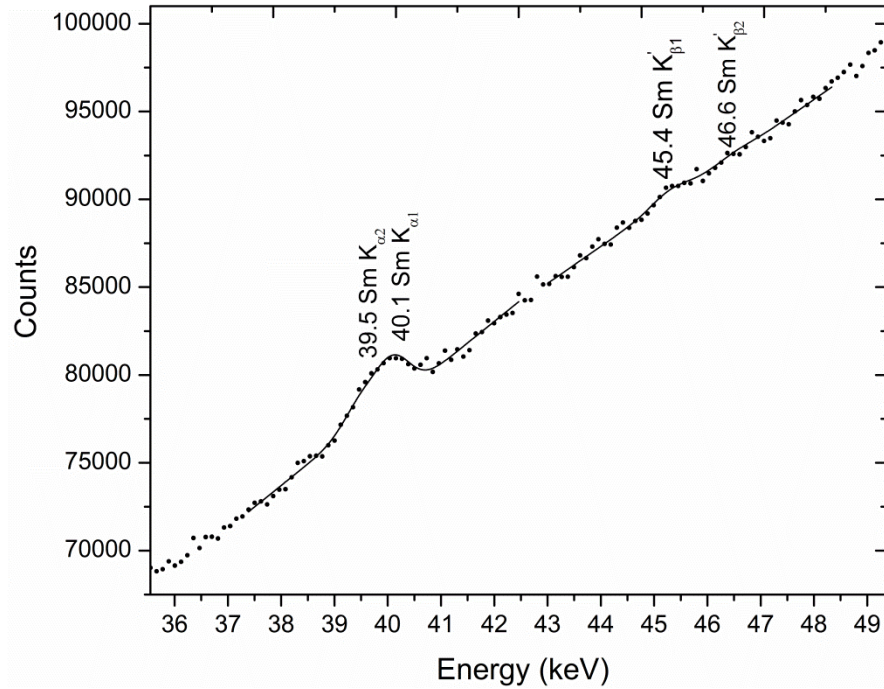


Figure 7.8. Spectrum of the fitted Sm K Xrays from a 150 ppm Sm kidney phantom for a 20 000 second acquisition.

7.3 Conclusions

Initial *in vivo* Sm sensitivities for the kidney have been determined by experiment and Monte Carlo simulation. Excellent agreement was seen when the ENSDF adopted gamma emission probabilities are used for the detector in its current state. The discrepancies in the prompt gamma ray emission probability data for neutron capture in ^{149}Sm make it difficult to determine which gamma ray emission data are correct. Also the noticed detection efficiency loss in the energy region of interest complicates matters

further. It appears most likely that the most appropriate data for the prompt gamma ray emission probability of Sm are the adopted IAEA data, if the damage to the HPGe detector is taken into account.

Of importance for image quality in neutron activated imaging is the amount of photons that can be collected in the detector during the imaging process. Now that the detection of ^{149}Sm has been benchmarked in MCNP, future simulations can be performed to assess the feasibility of such imaging procedures in terms of image quality. This study on Sm also demonstrates the feasibility of measuring Sm retention from medical exposures, or perhaps, occupational, environmental, or accidental exposures.

Chapter 8

Conclusions

8.1 Discussion and thesis conclusions

The present day routine use of gadolinium-based contrast agents demonstrates the need for a non-invasive routine gadolinium monitoring system for study of these agents. The reported numbers of cases of nephrogenic systemic fibrosis (NSF) have admittedly significantly decreased since the implementation of new guidance protocols and warnings for use in the renally impaired. The main contrast agents that were linked to NSF were Omniscan, OptiMark, and Magnevist. These agents were considered to be the most unstable, and the current use of these particular agents appears to be minimal, if used at all, in the group of people at risk, the renally impaired (Marckmann 2011). As newer and safer contrast agents merge into the market the concern regarding gadolinium-based chelates is perhaps diminishing as compared to when this thesis work began. However, no chelate can be 100% stable as there needs to be at least one open site for Gd to interact with the surrounding water molecules. It has recently been reported that levels on the order of parts per million have been retained in bone of healthy people who have received a Gd-based contrast agent up to 8 years prior to hip replacement surgery (Darrah et al. 2009) which suggests instability of the chelate and is an argument that it is, in fact, less than 100% of the Gd bound to chelate that is excreted. The retention at part per million levels in bone is a significant amount (when compared against current levels of environmental exposure to toxins such as Pb). The subsequent release of this due to bone turnover and remodelling (as has been observed in Pb exposure (Popovic et al. 2005)) may be a concern, especially if the patient will be repeatedly exposed to these agents, or will be given a higher than normal dose. The long-term health effects from single or multiple exposures to Gd-based contrast are still yet unknown. In this dissertation a new non-invasive method to measure Gd retention, *in vivo*, by PGNAA in the kidney, liver, and muscle was developed.

In Chapter 2 the first ever feasibility study on the measurement of *in vivo* Gd by PGNA was performed. Estimates were made of the initial phantom detection limits for the system. The system was optimized over the course of the feasibility study. The detector was repaired of neutron radiation damage by annealing which greatly improved the resolution and reduced the background peak area uncertainty. The background signal was reduced further by incorporating a 2.5 cm thick Pb shield. In addition, the slope was used at lower concentrations to avoid the non-linearity from self-shielding and fluence depression due to the enormous neutron capture cross section of Gd. These optimizations reduced the leg muscle detection limit from 2.3 to 0.89 ppm. A factor of improvement of at least 1.7 was expected for the kidney and liver.

A Monte-Carlo model of the experimental system was created in Chapter 3 to assist in system optimizations and to verify some of the results observed experimentally. The agreement between the model and experiment was, on average, better than 10%. This agreement is excellent for an *ab initio* computation. The model was able to confirm the non-linearity and turnover in the calibration lines due to self-shielding and fluence depression phenomena. The model was also used to characterize some of the properties of the neutron field from the collimating and shielding apparatus. MCNP computation also proved to be very important for the simulation of the radiation dose to the patient. In the future, the model may be helpful for system optimizations, simulating the sensitivity in other tissues or organs, and in addition it could be applied to other high neutron absorbing isotopes.

An interesting improvement in the sensitivity of measuring Gd was determined by using the characteristic K X rays which are more probable than the 181.9 keV line from neutron capture of ^{157}Gd in a PGNA experiment on natural Gd. In Chapter 4 the agreement between experiment and theory for the K X ray emission resulting from internal conversion electron emission from neutron capture of ^{155}Gd and ^{157}Gd was well demonstrated, with the experiment being higher consistently by 5%. In this thesis, the measurement of *in vivo* Gd was developed to be a combination of prompt gamma and ‘prompt X ray’ neutron activation analysis. The X ray emission may also provide for a

depth correction when measuring Gd retention in organs due to the differential attenuation in tissue of the X ray energies compared to the prompt gamma rays.

The detection limits for the kidney and liver for varying overlying tissue thicknesses were determined with the help of the MCNP model. These detection limits provide an estimate for the measurement of Gd retention in a variety of patient body types. These detection limits are based on two prompt gamma ray emissions (79.5 and 181.9 keV) and the Gd K X ray emissions. The kidney detection limit for the shallowest depth considered (4 cm axial and lateral depths) was determined to be 2.3 ppm. The liver detection limit for the shallowest depth (7 cm axial and lateral depths) was determined to be 0.74 ppm. The same 2 L phantoms for the liver are used to represent the leg muscle. The liver detection limit is larger than the optimized leg detection limit of 0.58 ppm because of the larger background (from Compton scatter of the 2.223 MeV gamma rays from neutron capture on hydrogen) for the liver irradiation geometry due to the presence of the torso phantom and attenuation of the gamma ray and X rays in the torso phantom.

The radiation dose to the participant was determined in detail in Chapter 5. In previous calculations for the kidney irradiation geometry the kidneys, liver, skin, and testicles were considered (Atanackovic et al. 2007). For many other studies only the entrance dose rate was considered ((Grinyer, Byun & Chettle 2005) and references therein). More organs-at-risk for radiation exposure were considered in this thesis. It was found in the kidney irradiation geometry that the largest contributor to the effective dose was the stomach. The kidneys do receive the largest equivalent dose, however, the kidneys are considered a remainder organ by the ICRP and therefore are weighted less than the stomach when calculating the effective dose. The effective dose rate for the kidney irradiation was calculated to be 74 $\mu\text{Sv/hr}$, which corresponds to a dose of 41 μSv for a 2000 s measurement. The liver and gall-bladder receive the largest equivalent doses for the liver irradiation. The effective dose rate for the liver irradiation was 48 $\mu\text{Sv/hr}$, which corresponds to a dose of 27 μSv for a 2000 s measurement. This is lower than the kidney irradiation due to the fact that the liver is a large organ that shields the other radiosensitive organs, and also due to the fact that the radiation dose to the liver is

averaged over a larger volume than, for example, the stomach or kidneys. The effective radiation dose for a single 2000 s leg muscle irradiation was found to be extremely low at 0.6 μSv , and this was one of the motivating factors for the *in vivo* study performed in Chapter 6.

The potential dose-enhancement from the presence of Gd in tissue was considered in detail. There is no significant dose-enhancement for the $^{238}\text{Pu}/\text{Be}$ system because the thermal neutron fluence is not a significant contributor to dose. If a source with a lower average neutron energy and higher thermal neutron fluence was used then the potential dose per source neutron could be significantly enhanced due to the presence of Gd in tissue. This is because the main dose-enhancement from the presence of Gd occurs from thermal neutron capture of ^{157}Gd releasing internal conversion and Auger electrons and low energy X rays. The main contribution to dose from the $^{238}\text{Pu}/\text{Be}$ system, however, is dominated by high energy neutrons. Over the course of the dosimetry calculations there were some observed discrepancies in the nuclear data libraries and therefore it is advised that researchers evaluate carefully the nuclear data's suitability for their specific applications.

The first ever pilot *in vivo* study measuring Gd by PGNA was performed in Chapter 6. A total of 10 healthy participants were recruited in this study, and every participant had measureable Gd concentration above the detection limit at the 99% confidence level for the first post-contrast injection neutron leg muscle scan. The measured concentrations of Gd ranged from 2.0 to 17.3 ppm. Phantom and *in vivo* detection limits were both determined to be 0.58 ppm Gd. The pre and late post-contrast measurements demonstrated no initial Gd concentration and no significant retention in muscle, respectively. The results of this study verified that the measurement system was working as expected and promote its use in future studies of Gd retention.

The measurement system was extended to another high neutron absorbing element, samarium (Sm). Both experimental and Monte-Carlo work were performed. Interesting comparisons were discovered between Sm and Gd which are both non- $1/\nu$ neutron absorbers. A significant contribution, 13%, to neutron capture in ^{149}Sm is from

epithermal neutrons, and the remainder is from thermal neutrons, compared to ^{157}Gd in which 98% of captures are from thermal neutrons. The detection limit of Sm in the kidney has been determined for various participant body types, and is based on the 334 and 440 keV prompt gamma ray emissions from neutron capture on ^{149}Sm . The experimental detection limit in the kidney placed at 4 cm axial and lateral depths in the torso phantom was determined to be 5.5 ppm. To the best of this author's knowledge, this was the first study investigating the feasibility of measuring *in vivo* Sm in the kidney by this method.

8.2 Future work

8.2.1 Accelerator-based neutron source

A natural extension from the isotopic source-based system is an accelerator-based neutron source. In our laboratory, one available system is the production of neutrons via the $^7\text{Li}(p,n)$ reaction of protons from a 3.0 MeV Van de Graaf accelerator (the “KN”, model KN3000, HVEC, USA) on a metal lithium target. The accelerator-based system has advantages over the source-based system due to the lower average neutron energy (< 500 keV) from the Li target reaction for incident proton energies up to 2.5 MeV (Lee, Zhou 1999), and the neutron emission rate can be controlled by the proton current control of the accelerator. The range of current available is 40 nA to 35 μA , which for proton energies of 1.95, 2.1, and 2.3 MeV corresponds to neutron emission rate yield ranges of 4.5×10^5 - 3.9×10^8 , 5.6×10^6 - 4.9×10^9 , and 1.6×10^7 - 1.4×10^{10} n/s, respectively (experimental yields from (Matysiak, Prestwich & Byun 2011)). Therefore, this allows for control of neutron emission over many orders of magnitude; one highly flexible advantage over the fixed emission rate of the source-based system. This can also be a limitation because of detector neutron damage, therefore it is critical to have a reliable MCNP model to help develop a ‘neutron safe’ detector arrangement.

A Monte-Carlo neutron source card is available for the angular and spectral neutron output for incident proton energies from 1.95 to 2.3 MeV for the $^7\text{Li}(p,n)$ reaction. This source card is a well developed model based on excellent experimental and

theoretical work performed previously by researchers here at McMaster (Arnold et al. 2000, Matysiak, Prestwich & Byun 2008) and elsewhere (Lee, Zhou 1999). Since the neutron output from the accelerator-based source is significantly greater than for the source-based system it is important to understand the neutron field, especially in the germanium detector positions. Damage to germanium from neutrons has generally been attributed to fast neutrons above 0.7-1 MeV (Darken 1980). These fast neutrons generally lead to fast germanium nuclear recoils which in turn collide with many other germanium nuclei during their short path in the crystal producing damage clusters. The average neutron energy for the (p,n) reaction on lithium is dependent on the incident proton energy. For proton energies up to 2.5 MeV the maximum neutron energy is less than 0.8 MeV and the average is 0.33 MeV (Lee, Zhou 1999). For incident protons at 2.1 MeV the maximum neutron energy is 0.35 MeV, and the average energy is 0.108 MeV. Therefore neutrons are produced with energies below the commonly quoted threshold for damage. However, it is difficult to determine which, if any, neutron energies are “safe” for germanium detectors. Some 25 eV is required to dislocate a germanium atom (Kraner 1980). Elastic scattering interactions for neutrons with energies in the keV region are sufficient to dislocate a germanium atom from the crystal lattice. In addition, thermal neutrons can actually transmute some of the Ge to n-type ($^{76}\text{Ge} + n$ produces ^{77}Se ; $^{74}\text{Ge} + n$ produces ^{75}As) or p-type ($^{70}\text{Ge} + n$ produces ^{71}Ga) impurities. Therefore for PGNAA experiments involving HPGe detectors it would not be too conservative to assume that any neutron, of any energy, would have the potential to damage the detector.

Although, in principle, the lower average neutron energy is desirable in terms of dose per source neutron and higher neutron capture rates, it will also be very important to consider the potential dose-enhancement from the presence of Gd in tissues because there will be a larger contribution to the neutron fluence from thermal neutrons. A higher thermal neutron fluence would mean a higher number of neutron captures with Gd and therefore a proportionally larger amount of local energy deposition from the internal conversion and Auger electrons and low energy X rays from neutron capture of ^{157}Gd . This will provide a dose-enhancement. However, a significant portion of the dose is still

expected to be from neutron elastic scattering events on hydrogen, which are subsequently weighted by relatively large radiation weighting factors, and therefore dominate the equivalent dose contribution. In addition, due to the lower average energy, a greater proportion of the dose (as compared to the $^{238}\text{Pu}/\text{Be}$ system) will be from the $^{14}\text{N}(\text{n,p})^{14}\text{C}$ reaction which locally deposits a high energy proton and recoil ^{14}C nucleus with a reaction Q value greater than 0.6 MeV. The dose components will most significantly depend on the proportionate amount of nitrogen, hydrogen, and, potentially gadolinium, which will all compete for neutron interactions in tissues.

8.2.2 Indirect measurement of Gd

In Chapter 1 a significant reduction in the number of 2.223 MeV counts from neutron capture on ^1H was demonstrated with 151 ppm Gd in the 2 L leg phantom. This suggests that Gd could be measured indirectly through the reduction in the number hydrogen counts due to the preferential neutron absorption in Gd. Although this is not element specific, Gd has the largest thermal neutron capture cross section of all the elements, and therefore a measured reduction this significant in human tissues could be highly indicative for the potential presence of Gd. Through Monte-Carlo simulation, the ‘reduction ratio’ as a function of Gd concentration was calculated and is shown in Figure 8.1. This is the ratio of the capture rate in ^1H with no Gd present to the capture rate with Gd present in the 2 L phantoms. The reduction ratio measured by the relative 2.223 MeV peak areas for 151 ppm Gd present using the NaI detector was 1.3, and the reduction ratio measured using the GMX detector was 1.48. The GMX detector peak area ratio exactly matches the reduction ratio determined by MCNP for the relative number of neutron captures on ^1H . This may suggest that the GMX detector, due to its lower efficiency and smaller size than the NaI detector, may be more sensitive to changes in the hydrogen signal from the phantom, whereas the NaI detector may measure a significantly higher contribution from both the phantom and the shielding and collimating apparatus.

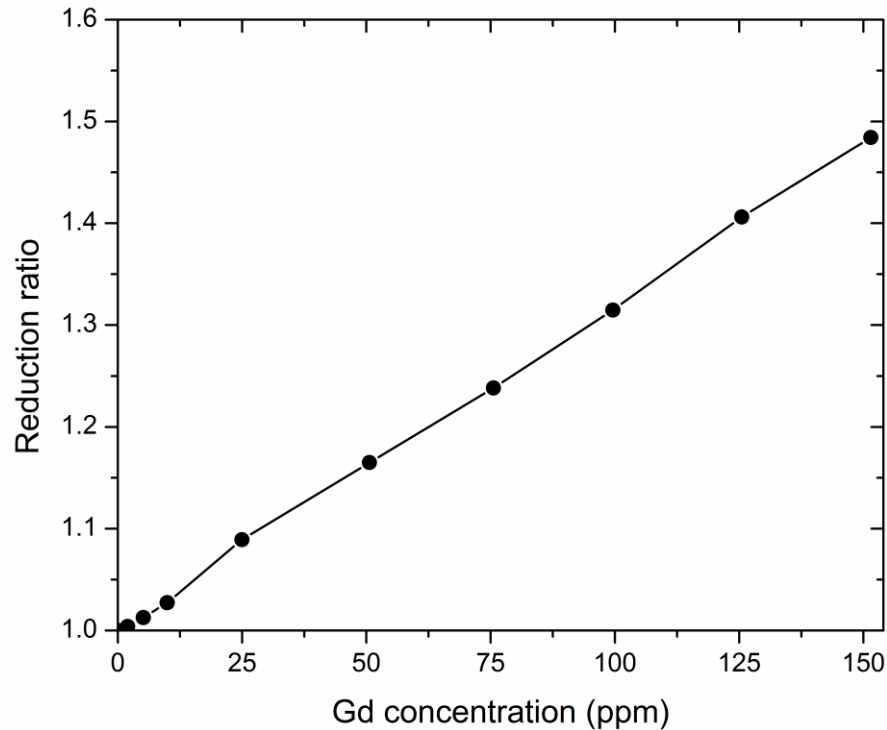


Figure 8.1. Simulated reduction in the number of 2.223 MeV hydrogen neutron captures as a function of Gd concentration in the 2 L phantoms.

This could be used as a relatively easy method if there was suspected exposure to Gd. Based on the reduction ratio of Figure 8.1 the detection limit would be less than 10 ppm for the 2 L phantoms. However, the effects for organs such as the kidney and liver will have to be investigated; the effect may not be as significant as seen in the homogenous 2 L phantoms. Also this may prove to be difficult when matching human with phantom results because the concentration is based on the difference in the hydrogen signal between Gd present and Gd absent. Measurements would have to be performed comparing the hydrogen signal in phantoms to humans to see if there is a good correlation. Otherwise, participant measurements would need to be performed before and after Gd exposure so that an accurate reduction ratio could be measured. However, despite the limitations, I suggest that this may be an interesting alternative indirect method to quantify Gd *in vivo*.

8.2.3 Kidney impaired population

Much of the toxicity of Gd-based contrast agents has been demonstrated in the kidney impaired population. The proposed method of toxicity in this group is due to the prolonged time the agents will be in body (because of reduced excretion capacity) and thus the greater chance for release of Gd from the chelate from *in vivo* transmetallation due to competition with other endogenous cations. These agents are now contraindicated for use in people with end stage renal disease. However, there are some cases where people with poor renal function are administered Gd-based contrast agents because the particular diagnosis is a benefit worth the risk of exposure. In addition, there is the potential for many people currently living with NSF who have mild or subclinical symptoms and are undiagnosed to be exposed (Marckmann 2011). This technique could therefore be used as a companion diagnostic tool for asymptomatic NSF cases potentially to investigate the retention of Gd and its role in disease development. The distribution in the kidney and liver could be determined, and results could be compared with skin biopsy measurements as well as bone measurements. Since the leg muscle measurement is a very low radiation exposure the muscle measurement could also be performed in combination with these organ and tissue measurements. Relationships could be determined with dose administered and the type or brand of Gd-based contrast agent administered.

8.2.4 Gadolinium in bone

The retention of Gd in bone in healthy individuals has been well demonstrated in biopsy measurements for patients receiving hip replacement surgery (White, Gibby & Tweedle 2006, Darrah et al. 2009). In the work of Darrah et al. (2009) the levels were as high as 39.5 nmol/g (~6 ppm) Gd in trabecular bone, with a mean of 16 nmol/g (~2.5 ppm). In cortical bone the mean was 9.36 nmol/g (~1.5 ppm) and the maximum was 31 nmol/g (~4.9 ppm). This promotes the need for the development of a measurement system for the residual *in vivo* content of Gd in bone. One method to measure the Gd content in bone

could be *in vivo* X ray Fluorescence (XRF). A suitable and convenient source could be a ^{241}Am source. This source emits a 59.5 keV gamma ray that is fortuitously just above the Gd K edge at 50.2 keV, and has a very long half-life of 433 years. A source-excited system using ^{241}Am has been under investigation to measure Gd in tumours for potential applications in determining tumour concentrations prior to Gd neutron capture therapy (Almalki et al. 2010). However, the detection limits were on the order of mg/g for this system with a 0.97 Ci source. A 1 mm thick CdTe detector with dimensions of $3 \times 3 \text{ mm}^2$ was used by these researchers (Amptek, Inc, USA). The intrinsic detection efficiency of the CdTe detector used was sufficient to detect the 40-50 keV Gd characteristic X rays, but the absolute detection efficiency was quite low. If a 50 mm diameter and 20 mm thick HPGe detector (standard small volume HPGe detector dimensions) was used the absolute detection efficiency would be 250 times higher than the CdTe detector at the Gd K_α X ray energy ($\sim 43 \text{ keV}$) for a point source 10 cm from the detector. I calculate that the detection limit would therefore be on the order of parts per million. The detection limit could be improved further by increasing the activity of the source, as suggested by Almalki *et al.* (2010). Based on the specific exposure rate constant for ^{241}Am the equivalent skin dose rate would be approximately 11 mSv/hr for a 1 Ci source at a 10 cm distance. This dose rate is comparable to other *in vivo* XRF measurements. The signal-to-noise ratio and dosimetry are obvious limiting factors that would need to be investigated further.

Another method to measure Gd in bone could be PGNA with either the $^{238}\text{Pu}/\text{Be}$ source-based system or an accelerator-based system. The detection limit in the hand-bones for the current $^{238}\text{Pu}/\text{Be}$ system is estimated by MCNP computation to be 2.2 ppm for bone with density of 1.4 g/cm^3 (for a 2000 s measurement). This was determined by substituting bone into the same 125 mL polyethylene bottles used for the kidney phantoms. Similar sized bone phantoms have been used by other researchers in our laboratory and have proved to be adequate representations of human hand-bones (Chamberlain et al. 2012a, Chamberlain et al. 2012b). The bone phantom was placed in 4 cm lateral and axial depths in the torso phantom as described in Chapter 4. This was done to improve the thermal neutron fluence in the phantom. In fact, the neutron capture rate is

almost 7 times higher than if the hand were placed in the same position in air; without any water moderation from the torso phantom. This positioning is feasible for *in vivo* measurement since the participant could place their hand at the same position within the water tank (torso phantom) quite easily and comfortably. This detection limit is comparable to the concentrations measured by Darrah et al. (2009) and White et al. (2006). However an improvement of a factor of 2 or more would be desirable. The neutron equivalent radiation dose rate to the hand bones and skin were computed by Monte-Carlo simulation to be 1.2 mSv/hr and 0.11 mSv/hr, respectively. Using a tissue fraction of 0.013 for both the bone and skin (Byun et al. 2007), and the radiation weighting factor of 0.01 for both bone and skin (ICRP 2007), the neutron effective dose rate for this measurement is estimated to be 0.17 μ Sv/hr (photons would contribute an additional 10%). This is a very low dose rate, and therefore suggests that future improvements in sensitivity by potentially moving the source closer to the collimator exit could be investigated. Also, investigations of different moderating materials and thicknesses could improve the detection limit. Of course the signal-to-noise ratio for these optimizations would need to be closely monitored. These are the first ever detection limit and dose rate estimates for the *in vivo* measurement of Gd in bone by PGNAA using the $^{238}\text{Pu}/\text{Be}$ source-based system.

The non-invasive bone retention measurement techniques described above could be cross-validated by ICP-MS with bones collected from hip or knee replacement surgeries.

In conclusion a new non-invasive Gd monitoring system has been developed utilizing both the prompt gamma ray and X ray transitions from Gd neutron capture. This was the first ever investigation measuring *in vivo* Gd by PGNAA. The measurement is low risk with effective radiation doses on the order of μ Sv. The system and technique have been verified in the first *in vivo* pilot study on 10 participants. The system also demonstrates that it may be able to measure the biological half-life of Gd-based chelates. The system can be applied in future studies in at risk populations exposed to Gd-based contrast agents. The well benchmarked model will be useful in future system

optimizations and measurements in other organs and tissues. The system and Monte-Carlo model can also be applied to other high neutron absorbers such as cadmium and samarium.

References

- Almalki, M., Majid, S., Butler, P. & Reinisch, L. 2010, "Gadolinium concentration analysis in brain phantom by X-ray fluorescence", *Australasian Physical & Engineering Science in Medicine*, vol. 33, no. 2, pp. 185-191.
- Arnold, M.L., McNeill, F.E., Prestwich, W.V. & Chettle, D.R. 2000, "System design for in vivo neutron activation analysis measurements of manganese in the human brain: based on Monte Carlo modeling", *Applied Radiation and Isotopes*, vol. 53, no. 4–5, pp. 651-656.
- Atanackovic, J., Grinyer, J., Chettle, D.R. & Byun, S.H. 2007, "The comparison of two MCNP models used for prompt gamma in vivo detection of cadmium and mercury", *Nuclear Instruments and Methods in Physics Research Section B*, vol. 263, no. 1, pp. 169-174.
- Bell, A.R., McRae, G., Wassenaar, R. & Wells, G. 2011, "Neutron activation for planar and SPECT imaging", *Biomedical Imaging: From Nano to Macro, 2011 IEEE International Symposium on*, 30 2011-april 2, pp. 1801.
- Block, S., Bryan, J., Prevo, C. & Montan, D. 1967, "Laboratory sources enhanced in 0.5 eV to 200 keV neutrons for instrument evaluation", *Health Physics*, vol. 13, no. 9, pp. 1025-1031.
- Browne, E. & Tuli, J.K. 2007, "Nuclear Data Sheets for A = 234", *Nuclear Data Sheets*, vol. 108, no. 3, pp. 681-772.
- Byun, S.H., Pejović-Milić, A., McMaster, S., Matysiak, W., Aslam, Liu, Z., Watters, L.M., Prestwich, W.V., McNeill, F.E. & Chettle, D.R. 2007, "Dosimetric characterization of the irradiation cavity for accelerator-based in vivo neutron activation analysis", *Physics in Medicine and Biology*, vol. 52, no. 6, pp. 1693-1703.
- Caswell, R.S., Coyne, J.J. & Randolph, M.L. 1980, "Kerma Factors for Neutron Energies below 30 MeV", *Radiation Research*, vol. 83, no. 2, pp. 217-254.
- Chadwick, M.B., Barschall, H.H., Caswell, R.S., DeLuca, P.M., Hale, G.M., Jones, D.T.L., MacFarlane, R.E., Meulders, J.P., Schuhmacher, H., Schrewe, U.J., Wambersie, A. & Young, P.G. 1999, "A consistent set of neutron kerma coefficients from thermal to 150 MeV for biologically important materials", *Medical Physics*, vol. 26, no. 6, pp. 974-991.

- Chadwick, M.B., Obložinský, P., Herman, M., Greene, N.M., McKnight, R.D., Smith, D.L., Young, P.G., MacFarlane, R.E., Hale, G.M., Frankle, S.C., Kahler, A.C., Kawano, T., Little, R.C., Madland, D.G., Moller, P., Mosteller, R.D., Page, P.R., Talou, P., Trellue, H., White, M.C., Wilson, W.B., Arcilla, R., Dunford, C.L., Mughabghab, S.F., Pritychenko, B., Rochman, D., Sonzogni, A.A., Lubitz, C.R., Trumbull, T.H., Weinman, J.P., Brown, D.A., Cullen, D.E., Heinrichs, D.P., McNabb, D.P., Derrien, H., Dunn, M.E., Larson, N.M., Leal, L.C., Carlson, A.D., Block, R.C., Briggs, J.B., Cheng, E.T., Huria, H.C., Zerkle, M.L., Kozier, K.S., Courcelle, A., Pronyaev, V. & van der Marck, S.C. 2006, "ENDF/B-VII.0: Next Generation Evaluated Nuclear Data Library for Nuclear Science and Technology", *Nuclear Data Sheets*, vol. 107, no. 12, pp. 2931-3060.
- Chamberlain, M., Gräfe, J.L., Aslam, Byun, S.H., Chettle, D.R., Egden, L.M., Orchard, G.M., Webber, C.E. & McNeill, F.E. 2012a, "The feasibility of *in vivo* quantification of bone-fluorine in humans by delayed neutron activation analysis: a pilot study", *Physiological Measurement*, vol. 33, pp. 243-257.
- Chamberlain, M., Gräfe, J.L., Aslam, Byun, S.H., Chettle, D.R., Egden, L.M., Webber, C.E. & McNeill, F.E. 2012b, "*In vivo* quantification of bone-fluorine by delayed neutron activation analysis: a pilot study of hand-bone-fluorine levels in a Canadian population", *Physiological Measurement*, vol. 33, no. 3, pp. 375-384.
- Chettle, D.R. 2006, "Occupational nuclear medicine: Trace element analysis of living human subjects", *Journal of Radioanalytical and Nuclear Chemistry*, vol. 268, no. 3, pp. 653-661.
- Chettle, D.R. & Fremlin, J.H. 1984, "Techniques of *in vivo* neutron activation analysis", *Physics in Medicine and Biology*, vol. 29, no. 9, pp. 1011-1043.
- Colletti, P.M. 2008, "Nephrogenic Systemic Fibrosis and Gadolinium: A Perfect Storm", *American Journal of Roentgenology*, vol. 191, no. 4, pp. 1150-1153.
- Cristy, M. 1981, "Active bone marrow distribution as a function of age in humans", *Physics in Medicine and Biology*, vol. 26, pp. 389-400.
- Culbertson, C.N. & Jevremovic, T. 2003, "Computational assessment of improved cell-kill by gadolinium-supplemented boron neutron capture therapy", *Physics in Medicine and Biology*, vol. 48, pp. 3943-3959.
- Darken, L. 1980, "Mechanism for fast neutron damage of Ge(HP) detectors", *Nuclear Instruments and Methods*, vol. 171, pp. 49-59.

- Darrah, T.H., Prutsman-Pfeiffer, J.J., Poreda, R.J., Ellen Campbell, M., Hauschka, P.V. & Hannigan, R.E. 2009, "Incorporation of excess gadolinium into human bone from medical contrast agents", *Metallomics*, vol. 1, no. 6, pp. 479-488.
- De Stasio, G., Casalbore, P., Pallini, R., Gilbert, B., Sanità, F., Ciotti, M.T., Rosi, G., Festinesi, A., Larocca, L.M., Rinelli, A., Perret, D., Mogk, D.W., Perfetti, P., Mehta, M.P. & Mercanti, D. 2001, "Gadolinium in Human Glioblastoma Cells for Gadolinium Neutron Capture Therapy", *Cancer Research*, vol. 61, no. 10, pp. 4272-4277.
- Debertin, K. & Helmer, R.G. 1988, *Gamma- and X-ray Spectrometry with Semiconductor Detectors*, North-Holland, Amsterdam.
- Eckerman, K.F., Cristy, M. & Ryman, J.C. 1996, *The ORNL mathematical phantom series*. Available: <http://mcnp-green.lanl.gov/resources.html> [2010, 01/01].
- Elam, W.T., Ravel, B.D. & Sieber, J.R. 2002, "A new atomic database for X-ray spectroscopic calculations", *Radiation Physics and Chemistry*, vol. 63, no. 2, pp. 121-128.
- Ellis, K.J. 1990, "The effective half-life of a broad beam $^{238}\text{Pu}/\text{Be}$ total body neutron irradiator", *Physics in Medicine and Biology*, vol. 35, pp. 1079-1087.
- FDA 2009, *Gadolinium-Based Contrast Agents for Magnetic Resonance Imaging*. Available: http://www.fda.gov/cder/drug/InfoSheets/HCP/gcca_200705.htm [2009, 3/17/2009].
- FDA 2006, *FDA Public Health Advisory: Gadolinium-containing Contrast Agents for Magnetic Resonance Imaging (MRI): Omniscan, OptiMARK, Magnevist, ProHance, and MultiHance*. Available: http://www.fda.gov/cder/drug/advisory/gadolinium_agents.htm [2009, 3/17/2009].
- Fedorowicz, R.P., Chettle, D.R., Kennett, T.J., Prestwich, W.V. & Webber, C.E. 1993, "A $^{238}\text{Pu}/\text{Be}$ facility for in vivo cadmium measurements", *Basic Life Sciences*, vol. 60, pp. 323-324.
- Franken, N.A.P., Bergs, J., Kok, T.T., Kuperus, R.R.N., Stecher-Rasmussen, F., Haveman, J., Bree, v.C. & Stalpers, L.J.A. 2006, "Gadolinium enhances the sensitivity of SW-1573 cells for thermal neutron irradiation", *Oncology Reports*, vol. 15, no. 3, pp. 715-715-720.
- Franklin, D.M., Armstrong, R., Chettle, D.R. & Scott, C. 1990, "An improved in vivo neutron activation system for measuring kidney cadmium", *Physics in Medicine and Biology*, vol. 35, no. 10, pp. 1397-1408.

- Gierga, D.P., Yanch, J.C. & Shefer, R.E. 2000, "An investigation of the feasibility of gadolinium for neutron capture synovectomy", *Medical Physics*, vol. 27, no. 7, pp. 1685-1692.
- Gilmore, G. 2008, *Practical Gamma-ray Spectroscopy*, 2nd edn, John Wiley & Sons Ltd., Chichester.
- Goorley, T. & Nikjoo, H. 2000, "Electron and photon spectra for three gadolinium-based cancer therapy approaches", *Radiation Research*, vol. 154, no. 5, pp. 556-563.
- Goorley, T., Zamenhof, R. & Nikjoo, H. 2004, "Calculated DNA Damage from Gadolinium Auger Electrons and Relation to Dose Distributions in a Head Phantom", *International Journal of Radiation Biology*, vol. 80, no. 11-12, pp. 933-940.
- Gräfe, J.L., McNeill, F.E., Chettle, D.R. & Byun, S.H. 2012, "Characteristic X ray emission in gadolinium following neutron capture as an improved method of *in vivo* measurement: a comparison between feasibility experiment and Monte Carlo simulation", *Nuclear Instruments and Methods in Physics Research B*, vol. 281, pp. 21-25.
- Gräfe, J.L., McNeill, F.E., Byun, S.H., Chettle, D.R. & Noseworthy, M.D. 2011, "The feasibility of *in vivo* detection of gadolinium by prompt gamma neutron activation analysis following gadolinium-based contrast-enhanced MRI", *Applied Radiation and Isotopes*, vol. 69, no. 1, pp. 105-111.
- Gräfe, J.L., McNeill, F.E., Byun, S.H., Chettle, D.R. & Noseworthy, M.D. 2010, "A benchmarked MCNP model of the *in vivo* detection of gadolinium by prompt gamma neutron activation analysis", *Nuclear Instruments and Methods in Physics Research Section B: Beam Interactions with Materials and Atoms*, vol. 268, no. 15, pp. 2451-2457.
- Grinyer, J., Byun, S.H. & Chettle, D.R. 2005, "In vivo prompt gamma neutron activation analysis of cadmium in the kidney and liver", *Applied Radiation and Isotopes*, vol. 63, no. 4, pp. 475-479.
- Grinyer, J. 2008, *Measurements of cadmium and mercury organ burdens using prompt gamma neutron activation analysis and X-ray fluorescence*, Ph.D. edn, McMaster University, Ottawa : Library and Archives Canada.
- Grobner, T. 2006, "Gadolinium-a specific trigger for the development of nephrogenic fibrosing dermopathy and nephrogenic systemic fibrosis?", *Nephrology Dialysis Transplantation*, , pp. 1108.

- Grobner, T. & Prischl, F.C. 2007, "Gadolinium and nephrogenic systemic fibrosis", *Kidney international*, vol. 72, no. 3, pp. 260-264.
- Groshev, L.V., Demidov, A.M., Ivanov, V.A., Lutsenko, V.N. & Pelekhov, V.I. 1963, "Levels of the nucleus Sm^{150} excited in the (n, γ) reaction", *Nuclear Physics*, vol. 43, no. 0, pp. 669-683.
- Haynes, W.M. 2012, *CRC Handbook of Chemistry and Physics*. 92nd Edition (Internet Version 2012) edn, CRC Press/Taylor and Francis, Boca Raton, FL.
- Helmer, R.G. 2004, "Nuclear Data Sheets for A=158", *Nuclear Data Sheets*, vol. 101, no. 3, pp. 325-519.
- Hirano, S. & Suzuki, K.T. 1996, "Exposure, metabolism, and toxicity of rare earths and related compounds", *Environmental Health Perspectives*, vol. 104 Suppl 1, pp. 85-95.
- IAEA 2007, *Database for PGNAA*. Available: <http://www-nds.iaea.org/pgaa/>.
- ICRP 2007, "P103: The 2007 Recommendations of the International Commission on Radiological Protection", *Annals of the ICRP*, vol. 37, no. 2-4, pp. 49-79.
- ICRP 2002, "Basic anatomical and physiological data for use in radiological protection: reference values. A report of age- and gender-related differences in the anatomical and physiological characteristics of reference individuals. ICRP Publication 89", *Annals of the ICRP*, vol. 32, no. 3-4, pp. 5-265.
- ICRP 1996, "Conversion Coefficients for use in Radiological Protection against External Radiation. ICRP Publication 74.", *Annals of the ICRP*, vol. 26, no. (3-4).
- ICRP 1991, "1990 Recommendations of the International Commission on Radiological Protection. ICRP Publication 60", *Annals of the ICRP*, vol. 21, no. (1-3).
- Kraner, H.W. 1980, "Fast Neutron Damage in Germanium Detectors", *Nuclear Science, IEEE Transactions on*, vol. 27, no. 1, pp. 217-234.
- Kraner, H.W., Pehl, R.H. & Haller, E.E. 1975, "Fast Neutron Radiation Damage of High-Purity Germanium Detectors", *Nuclear Science, IEEE Transactions on*, vol. 22, no. 1, pp. 149-159.
- Krstić, D. & Nikezić, D. 2007, "Input files with ORNL—mathematical phantoms of the human body for MCNP-4B", *Computer Physics Communications*, vol. 176, no. 1, pp. 33-37.

- Kurczynski, P., Pehl, R.H., Hull, E.L., Palmer, D., Harris, M.J., Seifert, H., Teegarden, B.J., Gehrels, N., Cline, T.L., Ramaty, R., Sheppard, D., Madden, N.W., Luke, P.N., Cork, C.P., Landis, D.A., Malone, D.F. & Hurley, K. 1999, "Long-term radiation damage to a spaceborne germanium spectrometer", *Nuclear Instruments and Methods in Physics Research Section A*, vol. 431, no. 1–2, pp. 141-147.
- Lameire, N., Floege, J. & Wheeler, D.C. 2010, "The five most cited NDT papers from 2005 to 2009", *Nephrology Dialysis Transplantation*, vol. 25, no. 9, pp. 2825-2831.
- LANL 2006, *Information on MISC5XS*, Los Alamos National Laboratory. Available: <http://www-xdiv.lanl.gov/projects/data/nuclear/mcnpdata/misc5xs.html> [2012, 02/12].
- Lee, C.L. & Zhou, X.-. 1999, "Thick target neutron yields for the ${}^7\text{Li}(p,n){}^7\text{Be}$ reaction near threshold", *Nuclear Instruments and Methods in Physics Research Section B*, vol. 152, no. 1, pp. 1-11.
- Lone, M.A., Leavitt, R.A. & Harrison, D.A. 1981, "Prompt gamma rays from thermal-neutron capture", *Atomic Data and Nuclear Data Tables*, vol. 26, no. 6, pp. 511-559.
- MacFarlane, R.E. 2007, *Energy-Balance Tests for ENDF/B-VII*. Los Alamos National Laboratory. Available: <http://t2.lanl.gov/data/ebalVII/summary.html> [2012, 01/15].
- Marckmann, P. 2011, "Gadolinium-based Magnetic Resonance Contrast Agents and Nephrogenic Systemic Fibrosis", *US Nephrology*, vol. 6, no. 1, pp. 40-44.
- Matsumoto, T. 1992, "Transport calculations of depth-dose distributions for gadolinium neutron capture therapy", *Physics in Medicine and Biology*, vol. 37, pp. 155-162.
- Matysiak, W., Prestwich, W.V. & Byun, S.H. 2011, "Precise measurements of the thick target neutron yields of the ${}^7\text{Li}(p,n)$ reaction", *Nuclear Instruments and Methods in Physics Research Section A*, vol. 643, no. 1, pp. 47-52.
- Matysiak, W., Prestwich, W.V. & Byun, S.H. 2008, "Measurement of the thick target ${}^7\text{Li}(p,n)$ neutron source spectrum using a ${}^3\text{He}$ ionization chamber", *Nuclear Instruments and Methods in Physics Research Section A*, vol. 592, no. 3, pp. 316-324.
- McEwan, A.J.B. 2000, "Use of radionuclides for the palliation of bone metastases", *Seminars in radiation oncology*, vol. 10, no. 2, pp. 103-114.
- McNeill, F.E. & Chettle, D.R. 1998, "Improvements to the in vivo measurement of cadmium in the kidney by neutron activation analysis", *Applied Radiation and Isotopes*, vol. 49, no. 5–6, pp. 699-700.

- Miller, G.A., Hertel, N.E., Wehring, B.W. & Horton, J.L. 1993, "Gadolinium neutron capture therapy", *Nuclear Technology*, vol. 103, no. 3, pp. 320-331.
- Owens, A., Brandenburg, S., Buis, E.-., Kozorezov, A.G., Kraft, S., Ostendorf, R.W. & Quarati, F. 2007, "Effect of prolonged annealing on the performance of coaxial Ge gamma-ray detectors", *Journal of Instrumentation*, vol. 2, pp. 1001.
- Pirard, B., Cabrera, J., d'Uston, C., Thocaven, J.J., Gasnault, O., Leleux, P. & Brückner, J. 2007, "Solar proton damage in high-purity germanium detectors", *Nuclear Instruments and Methods in Physics Research Section A*, vol. 572, no. 2, pp. 698-707.
- Popovic, M., McNeill, F.E., Chettle, D.R., Webber, C.E., Lee, C.V. & Kaye, W.E. 2005, "Impact of Occupational Exposure on Lead Levels in Women", *Environmental Health Perspectives*, vol. 113, no. 4, pp. 484.
- Quarati, F., Brandenburg, S., Buis, E.-., Dressler, P., Kraft, S., Lampert, M.-., Ostendorf, R.W., Owens, A., Peacock, A., Quirin, P. & Quirion, D. 2009, "Solar proton event damage in space-borne Ge detectors", *Nuclear Instruments and Methods in Physics Research Section A*, vol. 610, no. 1, pp. 354-357.
- Raudorf, T.W., Trammell, R.C., Wagner, S. & Pehl, R.H. 1984, "Performance of Reverse Electrode HPGE Coaxial Detectors after Light Damage by Fast Neutrons", *Nuclear Science, IEEE Transactions on*, vol. 31, no. 1, pp. 253-257.
- Reedy, R.C. & Frankle, S.C. 2002, "Prompt gamma rays from radiative capture of thermal neutrons by elements from hydrogen through zinc", *Atomic Data and Nuclear Data Tables*, vol. 80, no. 1, pp. 1-34.
- S.F Mughabghab, M. Divadeenam and N.E. Holden 1981, "Neutron Cross Sections from Neutron Resonance Parameters and Thermal Cross Sections" in New York.
- Sakurai, Y. & Kobayashi, T. 2002, "Experimental verification of the nuclear data of gadolinium for neutron capture therapy", *Journal of Nuclear Science and Technology*, vol. Supplement 2, pp. 1294-1297.
- Salt, C., Lennox, A.J., Takagaki, M., Maguire, J.A. & Hosmane, N.S. 2004, "Boron and gadolinium neutron capture therapy", *Russian Chemical Bulletin*, vol. 53, no. 9, pp. 1871-1888.
- Slatkin, D.N. 1991, "A History of Boron Neutron Capture Therapy of Brain Tumours", *Brain*, vol. 114, no. 4, pp. 1609-1629.

- Smither, R.K. 1966, "Gamma-Ray Spectrum from Thermal-Neutron Capture in Sm^{149} , and Associated Energy Levels in Sm^{150} ", *Physical Review*, vol. 150, no. 3, pp. 964-984.
- Spowart, A.R. 1972, "Neutron radiography", *Journal of Physics E: Scientific Instruments*, vol. 5, no. 8, pp. 756-756.
- Stamatelatos, I.E.M., Chettle, D.R., Green, S. & Scott, M.C. 1992, "Design studies related to an in vivo neutron activation analysis facility for measuring total body nitrogen", *Physics in Medicine and Biology*, vol. 37, pp. 1657-1674.
- Stepanek, J. 2003, "Emission spectra of Gadolinium-158", *Medical Physics*, vol. 30, no. 1, pp. 41-43.
- Sun, G., Byun, S. & Choi, H. 2003, "Prompt k_0 -factors and relative gamma-emission intensities for the strong non- $1/\nu$ absorbers ^{113}Cd , ^{149}Sm , ^{151}Eu and $^{155,157}\text{Gd}$ ", *Journal of Radioanalytical and Nuclear Chemistry*, vol. 256, no. 3, pp. 541-552.
- Swaminathan, S., High, W.A., Ranville, J., Horn, T.D., Hiatt, K., Thomas, M., Brown, H.H. & Shah, S.V. 2008, "Cardiac and vascular metal deposition with high mortality in nephrogenic systemic fibrosis", *Kidney International*, vol. 73, no. 12, pp. 1413-1418.
- Thakral, C., Alhariri, J. & Abraham, J.L. 2007, "Long-term retention of gadolinium in tissues from nephrogenic systemic fibrosis patient after multiple gadolinium-enhanced MRI scans: case report and implications", *Contrast Media & Molecular Imaging*, vol. 2, no. 4, pp. 199-205.
- Voth, M., Rosenberg, M. & Breuer, J. 2011, "Safety of Gadobutrol, a New Generation of Contrast Agents: Experience From Clinical Trials and Postmarketing Surveillance", *Investigative Radiology*, vol. 46, no. 11, pp. 663-671.
- Wangerin, N., Culbertson, C.N. & Jevremovic, T. 2005, "A comparison of the COG and MCNP codes in computational neutron capture therapy modeling. Part II Gadolinium neutron capture therapy models and therapeutic effects", *Health Physics*, vol. 89, no. 2, pp. 135-144.
- Wastie, M.L. & Latief, K.H. 2004, "Gadolinium: named after Finland's most famous chemist", *British Journal of Radiology*, vol. 77, no. 914, pp. 146-147.
- White, G.W., Gibby, W.A. & Tweedle, M.F. 2006, "Comparison of Gd(DTPA-BMA) (Omniscan) Versus Gd(HP-DO3A) (ProHance) Relative to Gadolinium Retention in Human Bone Tissue by Inductively Coupled Plasma Mass Spectroscopy", *Investigative Radiology*, vol. 41, no. 3, pp. 272-278.

Yasui, L.S., Andorf, C., Schneider, L., Kroc, T., Lennox, A. & Saroja, K.R. 2008,
"Gadolinium neutron capture in glioblastoma multiforme cells", *International Journal
of Radiation Biology*, vol. 84, no. 12, pp. 1130-1139.